

A Dissertation

entitled

*NUMERICAL SIMULATION OF HEAT CONDUCTION WITH
MELTING AND/OR FREEZING BY SPACE-TIME CONSERVATION
ELEMENT AND SOLUTION ELEMENT METHOD*

by

Anahita Ayasoufi

Submitted as partial fulfillment of the requirements for
the Doctor of Philosophy in Engineering



Adviser: *Professor Theo G. Keith*



Graduate School

The University of Toledo

December 2004

An Abstract of

NUMERICAL SIMULATION OF HEAT CONDUCTION WITH
MELTING AND/OR FREEZING BY SPACE-TIME CONSERVATION
ELEMENT AND SOLUTION ELEMENT METHOD

by

Anahita Ayasoufi

Submitted as partial fulfillment of the requirements for
the Doctor of Philosophy in Engineering Science

The University of Toledo

December 2004

Numerical simulation of the Enthalpy formulation, for the Stefan problems, is known to be limited by two difficulties: 1) non-physical waviness in the temperature distribution, as well as unwanted oscillations close to the phase interface, for isothermal phase change, and 2) convergence and stability problems, as well as inaccuracies due to overwhelming dissipation of the numerical schemes, at the limit of small Stefan numbers.

The method of space-time conservation element and solution element is known for its low dissipation and dispersion errors, as well as its distinguishingly high capability of capturing discontinuities accurately. Therefore, this numerical method, mainly applied to the fluid flow problems, represents an alternative for numerical modeling of moving boundary (Stefan) problems such as solid/liquid phase change.

In this dissertation, space-time CE/SE schemes are developed, for the solid/liquid phase change problems, in one-, two-, and three- spatial dimensions. A separate formulation is also presented and programmed for the axisymmetric problems. The von Neumann stability analysis is applied to the one-dimensional scheme. The results of this analysis lead to a necessary stability condition.

Each scheme is then validated, numerically, using benchmark problems without and with phase change. Both analytical and experimental results are used in the validation process. The results reveal that using the space-time CE/SE method, the first problem associated with the numerical modeling of the enthalpy method is eliminated. No non-physical waviness or unwanted oscillation is detected in the results. The second problem, however, still existed. Although accurate results can be obtained for small Stefan numbers using the CE/SE method, a case-dependent adjustment in dissipation was needed. This presents the potential for a modification in the original schemes.

Numerical experiments are then conducted, in order to reveal the dissipative / dispersive behavior of the numerical scheme and its variation with the Stefan number. The results of this analysis lead to the development of a CE/SE scheme that is, to a considerable degree, insensitive to the value of the Stefan number.

Finally, space-time CE/SE method is established as an alternative for the numerical simulation of the enthalpy method for the Stefan problems.

DEDICATIONS

I dedicate this work

To my father, Dr. Kazem Ayasoufi, who recognized and encouraged my enthusiasm towards science,

To my mother, Farideh Shahla, who supported and accompanied me in every step of my education,

To my husband, Ramin Khosravi Rahmani, who enlightens my thoughts through long hours of scientific discussions; who supports me in every conceivable aspect, and without whose knowledge, support and love, this work would not be possible, and,

To my adviser, Professor Theo G. Keith, whose vast knowledge, extraordinary personality, and unique management, not only made this work possible, but also profoundly changed my life in the most positive imaginable way.

Anahita Ayasoufi



From left to right:

Professor Theo G. Keith, Anahita Ayasoufi, Doctor Sin-Chung Chang

TABLE OF CONTENTS

CHAPTER 1	1
INTRODUCTION.....	1
1.1 REALM OF SOLID-LIQUID PHASE CHANGE PROCESSES.....	1
1.1.1 APPLICATION OF PHASE CHANGE PROCESS MODELING IN ASTROPHYSICS.....	1
1.1.2 <i>Application of Phase Change Process Modeling in Magma Migration and Solidification.....</i>	<i>2</i>
1.1.3 <i>Application of Phase Change Process Modeling in the Study of Undercooled Melts.....</i>	<i>3</i>
1.1.4 <i>Application of Phase Change Process Modeling in Studying Ablation of Entry Objects.....</i>	<i>4</i>
1.1.5 <i>Application of Phase Change Process Modeling in Aircraft Icing.....</i>	<i>4</i>
1.1.6 <i>Application of Phase Change Process Modeling in Casting of Metals.....</i>	<i>6</i>
1.1.7 <i>Application of Phase Change Process Modeling in Cryosurgery.....</i>	<i>7</i>
1.1.8 <i>Application of Phase Change Process Modeling in Cryopreservation of Cells and Organs for Transplantation.....</i>	<i>8</i>
1.2 MOVING (FREE) BOUNDARY PROBLEMS	10
1.2.1 <i>Historical Background of Moving Boundary Problems.....</i>	<i>10</i>
1.3 THE SPACE-TIME CONSERVATION ELEMENT AND SOLUTION ELEMENT METHOD - AN INNOVATIVE NUMERICAL SCHEME FOR FLUID MECHANICS PROBLEMS	22
1.3.1 <i>The CE/SE Method's History.....</i>	<i>23</i>
1.3.2 <i>The CE/SE Method's Features.....</i>	<i>24</i>
1.4 OUTLINE OF DISSERTATION	26
CHAPTER 2	1
PROBLEM STATEMENT AND FORMULATION	29
2.1 PHYSICAL PHENOMENA INVOLVED IN SOLID-LIQUID PHASE CHANGE PROCESSES	29
2.1.1 <i>Heat and Mass Transfer.....</i>	<i>31</i>
2.1.2 <i>Variation of Phase Change Temperature.....</i>	<i>31</i>
2.1.3 <i>Supercooling.....</i>	<i>32</i>
2.1.4 <i>Variation of Thermophysical Properties.....</i>	<i>33</i>
2.1.5 <i>Density Changes.....</i>	<i>33</i>
2.2 UNDERLYING ASSUMPTIONS.....	34
2.3 ENTHALPY METHOD.....	35
2.4 ISOTHERMAL PHASE CHANGE	37
2.5 PHASE CHANGE OVER A TEMPERATURE RANGE.....	38
CHAPTER 3	29
ONE-DIMENSIONAL CE/SE PHASE-CHANGE SCHEME.....	41
3.1 DEVELOPMENT OF A ONE-DIMENSIONAL CE/SE SCHEME FOR HEAT CONDUCTION WITH MELTING/FREEZING	42
3.1.1 <i>First-Order Derivatives.....</i>	<i>46</i>
3.1.2 <i>Second-Order Derivatives.....</i>	<i>47</i>
3.2 ON THE EQUIVALENCE OF THE CESE FORMULATION OF THE ENTHALPY METHOD WITH THE CONVENTIONAL FORMULATION.....	48
3.3 VON NEUMANN STABILITY ANALYSIS.....	55
3.2.1 <i>Linear Scheme without Second-Order Derivatives.....</i>	<i>57</i>
3.2.2 <i>Linear Scheme with Second-Order Derivatives.....</i>	<i>65</i>
3.2.3 <i>Non-Linear Scheme without Second-Order Derivatives.....</i>	<i>68</i>

3.2.4	<i>Non-Linear Scheme with Second-Order Derivatives.....</i>	<i>69</i>
3.4	VALIDATION TESTS.....	70
3.4.1	<i>Steady Linear Case.....</i>	<i>70</i>
3.4.2	<i>Single-Phase Stefan Problem.....</i>	<i>73</i>
3.4.3	<i>One-Dimensional Solidification of the Binary Al-4.5% Cu Alloy.....</i>	<i>74</i>
CHAPTER 4	41
TWO-DIMENSIONAL CE/SE PHASE-CHANGE SCHEME	83
4.1	DEVELOPMENT OF A TWO-DIMENSIONAL SPACE-TIME CE/SE SCHEME FOR HEAT CONDUCTION WITH MELTING/ FREEZING.....	84
4.1.1.	<i>First-Order Derivatives.....</i>	<i>91</i>
4.1.2.	<i>Second-Order Derivatives.....</i>	<i>92</i>
4.1.3.	<i>Boundary Conditions.....</i>	<i>93</i>
4.2	NUMERICAL RESULTS AND DISCUSSION.....	94
4.2.1	<i>The Steady Linear Case.....</i>	<i>95</i>
4.2.2	<i>A Problem with Time-Dependent Boundary Conditions.....</i>	<i>96</i>
4.2.3	<i>Freezing of a Finite Slab (a One-Phase Stefan Problem).....</i>	<i>97</i>
4.2.4	<i>Heat Conduction with Freezing in a Corner.....</i>	<i>99</i>
4.2.5	<i>Inward Freezing in a Circular Pipe.....</i>	<i>101</i>
CHAPTER 5	83
AXISYMMETRIC CE/SE PHASE-CHANGE SCHEME.....		111
5.1	DEVELOPMENT OF AN AXISYMMETRIC CE/SE SCHEME FOR HEAT CONDUCTION WITH MELTING/FREEZING	111
5.1.1.	<i>Convective Boundary Conditions.....</i>	<i>118</i>
5.2	NUMERICAL RESULTS AND DISCUSSION.....	118
5.2.1.	<i>Case 1: Time-Step Effects.....</i>	<i>119</i>
5.2.2.	<i>Case 2: Spatial Grid Size Effects.....</i>	<i>120</i>
5.2.3.	<i>Cases of the Thawing Cone</i>	<i>120</i>
CHAPTER 6	111
THREE-DIMENSIONAL CE/SE PHASE-CHANGE SCHEME		127
6.1	DEVELOPMENT OF A THREE-DIMENSIONAL CE/SE SCHEME FOR HEAT CONDUCTION WITH MELTING/FREEZING.....	127
6.1.1.	<i>Top/Bottom Faces.....</i>	<i>128</i>
6.1.2.	<i>Lateral Faces.....</i>	<i>130</i>
6.1.3.	<i>First-Order Derivatives.....</i>	<i>131</i>
6.1.4.	<i>Second-Order Derivatives.....</i>	<i>133</i>
6.1.5.	<i>Boundary Conditions.....</i>	<i>133</i>
6.2	NUMERICAL RESULTS AND DISCUSSION.....	134
6.2.1.	<i>Case 1: A Steady Linear Problem.....</i>	<i>135</i>
6.2.2.	<i>Case 2: A Problem with Time-Dependent Boundary Conditions.....</i>	<i>136</i>
6.2.3.	<i>Case 3: Freezing of a Finite Slab</i>	<i>136</i>
6.2.4.	<i>Case 4: Thawing of a Cube</i>	<i>139</i>
6.2.5.	<i>Case 5: Thawing of an ellipsoid.....</i>	<i>139</i>
6.2.6.	<i>Case 6: Thawing of a sphere.....</i>	<i>140</i>
CHAPTER 7	127
THE STEFAN-NUMBER INSENSITIVE CE/SE PHASE-CHANGE SCHEME.....		149
7.1	THE ORIGINAL ONE-DIMENSIONAL SCHEME	150
7.2	THE DISSIPATIVE / DISPERSIVE BEHAVIOR OF THE NUMERICAL SCHEME.....	152

7.3	A NEW CE/SE PHASE CHANGE SCHEME.....	154
7.4	NUMERICAL RESULTS AND DISCUSSION.....	158
CHAPTER 8		167
A SPACE-TIME CE/SE NAVIER-STOKES SOLVER		167
8.1	GOVERNING EQUATIONS.....	171
8.2	A SPACE -TIME CE/SE NAVIER-STOKES SCHEME.....	173
8.3	A NOTE ON THE BOUNDARY CONDITIONS.....	176
8.4	VALIDATION TESTS.....	178
8.4.1.	<i>The Uniform Flow Cases.....</i>	<i>178</i>
8.4.2.	<i>The Driven Cavity Problem.....</i>	<i>179</i>
CONCLUSIONS		190
FUTURE WORK.....		192
REFERENCES		194
APPENDIX A.....		212
APPENDIX B: AN UNSTRUCTURED THREE DIMENSIONAL REGULAR GRID GENERATOR		224
APPENDIX C.....		229

LIST OF TABLES

<i>Number</i>	<i>Page</i>
Table 3.1: Numerical experiments of stability: effect of the Stefan number	63
Table 3.2: Numerical experiments of stability: effect of the spatial increment	64
Table 3.3: Properties of a binary Al-4.5% Cu alloy from [86]	75
Table 6.1: Statistical parameters associated with Fig. 6.8	138
Table 8.1: Location of the core of the vortices, resulting from usage of different grid spacing.....	182

LIST OF FIGURES

<i>Number</i>	<i>Page</i>
Figure 2.1: Different microstructures of the solid-liquid phase interface	32
Figure 3.1: Computational molecule of the CE/SE method, (a) CE (j, n) and (b) SE (j, n)	76
Figure 3.2: Space-time conservation element containing the phase interface	76
Figure 3.3: The amplification factor for time step equal to 1.E-3, for the linear scheme without the second-order derivatives	77
Figure 3.4: The amplification factor for time step equal to 1.E-4, for the linear scheme without the second-order derivatives	77
Figure 3.5: The amplification factor for time step equal to 1.E-6, for the linear scheme without the second-order derivatives	78
Figure 3.6: The amplification factor for time step equal to 1.E-3, for the linear scheme with the second-order derivatives	78
Figure 3.7: The amplification factor for time step equal to 5.E-4, for the linear scheme with the second-order derivatives	79
Figure 3.8: The amplification factor for time step equal to 1.1E-5, for the linear scheme with the second-order derivatives	79
Figure 3.9: Time step zone 3 for one-dimensional code; vanishing errors for different time- steps	80
Figure 3.10: Optimum time-step	80
Figure 3.11: Temperature profile at $t = 0.14$ s	81
Figure 3.12: Enthalpy distribution at $t = 0.14$ s	81
Figure 3.13: Solidification of the binary Al-4.5% Cu alloy from [86]	82
Figure 3.14: The liquid fraction function	82
Figure 4.1: Computational molecule of CE/SE method, (a) CEs and (b) SEs	102
Figure 4.2: Boundary and ghost cells	103
Figure 4.3: Bounded growth of errors (Zone 2)	103
Figure 4.4: Vanishing errors (zone 3)	104
Figure 4.5: The grid-dependent truncation error	104
Figure 4.6: Demonstration of two-dimensional CE/SE scheme's second-order accuracy	105
Figure 4.7: Geometry of the freezing slab case	105
Figure 4.8: Location of the interface for the freezing slab case	106
Figure 4.9: Temperature distribution at $t = 0.14$ for the freezing slab case	106
Figure 4.10: Geometry for the freezing corner case	107
Figure 4.11: Temperature isotherms at $t = 0.02$ s, for the freezing corner case	107
Figure 4.12: Non-dimensional interface for the freezing corner case	108
Figure 4.13: An example of the grid within a square	108
Figure 4.14: Geometry of the inward freezing pipe case	109
Figure 4.15: An example mesh for the inward freezing pipe case	109
Figure 4.16: The interface position for the inward freezing pipe case	110
Figure 4.17: Enthalpy contours at $t = 0.11$ s for the inward freezing pipe case	110

Figure 5.1: Vanishing errors for case 1	123
Figure 5.2: Grid size effects for case 2	123
Figure 5.3: Demonstration of the axisymmetric CE/SE scheme's second-order accuracy	124
Figure 5.4: An example of the grid for conical cases	124
Figure 5.5: Position of the interface at different times, using enthalpy contours.	125
Figure 5.6: Position of the phase change interface on the axis of symmetry for the thawing cone case 2.....	125
Figure 5.7: Interface position for the thawing cone case 3	126
Figure 6.1: Geometry for 3D formulation.....	142
Figure 6.2: Vanishing errors for case 1	142
Figure 6.3: Grid size effects for case 2.....	143
Figure 6.4: Demonstration of the CE/SE scheme's second-order accuracy	143
Figure 6.5: Spatial grid for the unit cube.....	144
Figure 6.6: Location of the phase change interface for case 3.....	144
Figure 6.7: Temperature distribution at $t = 0.14$ s for case 3.....	145
Figure 6.8: Comparison of the errors at $t = 0.14$ s for case 3.....	145
Figure 6.9: The thawing cube, (case 4), at $t = 0.005, 0.02$, and 0.05 s.....	146
Figure 6.10: (a) Thawing ellipsoid, (case 5), at $t = 0, 0.0035$, and 0.0085 s; (b) Thawing sphere, (case 6), at $t = 0, 0.0025$, and 0.0065 s.....	147
Figure 6.11: Total melting time for the thawing sphere of case 6	148
Figure 7.1: Effect of the Stefan number on the dissipation of the original phase change scheme	161
Figure 7.2: Geometry for the modified scheme	161
Figure 7.3: Temperature and enthalpy distributions at $t = 0.14$ s, for $St = 0.01$	162
Figure 7.4: Temperature and enthalpy distributions at $t = 0.14$ s, for $St = 0.05$	163
Figure 7.5: Temperature and enthalpy distributions at $t = 0.14$ s, for $St = 0.1$	164
Figure 7.6: Temperature and enthalpy distributions at $t = 0.14$ s, for $St = 0.5$	165
Figure 7.7: Location of the phase interface at different times	166
Figure 8.1: Geometry of the driven cavity	184
Figure 8.2: Streamlines for the 200×200 grid.....	184
Figure 8.3: Comparison of the horizontal component of the velocity, on the vertical centerline, for different grids, with results from [46]	185
Figure 8.4: Comparison of the vertical component of the velocity, on the horizontal centerline, for different grids, with results from [46]	186
Figure 8.5: Convergence history for the 150×150 grid.....	187
Figure 8.6: Demonstration of the two-dimensional CE/SE Navier-Stokes scheme's second- order accuracy, based on velocity of the center of the cavity.....	188
Figure 8.7: Demonstration of the two-dimensional CE/SE Navier-Stokes scheme's second- order accuracy, based on x coordinate of the core of the bottom right vortex	189
Figure A.1: Geometric parameters involved in the transformation of the coordinates	212
Figure A.2: Transformation of the coordinate system.....	214

The University of Toledo

College of Engineering

I HEREBY RECOMMEND THAT THE DISSERTATION PREPARED UNDER MY
SUPERVISION BY *Anahita Ayasoufi*

ENTITLED *Numerical Simulation of Heat Conduction with Melting
and/or Freezing by Space-Time Conservation Element
and Solution Element Method*

BE ACCEPTED IN PARTIAL FULFILLMENT OF THE REQUIREMENTS FOR
THE DEGREE OF DOCTOR OF PHILOSOPHY IN ENGINEERING

Theo G. Keith

Dissertation Advisor: *Professor Theo G. Keith*

Recommendation concurred by .

Abdellah Afje

Committee member 2: *Professor A. Afje*

S. C. Chang

Committee member 3: *Dr. S. C. Chang*

K. C. Masiulaniec

Committee member 4: *Professor K. C. Masiulaniec*

N. Mostaghel

Committee member 5: *Professor N. Mostaghel*

T. Ng

Committee member 6: *Professor T. Ng*

Committee

On

Final Examination

Mohamed S. S. S.

Dean, College of Engineering

Chapter 1

INTRODUCTION

1.1 Realm of Solid-Liquid Phase Change Processes

The range of scientific and industrial applications of heat flow with solid-liquid phase change is so broad that, in many fields, one has little difficulty finding a phase change process involved. The vastness of this realm can be explored through a brief discussion of the recent and ongoing phase change related research, ranging from astrophysics to micro-cryopreservation of live cells for transplants.

1.1.1 Application of Phase Change Process Modeling in Astrophysics

Magma exists at high temperature and resides in a fluid-like state inside the Earth while its cooling process is still taking place. Modeling this cooling process has led to an estimation of the age of the planet to be not more than 1700 million years.

The cooling process results in the shrinkage of the already solidified crust, generating compressive stresses that cause failure and lead to formation of mountains, volcanic activities and seismic events, [1].

A more comprehensive model could be used to achieve a more accurate estimate of our planet's age. Moreover, it could predict relative movement of rocks, and could have the potential of predicting seismic events.

1.1.2 Application of Phase Change Process Modeling in Magma

Migration and Solidification

Consideration of the motion of magma and its solidification is important to the understanding of ore body formation and mineralization in the crust of the earth. Owing to the complex nature of the geological problem, numerical methods have been widely adopted to find approximate solutions to many geological and mineralization problems. Nevertheless, numerical algorithm development for simulating magma migration and solidification is still at an elementary stage. The problem associated with the numerical modeling is that, in this area, the characteristic dimension of the whole geological system under consideration has a length scale of tens and sometimes hundreds of kilometers, while that of the intruded magma, such as sills and dikes has a length scale of meters and tens of meters. Therefore, new methodologies could be useful to either solve the problems that were previously unsolvable using conventional finite element methods, or solve the previously solvable problems more efficiently, [2].

1.1.3 Application of Phase Change Process Modeling in the Study of Undercooled Melts

A melt can be cooled significantly below its equilibrium melting point if the energy barrier for nucleation of the solid phase is high. However, solid impurities, convective flows, and the local energy fluctuations in the melt can lower this energy barrier. The highest achievable energy barrier for nucleation, which corresponds to homogeneous nucleation, can be achieved only in a containerless, quiescent, pure melt.

Upon cooling, under such conditions, the melt can either solidify extremely rapidly from a very limited number of nucleation points giving rise to unique metastable microstructures, or the melt can pass through a glass transition and an amorphous solid phase is obtained. Knowledge of such processes enables one to predict the formation of specific phases or glasses with very unique properties.

Recent experience has demonstrated that with containerless processing in the space environment (i.e., using electromagnetic levitation), these conditions can be achieved and unique results can be obtained. However, attaining the proper experimental conditions required for such investigations is not possible on the ground for a wide range of materials, [3]. Therefore, a reliable numerical model could be used to partially replace expensive experiments in space.

1.1.4 Application of Phase Change Process Modeling in Studying

Ablation of Entry Objects

In studying the objects that enter the earth's atmosphere, useful information can be obtained from trajectory models. It is common to hypothesize about the nature of an entry object, and then use a trajectory model to simulate its path, and then compare the results with what was observed.

An accurate trajectory model must include an evaluation of both the mechanical fragmentation and the aerothermal ablation since both processes reduce the body's initial kinetic energy. Unfortunately, accurate calculation of the rate of ablation mass loss is extremely difficult, since it requires knowledge of the temperature distribution in the shock layer, the chemical composition of the meteor, and the degree to which the ablation products block radiative heat transfer to the body. Therefore, the trajectories predicted by using different ablation models, significantly differ for a given meteor. Inaccuracies in the calculated ablation rate can lead to substantial errors in the predicted terminal altitude of a given entry body, [4]. An accurate and efficient numerical phase change simulator could be part of a broader program for accurately modeling these trajectories.

1.1.5 Application of Phase Change Process Modeling in Aircraft Icing

In flight, icing on an aircraft surface occurs when the plane flies through a cloud of supercooled water droplets. A portion of the water droplets impinges on the aircraft components and results in ice formation. The growth of ice on an aircraft wing results in a

sharp increase in drag and a reduction in lift. Ice accretion can seriously degrade aircraft performance and handling characteristics. Icing has been implicated in a number of serious commercial aircraft accidents in recent years.

From a thermodynamic standpoint, two types of ice accretion mechanisms have been identified, resulting in physically and geometrically different formations. Immediately upon impact, the droplets freeze either partially or completely. The released latent heat of fusion then, tends to warm the accreted ice and the underlying solid surface towards the fusion temperature. This warming tendency is counteracted by convective heat loss to the ambient air. The resulting energy balance between these two factors then, determines the impact region's temperature. In cold temperatures with low liquid water content, temperature of the accreted ice remains below the fusion temperature and the impacting ice droplets freeze completely. This is known as *rime icing*. On the other hand, with high liquid water content and/or air temperatures only slightly below the fusion temperature, the accreted ice is at the fusion temperature and only a part of the liquid water freezes upon impact. The unfrozen water, then, tends to run back and freeze downstream of where it impinged on the surface. Consequently, complex "lobster tail" shapes tend to develop. This is called *glazed icing*.

Rime icing is reasonably well understood and can be adequately simulated for most practical purposes while glaze icing is more complicated and much additional research is required before its computational simulations will be sufficiently accurate and reliable for most practical purposes, ([5], [5]). This is another area that a more accurate phase front capturing method could be of extreme value.

1.1.6 Application of Phase Change Process Modeling in Casting of Metals

In recent years, numerical modeling of casting solidification has received increasing attention because of its enormous potential to improve productivity of the metal casting industry by reducing the cost and time associated with the traditional, experimentally based, design of castings. This becomes especially important in the case of permanent mold casting where mold prototyping can be extremely expensive. The numerical modeling of casting solidification has also found its way to the field of dentistry and is reported to be a reliable design tool for optimization and preventing defects in tooth crowns and bridges, ([7], [8]).

Although computer simulations of solidification of casting offer a basis for predicting solidification patterns and casting defects, achieving accuracy is not easy to accomplish. Casting processes, are very difficult to model due to the complicated physics involved, which includes such phenomena as fluid mechanics with phase change, shrinkage and porosity, macrosegregation in alloys, heat transfer between the casting and the mold, and thermal stresses in the solidifying ingot. A further complicating factor is the fact that typical industrial parts have complicated geometries and thus three-dimensional modeling is necessary. Consequently, although qualitative agreement with experimental data is reported to be achieved in the literature, simulation times are reported to be large, [9]. Most of the numerical casting simulations in the literature are accomplished using finite element methods. An accurate and efficient alternative phase change scheme can be notably more efficient for this class of applications.

1.1.7 Application of Phase Change Process Modeling in Cryosurgery

Cryosurgery, introduced in 1961, uses localized freezing/thawing cycles to destroy tissue. The procedure has found several areas of application including treatment of benign and cancerous prostate growth, liver cancer, breast cancer, skin cancer, Parkinson's disease, kidney cancer, abnormal brain, cervical growth, and lung cancer. Cryosurgery is desirable because of its medical and economical advantages including low bleeding, good esthetic results, minimal use of anesthetics, short period of recovery, and low procedural costs, [10].

Cryosurgery uses one or more cryosurgical probes, inserted into the patient's body at the desired point of application. Cryoprobe are small, hollow cylindrical devices, 2-10 mm in diameter, through which a cryofluid, typically liquid nitrogen, flows at a controlled rate.

The objective of procedure is to completely freeze and destroy the tumor or benign tissue while minimizing the amount of healthy tissue destruction, [11]. The degree of success in a cryosurgical procedure depends on a number of factors such as the lowest temperature achieved, the cooling rate during freezing, the thawing rate following the freezing process, probe placement, the number of repeated freezing/thawing cycles, and the cooling rate at the freezing front. As an example, it was observed that, the cryosurgical iceball shape and size is greatly affected by the cryoprobe placement and operation, [12]. Also a pioneering analytical and numerical study of cryosurgery related to lung cancer, by Bischof, Bastacky and Rubinsky in 1992, revealed that the freezing front accelerates as it leaves the tumor and enters the surrounding healthy, low-density tissue. Therefore, monitoring, controlling and optimizing the involved parameters are vital. This is where a numerical simulation of freeze/thaw cycles can play an important role. In fact there are

computer-controlled devices designed to control the freezing front's temperature by controlling the cryoprobe's temperature, [10]. Real-time data processing in the simulation of the heat transfer process is a very useful feature of these devices. Three-dimensional real-time simulations, however, require excessive amounts of computational power. The device, introduced in [10], allows one-dimensional simulations. Upgrading to a faster processor is suggested in order to be able to perform two-dimensional simulations. Obviously, a more efficient phase change scheme can also provide advances in this area.

1.1.8 Application of Phase Change Process Modeling in Cryopreservation of Cells and Organs for Transplantation

As an illustration in this class of applications, transplantation of isolated pancreatic islets is evolving into an effective treatment of patients with insulin-dependent diabetes mellitus. To date, a number of islet transplant recipients who have experienced insulin independence have received cryopreserved islets from a low-temperature bank. Successful cryopreservation of islet cells demands that the addition and removal of cryoprotectants as well as cooling and warming are carried out within certain biophysical and cell physiological tolerance limits. These limits have not yet been fully defined. Cells shrink transiently upon the addition of cryoprotective agents and then re-swell as the cryoprotectant permeates. Cells undergo a second shrinkage when cooled at rates low enough to preclude intracellular freezing as growing extracellular ice concentrates the solutes in the diminishing volume of non-frozen water, causing exosmosis. The cells return once again to their normal volume during warming and thawing. Finally, cells undergo a

potentially damaging osmotic volume excursion during the removal of the cryoprotectant. Therefore, accurate and efficient treatment of the freezing/thawing in the extracellular solute plays an important role in the calculation of lethal volume changes in cells. Furthermore, simulations can help provide knowledge to prevent intracellular freezing during cooling, [13].

The applications described above do not completely cover the realm of phase change processes. Other applications can be mentioned including formation of ice on the oceans; simulation of growth and decay of permafrost regions [14]; drilling and mining in permafrost regions where the rocks are held together by permafrost [15]; welding of metals and its control in order to reduce defects such as solidification cracking ([16], [17]); separating highly soluble salts from their aqueous solution through freezing in wastewater purification ([18], [19]); latent heat thermal storage systems and their usage where heat supply and heat demand are out of phase ([20]-[22]) as well as in maintaining a system's temperature in its operating range [23]; melting of fuses in electrical applications; cooling of electronic equipments using latent heat of fusion; deep freezing of food in food processing industry and its control in order to maintain the original characteristic of the fresh food.

In fact it is interesting to note that solid-liquid phase change problems belong to an even broader class of problems with numerous other applications. The feature that distinguishes this broader class is the subject of the next section.

1.2 Moving (Free) Boundary Problems

Many problems in various areas of applied science can be modeled using ordinary or partial differential equations posed in domains whose boundaries are to be determined as part of the problem. Depending on whether these boundaries are stationary or moving, such problems are usually referred to as free or moving boundary problems, respectively.

Free or moving boundary problems are, in general, harder to solve, either analytically or numerically, than the underlying differential equations would be in a prescribed domain. In particular, two separate solutions of such problems cannot be superposed, and this inherent non-linearity means that there is a dearth of analytical solutions, [24]. Moving boundaries can suddenly vanish, or appear, or move with infinite speed, or become blurred, all causing complications in the problem.

Problems of this kind arise in many fields such as fluid mechanics (shock waves, inviscid flow, slow (Hele-Shaw) flow, flow of liquids and gases in porous media), molecular diffusion, solid mechanics (frictional and contact problems), lubrication, and heat conduction with melting/freezing.

The scientists who developed the subject to its present shape, and where to find the details of their work, are reviewed briefly in the next sections.

1.2.1 Historical Background of Moving Boundary Problems

Moving boundary problems are often called Stefan problems, with reference to the early work of Jožef Stefan (1835-1893) on solid-liquid phase change published in six treatises

between the years 1889 and 1891. The solid-liquid phase change story, however, had begun a century earlier by the Scottish medical doctor, physician and chemist Joseph Black (1728-1799) in a series of experiments performed with water and ice at the University of Glasgow between the years 1758 and 1762. He demonstrated that solid-liquid phase change processes could not be calorically understood within the framework of sensible heat alone. As a consequence he introduced the term and the concept of *latent heat*.

French mathematician and physicist Jean Baptiste Joseph Fourier (1768-1830) provided the necessary physics and mathematics for heat conduction in his “La Théorie Analytique de la Chaleur”, published in 1822. The idea of how to analytically incorporate latent heat in heat conduction equations was first explained in a pioneering paper by the physicist Gabriel Lamé (1795-1850) and the mechanical engineer Emile Clapeyron (1799-1864) in 1831. This work presents an extension of the earlier work by Fourier, which tried to produce a rough estimate of the time elapsed since the earth began to cool from the initially molten state without considering solidification. Franz Neumann (1798-1895) also solved a similar problem in the early 1860s [25].

Classical Formulation

Jožef Stefan, in addition to Lamé, Clapeyron, and Neumann, contributed importantly to establishing the roots of the subject [25]. In 1889, Stefan in his work on the freezing of the ground posed and solved the following two problems.

- 1) A material that changes phase at a single fusion temperature T_f , and transmitting heat only by conduction, fills the half-space $x > 0$. At the initial time it is at the

constant temperature $T_i = T_f$. At the surface $x = 0$ it is maintained at constant temperature $T_w < T_f$, under the effect of which freezing arises isothermally, without supercooling. Volume change effects are neglected. When $T_i = T_f$, this problem is called the *one-phase Stefan problem* because only one phase is active and the other phase, where present, remains at the fusion temperature.

Clearly few realistic phase-change processes will actually lead to a single-phase situation, with ablation (instantaneous removal of melt) and induced stirring of liquid while freezing, being notable exceptions. On the other hand, molecular diffusion, filtration, and other processes commonly lead to single-phase problems [26], [24]. When $T_i > T_f$, however, both phases are active and the problem is called the *two-phase Stefan problem*:

- 2) The heat conducting material described above occupies the space $-8 < x < 8$. At the initial time the liquid phase fills the domain $0 < x < 8$ at temperature $T_L > T_f$, while the solid occupies the domain $-8 < x < 0$ at temperature $T_S < T_f$. The remaining conditions are the same as in the first problem.

Classically formulated, the two-phase Stefan problem can be described mathematically by the heat conduction equation in each phase plus the Stefan condition, (which can be derived from a global energy balance [27]) at the interface. Consider, for example, a semi-infinite slab $0 = x < 8$, initially solid at a uniform temperature $T_S = T_f$. By imposing a constant temperature $T_L > T_f$ on the face $x = 0$, melting starts from the left. The mathematical formulation can be written as

In melt region:

$$\frac{\partial T}{\partial t} = \mathbf{a}_L \frac{\partial^2 T}{\partial x^2}, \quad 0 < x < X(t), \quad t > 0 \quad (1.1)$$

In solid region:

$$\frac{\partial T}{\partial t} = \mathbf{a}_s \frac{\partial^2 T}{\partial x^2}, \quad X(t) < x, \quad t > 0 \quad (1.2)$$

Interface temperature:

$$T(X(t), t) = T_f, \quad t > 0 \quad (1.3)$$

Stefan condition:

$$\mathbf{r} L_f \frac{dX(t)}{dt} = -k_L \frac{\partial T}{\partial x}(X(t)^-, t) + k_s \frac{\partial T}{\partial x}(X(t)^+, t), \quad t > 0 \quad (1.4)$$

Initial conditions:

$$T(x, 0) = T_s < T_f, \quad x > 0, \quad X(0) = 0 \quad (1.5)$$

Boundary conditions:

$$T(0, t) = T_L > T_f, \quad \lim_{x \rightarrow \infty} T(x, t) = T_s, \quad t > 0 \quad (1.6)$$

where T denotes temperature, t is time, x is the spatial coordinate, and L_f , \mathbf{r} , X , k , and \mathbf{a} are latent heat of fusion, density, interface location, conductivity, and diffusivity, respectively. Subscripts, L and S , refer to the liquid and the solid, respectively.

That reasonably general one-dimensional Stefan Problems are well-posed, i.e., they have a unique classical solution depending continuously on the data, was established only during the mid 1970's! [28]. Local solvability (meaning: there exists a time t^* up to which a

unique classical solution exists) was proved by Rubinstein in 1947 (see [26] for a historical survey of the mathematical development up to the mid 1960's).

The classical formulation of Stefan problems as models of basic phase-change processes was presented in the above. Under certain restrictions on the parameters and data such problems admit explicit solutions in closed form. These simplest possible, explicitly solvable, Stefan problems form the backbone of our understanding of all phase-change models and serve as the primary means of validating approximate and numerical solutions of more complicated problems. Unfortunately, closed-form explicit solutions (all of which are of similarity type) may be found only under the following very restrictive conditions: semi-infinite (and usually one-dimensional) geometry, uniform initial temperature, constant imposed temperature (at the boundary), and constant thermophysical properties in each phase, [27].

Stefan-type problems can also be formulated classically in two or three dimensions [27] but such formulations may admit no (classical) solution. Even one-dimensional problems with either internal sources or a variable fusion temperature may develop mushy regions rendering the above sharp-front classical formulation inappropriate. Fortunately *weak* or *generalized (enthalpy)* formulations, which are well-posed (and computable), came to the rescue in the early 1960's. Furthermore, since explicit and approximate solutions are obtainable only for simple problems and only in one space dimension while most realistic phase-change processes do not neatly fall in this category, the modeling of such processes may only be attacked numerically, [27].

Before closing this discussion of the classical formulation and beginning the next chapter of the phase-change story, i.e., numerical methods and enthalpy formulation, it is worthwhile to mention excellent references that cover documented details of phase change background: Surveys of the early literature with numerous references dating from the time of Stefan have been written by Bankoff [29] and Muehlbauer and Sunderland [30]. Rubinstein's classic book [26] gives a systematic presentation of the mathematical developments in Stefan problems up to that time. A later survey is given by Fox (1979) [31], with useful bibliographies. Reports on several conferences ([32]-[36]) contain accounts of mathematical developments and of wide-ranging applications to problems in physical and biological sciences, engineering, metallurgy, soil mechanics, decision and control theory, etc. which are of practical importance in industries [33]. More recent surveys can be found in [27] and [37].

Numerical Methods

Numerical methods for the phase change problems are designed to be suitable for one of three main approaches, namely *front fixing*, *front tracking*, and *front capturing* methods. This section, offers a brief discussion on front fixing and front tracking methods, usually used for numerical modeling of phase change problems, based on the classical formulation.

Front Fixing Methods

This approach is based on the Landau transformation. By a change of variables

$$\mathbf{x} = x / X(t) \tag{1.7}$$

where $X(t)$ is the interface location, the interval $0 = x = X(t)$, is mapped onto the fixed interval $0 = x = 1$. Using this mapping, the geometric non-linearity of the problem is eliminated. The governing equations, on the other hand, become explicitly and algebraically non-linear, [27]. Then one solves the resulting system of nonlinear equations by some numerical method.

The above transformation was proposed by H. G. Landau in 1950 and first implemented using a finite-difference scheme by J. Crank in 1957. The one-dimensional transformation introduced above is a simple case of more general transformations that map curved shape regions, in two or three dimensions, onto fixed rectangular domains and are commonly called body-fitted curvilinear transformations. A particular case of the curvilinear transformations is the isotherm migrations method (IMM), in which the dependent variable T , i.e., the temperature, is replaced with one of the space variables, e.g., x . In other words, IMM, instead of expressing the time-dependence of temperature at a specific x , expresses how a specified isotherm moves in the field. The IMM is particularly suited to melting and freezing because phase front itself is an isotherm, provided the phase change takes place at a constant temperature [33]. More details as well as the historical background are available in [33].

Front Tracking Methods

Due to the underlying geometric nonlinearity of the problem, several approaches have been devised with the aim of separating the problem into time-varying regions in which heat conduction equation is to hold, and to compute the location of the interface $x = X(t)$

concurrently. These methods are referred to as front tracking schemes, because they attempt to explicitly track the interface using the Stefan condition, [27].

These methods compute, at each step in time, the location of the moving boundary. Using standard numerical methods, generally, the moving boundary will be located somewhere between the grid nodes and not necessarily exactly on them. Consequently special formulae are needed for calculation of derivatives. One approach is to fix the spatial step, but allow the time step, to float in such a way that the front always passes through a grid node. An example of this approach is the method of Douglas and Gallie [38]. Another approach is to fix the time step and allow the spatial step to float, in fact, use two distinct and time-varying space steps for the two phases. In these methods, e.g., the method of Murray and Landis the number of space intervals is kept constant between a fixed and a moving boundary. This way the moving boundary is on a grid node at all times [33]. For more details and other methods of this category, as well as the historical background, see [33]. Surveys of front tracking methods also appear in [39] and [35].

Difficulties Associated with the Front Fixing and Front Tracking Methods

All of these methods are effective for simple Stefan Problems set in the geometries where a sharp front is expected to appear. In more realistic problems, it may sometimes be difficult or even impossible to track the moving boundary directly if it does not move smoothly or monotonically with time [33]. Presence of a time-dependent heat source (or sink) may cause multiple fronts and disappearing phases; mushy zones may appear, etc. In other

words, a real life phase change problem can easily become complicated enough to make a classical, sharp front formulation impractical.

Moreover, front tracking methods often require complicated starting solutions [40]. Considering the difficulties that could occur for a slightly complicated one-dimensional phase change problem, one can easily imagine how difficult treatment of such multi-dimensional problems in this manner would be. The moving boundary may have sharp peaks, or double back, or it may even disappear. The possibility, therefore, of reformulating the problem in a new form of the equations, which applies over the whole of a fixed domain, is an attractive one [33]. Fortunately a more general and versatile class of methods is available for formulation of phase change processes: *the enthalpy formulation*.

Enthalpy Formulation

This method of formulation eliminates the difficulties associated with the above approaches because it bypasses the explicit tracking of the interface. The Stefan condition is not enforced, but obeyed automatically. The enthalpy method is based on the method of weak solutions. Weak solutions nucleated in late 1800's when David Hilbert first introduced the idea of generalized solutions for the partial differential equations (PDE's). Traditionally, a solution to a PDE was regarded as a continuous function with continuous derivatives that satisfied that PDE in its domain of application. In the late 1800's, however, the need arose to weaken these conditions and to define continuity at every point, in a more general way, by integrability over a set. The initiated ideas further evolved in the 1930's and 1940's, mainly in the context of the calculus of variations and also in problems described in terms

of hyperbolic PDE, e.g., shock waves. The Stefan problems, however, were introduced to the subject much later due to their highly non-linear and non-standard PDE types. The use of enthalpy was proposed by Eyres et al. (1946) and later by Price and Slack (1954) [33]. It was Kamin (1958) and Oleinik [41] who first introduced a weak formulation of the Stefan problem, while enthalpy-based numerical methods were first proposed in [42]-[44]. For more details on the history and mathematics of the subject see [27].

The enthalpy formulation in its simplest form can be presented as follows. Consider the governing equation in a three-dimensional Cartesian coordinate system, i.e., the conservation of energy, with the assumption of constant thermophysical properties within each phase (the Fourier-Biot equation)

$$\mathbf{r} c \frac{\partial T}{\partial t} = \frac{\partial}{\partial x} \left(k \frac{\partial T}{\partial x} \right) + \frac{\partial}{\partial y} \left(k \frac{\partial T}{\partial y} \right) + \frac{\partial}{\partial z} \left(k \frac{\partial T}{\partial z} \right) + \dot{q} \quad (1.8)$$

where c , k , and \mathbf{r} are specific heat, thermal conductivity and density of the material, respectively, and \dot{q} refers to a distributed heat source (or sink) that may be present in the domain. The left hand side of the above equation is related to the change of enthalpy. The specific enthalpy may be defined as

$$\bar{h} = \int_0^T c dT + \mathbf{f} L_f \quad (1.9)$$

where L_f is the latent heat of fusion and \mathbf{f} equals 1 for liquids and 0 for solids. Using the above definition, the governing equation can be written as

$$\frac{\partial H}{\partial t} = \frac{\partial}{\partial x} \left(k \frac{\partial T}{\partial x} \right) + \frac{\partial}{\partial y} \left(k \frac{\partial T}{\partial y} \right) + \frac{\partial}{\partial z} \left(k \frac{\partial T}{\partial z} \right) + \dot{q} \quad (1.10)$$

where $H = \mathbf{r} \bar{h}$ is the enthalpy per unit volume. To use the above equation when both solid and liquid phases are involved, procedures are needed for both choosing the thermal conductivity and calculating the temperature field from the enthalpy field. Since c is assumed to be constant within each phase, the enthalpy of the liquid and solid, for a material that changes phase at a single temperature T_f , can be calculated from Eq. (1.9) as

$$\begin{aligned} H_s &= \mathbf{r}_s \left(\int_0^T c_s dT \right) = \mathbf{r}_s c_s T \\ H_L &= \mathbf{r}_L \left(\int_0^{T_f} c_s dT + \int_{T_f}^T c_L dT + L_f \right) \\ &= \mathbf{r}_L (c_s T_f + c_L (T - T_f) + L_f) \end{aligned} \quad (1.11)$$

where subscripts L and S refer to liquid and solid phases, respectively. Therefore, the temperature field can be calculated using the above equation as follows

$$T = \begin{cases} \frac{H}{\mathbf{r}_s c_s} & H \leq H_{sf} \\ \frac{T_f}{\mathbf{r}_s c_s} & H_{sf} \leq H \leq H_{lf} \\ \frac{(H - H_{lf})}{\mathbf{r}_L c_L} + T_f & H \geq H_{lf} \end{cases} \quad (1.12)$$

where $H_{lf} = \mathbf{r}_L (c_s T_f + L_f)$ and $H_{sf} = \mathbf{r}_s c_s T_f$ are enthalpies of the fusion liquid and fusion solid, respectively. These values can also be used in the numerical approach for determining whether each grid element is solid, liquid or undergoing melting/freezing. Corresponding thermal conductivities are then chosen for that grid element.

Problems associated with the numerical modeling of the enthalpy method

Numerical application of these methods produces better results when the phase change occurs within a temperature range. For situations where the phase change occurs at a single temperature, the phase front is a moving discontinuity. Consequently all of these methods need special (and most of the time case-dependent) adjustments in order to achieve convergence, to maintain stability of the numerical solution [45], and to avoid oscillations in the location of the interface. Usually, for suppressing these oscillations, schemes need to be modified by incorporating a certain amount of artificial dissipation into the numerical method. This, however, has a dilatory effect on the solution in the smooth regions and the overall accuracy is consequently reduced. The ideal scheme would automatically add the artificial dissipation, only in the vicinity of the discontinuities, (which are located in a previously unknown region), and not affect the smooth regions. Has such a method ever been designed? The simple answer is yes. In another, not far remote discipline, not very long ago, a modern concept initiated what, we suggest, has the potential to be used for designing a very effective and generally applicable phase change scheme. This scheme will be introduced in the next chapter.

Another well-known weakness mentioned for numerical simulations of the enthalpy method is a convergence and accuracy problem at small Stefan numbers (the Stefan number is defined as the ratio of sensible to latent heat), [46]. Thus, for a new alternative general phase change solver, it is also necessary to consider its behavior at the limit of small Stefan numbers.

1.3 The Space-Time Conservation Element and Solution Element Method - An Innovative Numerical Scheme for Fluid Mechanics Problems

In 1991, at the NASA Glenn Research Center, Dr. Sin-Chung Chang introduced a new method for solving the conservation laws in fluid mechanics [47]-[49]. Compared to other numerical methods known to-date, the so-called space-time conservation element and solution element (CE/SE) method possesses a distinguishing¹ feature: it treats the domain of application of the PDE's in a way that is most consistent with the physical nature of the universe we live in. In other words, the CE/SE method sees the universe as a space-time continuum and naturally treats the space and time directions similarly. As a very brief definition, this method could be thought of as a means of solving the integral form of the conservation laws over a space-time domain.

Between 1991 and today (2004), the CE/SE method has been applied to a range of PDE's, mainly in the area of fluid mechanics. An overview of these applications, through which the interesting and unique features of the method were observed and studied, are the subject of the next sections.

¹ Certain finite element methods, e.g., Discontinuous Galerkin (DG) methods, share some of the features mentioned for the CE/SE scheme. For detailed comparison of the CE/SE scheme to the traditional schemes see [79]].

1.3.1 The CE/SE Method's History

A brief review of the advances of the space-time CE/SE method, since its inception, helps to provide an overall picture of the method's capabilities. The fact that the CE/SE method is being successfully applied to disciplines other than that where it originated from, presents a strong confirmation of the method's robustness and generality. The following contains some of these applications that have appeared to date.

In 1993, the CE/SE method was applied to Euler and Navier-Stokes equations in one spatial dimension [50]. The shock tube problem was then studied using this method [51]. At the same time the scheme was extended to two-dimensional time-marching problems [52].

In 1995, the method was extended in order to solve two-dimensional advection-diffusion problems [53]. An implicit solver was also built based on the concept [54]. The CE/SE method's application in axisymmetric Euler time-marching problems appeared [55], and research started to apply it to aeroacoustics problems [56].

In 1996, flows caused by shock-body interactions were studied using the CE/SE method [57]. Its application in unsteady flows with chemical reactions started in 1997. Among the new applications that appeared in 1998 are: shock reflection over a dust layer [58], free shear flows, and ZND detonations [59]. Further, a CE/SE scheme, suitable for two-dimensional unstructured triangular grids, was proposed [60], and a dam-break and a hydraulic jump were simulated using the method [61]. The study of unstable detonations using the CE/SE method continued in 1999 [62], along with further applications in the simulation of vortex dynamics in aeroacoustics [63]. It was in this year that three-

dimensional structured and unstructured CE/SE Euler solvers were developed ([64], [65]). Moreover, the method was extended to two-dimensional viscous flows [66] and also used as a new alternative for the NCC (National Combustion Code) solver ([67]-[69]).

Propagation of sound waves through a nozzle with/without a shock wave was resolved using the CE/SE method in 2000 [70]. Further applications in this year also include aeroacoustic computations of supersonic jets ([71], [72]), along with successful attempts for parallel computation [73] and local mesh refinement [74]. In addition to more recent applications in inviscid and axisymmetric flows, ([75], [76]), the CE/SE method has been applied to the solution of Maxwell's equations for electrical engineering problems [77].

A mathematical discussion on the convergence and error bound analysis of the CE/SE method applied to a one-dimensional time-dependent convection-diffusion equation is available in [78].

The studies and applications of the CE/SE method, during these years, proved and reproved a number of distinguishing features that are summarized in the next section.

1.3.2 The CE/SE Method's Features

The applications mentioned above, in addition to establishing the effectiveness, robustness and accuracy of the CE/SE method, revealed that it possesses low dissipation and low dispersion errors in spite of its second order accuracy.

Furthermore, the method was shown to be capable of capturing discontinuities without resorting to special treatments [68], without oscillations and without affecting the smooth solution within the region. This was best demonstrated in the method's capability of

resolving weak disturbances along with strong discontinuities. This is in fact due to a dissipation term that can be introduced in the scheme for automatically suppressing the unwanted oscillations close to the discontinuities while being automatically negligible in the smooth regions.

Among other favorable features of the CE/SE method, is the fact that its underlying concept is easy to implement and easy to extend to higher dimensions. Furthermore, computationally efficient explicit methods can be designed based on it, a feature vital to the treatment of three-dimensional problems. Finally, the method is adaptable to unstructured grids, a feature that simplifies treatment of complex geometries. It is also worthwhile to briefly compare the CE/SE method to the well-known traditional computational methods.

In comparison with traditional computational methods.

The CE/SE method's both underlying concept and methodology of application are different from finite difference, finite element, finite volume, and spectral computational methods.

In particular, finite difference, and spectral methods deal with the differential conservation laws. This feature, as mentioned in the comparison between classical and weak formulations, introduces fundamental disadvantages when treating discontinuities. The CE/SE method treats the integral equations.

Furthermore, traditional methods either do not enforce flux conservation or enforce it in space only. Finite volume methods treat the integral form of conservation laws and can be designed to enforce flux conservation in both space and time. This process, however, involves the ad hoc choice of a special flux evaluation model among many available

models. In the CE/SE method, on the other hand, flux conservation is enforced both locally and globally over space and time. This flux conservation enforcement is an integral part of the process and no interpolation/extrapolation is needed. The CE/SE, in contrast to traditional methods, is discussed in detail in [79].

1.4 Outline of dissertation

The remaining chapters are organized as follows: Chapter 2 is devoted to problem statement and its physical modeling. It contains a brief introduction to the physical phenomena involved in phase change, underlying assumptions used in modeling and their evaluation, and finally the enthalpy formulation for both isothermal phase change and phase change over a temperature range.

Chapter 3 provides the development of a one-dimensional CE/SE phase change solver. It contains analytical studies on the equivalence of the CE/SE formulation with the classical formulation, as well as the stability of the method. It also contains numerical studies on the convergence and accuracy of the method.

Chapter 4 presents the development of a two-dimensional CE/SE phase change solver. It contains a detailed derivation of the method on unstructured grids, as well as detailed numerical studies on the convergence and accuracy of the method.

Chapter 5 presents an axisymmetric version of the solver, since many phase change problems can be modeled as axisymmetric. This chapter explores axisymmetric formulation options and spots the option leading to a stable efficient solver. In addition to

the derivation, numerical confirmations are also presented on the convergence and accuracy of the axisymmetric scheme.

Chapter 6 presents the development of a three-dimensional CE/SE phase change solver. It contains a detailed derivation of the four-dimensional space-time scheme needed for solving phase change problems in three spatial dimensions. As presented in the previous chapter, the convergence and accuracy of the three-dimensional scheme is also assessed numerically, by comparing the results to the available analytical and semi-analytical solutions for specific benchmark problems.

Chapter 7 addresses the second difficulty associated with the numerical modeling of the enthalpy method, i.e. the limit of small Stefan numbers. As demonstrated in Chapter 4, the numerical simulation of the Stefan problem using the CE/SE method is capable of providing accurate results for both large and small Stefan numbers. However, for small Stefan numbers, the accuracy had to be improved by using an alternate method for calculation of the first-order derivative terms. The original CE/SE phase change scheme, like other numerical schemes for the enthalpy method, loses its second-order accuracy and becomes dissipative for small Stefan numbers. The dissipation, nevertheless, is adjustable. The adjustment, that was employed in order to obtain accurate results for small Stefan numbers, is an *ad hoc* feature and therefore undesirable. Recently, space-time CE/SE methods have been designed to solve fluid flow problems without being sensitive to the size of the Courant number ([80], [81]). Using an analogous concept, it is possible to design a CE/SE scheme that is, to a considerable degree insensitive to the size of the Stefan number. In this chapter, the one-dimensional analytical studies of Chapter 3 are summoned

again, and the dissipation of the original method is studied through numerical experiments. The new insensitive CE/SE scheme is then described for numerical simulation of phase change problems. A single-phase Stefan problem is selected as a benchmark problem for comparing the behavior of the original and the new scheme. Finally, the convergence and accuracy of the new scheme is assessed without any case-dependent adjustment.

Chapter 8 is in reality only a starting point for future work towards construction of a general phase change solver based on the previous developments. In this chapter, the consideration of density driven body force problems is made. A full CE/SE Navier-Stokes solver is derived. The program is validated for some standard benchmark fluid flow problems, and is proved to be accurate and ready to be extended to study phase change phenomenon.

The intention of this work is to lay the foundation for the design of a new generation of more accurate, more efficient, and more generally applicable numerical schemes for moving boundary problems and, in particular, to phase change problems.

Chapter 2

PROBLEM STATEMENT AND FORMULATION

A model can at best be as good as its underlying assumptions [27]. Therefore, the problem formulation needs to start by first providing a clear picture of which phenomena are to be taken into account and which are not, and errors introduced because of the model simplifications. Thus, in this chapter, an overview of the phenomena involved in a solid-liquid phase change process is briefly presented and the relevant terminology introduced. Then a summary of contributions of the mentioned phenomena to the model is given. The problem is then modeled using the Enthalpy Formulation.

2.1 Physical Phenomena Involved in Solid-Liquid Phase

Change processes

Both solid and liquid phases are characterized by the presence of cohesive forces that keep atoms in close proximity. In a solid the molecules vibrate around fixed equilibrium positions, while in a liquid they are freer to move between these positions. The

macroscopic manifestation of this vibrational energy is what we call heat or thermal energy. Clearly atoms in the liquid phase are more energetic than those in the solid phase, all other things being equal. Thus before a solid can melt it must acquire a certain amount of energy to overcome the binding forces that maintain its solid structure. This energy is referred to as the latent heat of fusion of the material and represents the difference in enthalpy levels between liquid and solid states, all other things being equal. Of course, solidification of liquid requires the removal of this latent heat and the structuring of atoms into more stable lattice positions [27].

The phase-transition region where solid and liquid coexist is called the interface. Its thickness may vary from a few Angstroms to a few centimeters, and its microstructure may be very complex, depending on several factors (the material itself, the rate of cooling, the temperature gradient in the liquid, surface tension, etc.). For most pure materials solidifying under ordinary freezing conditions at a fixed T_f , the interface appears (locally) planar and of negligible thickness. Thus, it may be thought of as a *sharp front*, a surface separating solid from liquid at temperature T_f . In other cases, typically resulting from supercooling, or presence of multiple components (e.g. in binary alloys), the phase transition region may have apparent thickness and is referred to as a "mushy zone"; its microstructure may now appear to be dendritic or columnar (shown schematically in Figure 2.1).

Several mechanisms are at work when a solid melts or a liquid solidifies. Such a change of phase involves heat (and often also mass) transfer, possible supercooling, absorption or release of latent heat, changes in thermophysical properties, surface effects, etc [27]. A qualitative discussion of these follows.

2.1.1. Heat and Mass Transfer

There are three possible modes of heat transfer in a material: conduction, convection and radiation. Conduction is the transfer of kinetic energy between atoms by any of a number of ways, including collision of neighboring atoms and the movement of electrons; there is no flow or mass transfer of the material. This is how heat is transferred in an opaque solid. In a liquid heat can also be transferred by a flow of particles, i.e. by convection. Radiation is the only mode of energy transfer that can occur in a vacuum (it requires no participating medium) [27].

2.1.2. Variation of Phase Change Temperature

The transition from one phase to the other, that is, the absorption or release of the latent heat, occurs at some temperature at which the stability of one phase breaks down in favor of the other according to the available energy. This phase change, or melt temperature T_f , depends on pressure. For a fixed pressure, T_f may be a particular fixed value characteristic of the material (for example, 0°C for pure water freezing under atmospheric pressure), or a function of other thermodynamic variables (for example, of glycol concentration in an anti-freeze mixture) [27].

2.1.3. Supercooling

Most solids are crystalline, meaning that their particles (atoms, molecules, or ions) are arranged in a repetitive lattice structure extending over significant distances in atomic terms. In this context atoms may be regarded as spheres of diameter 2 to 6 Angstroms (1 Angstrom = 10^{-10} meters). Since formation of a crystal may require the movement of atoms into the solid lattice structure, it may well happen that the temperature of the material is reduced below T_f without the formation of a solid. Thus, supercooled liquid, i.e., a liquid at temperatures

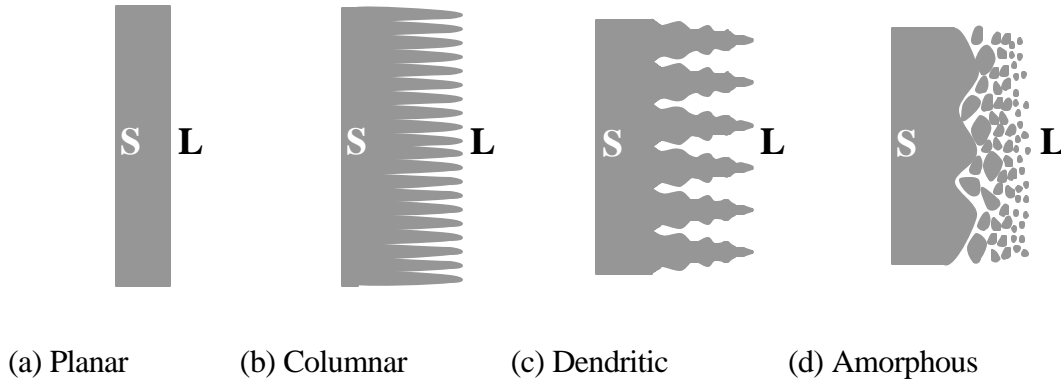


Figure 2.1: Different microstructures of the solid-liquid phase interface

below T_f may appear; such a state is thermodynamically *metastable* [82], [83]. We note that melting requires no such structuring, possibly explaining why *superheating* is rarely observed. When crystallization does take place, if the latent heat released upon freezing is sufficient to raise the temperature to T_f , i.e., the liquid was not cooled too much, the temperature rapidly rises back to the melt temperature T_f . Liquid cooled to a temperature so low that the latent heat is not sufficient to raise its temperature to T_f is referred to as being *hypercooled* [27].

2.1.4. Variation of Thermophysical Properties

Most thermophysical properties of a material (usually varying smoothly with temperature) undergo more or less sudden changes at T_f . For example the heat capacity of aluminum changes by 11 % at its melt temperature (of 659°C), but that of silicon changes by only 0.3% (at 1083°C). Such discontinuities in thermophysical properties complicate mathematical problems because they induce discontinuities in the coefficients of differential equations. However the most fundamental and pronounced effects are due to changes in density [27].

2.1.5. Density Changes

Typical density changes upon freezing or melting are in the range of 5% to 10% but can be as high as 30%. For most materials the solid is denser than the liquid, resulting in possible formation of voids in freezing or breaking of the container in melting. On the other hand water expands on freezing, resulting in broken pipes on cold days and ice floating instead of filling the bottom of the oceans. The density variation with temperature induces flow by natural convection in the presence of gravity, rapidly equalizing the temperature in the liquid and greatly affecting heat transfer. In microgravity there is no natural convection but *Marangoni* convection [84], due to surface tension (capillary) effects, may arise instead and dominate heat transfer. All these effects may complicate a phase-change process beyond our ability to effectively analyze them [27].

2.2 Underlying Assumptions

The phase change process considered here involves a PCM (phase change material) with constant latent heat of fusion L_f . Supercooling effects and nucleation difficulties are assumed not to be present.

The specific heats c_L , c_s , and thermal conductivities, k_L , k_s are assumed phase-wise constant, allowing their discontinuity at the phase interface. This assumption is made only for convenience. In fact the structure of the numerical scheme, easily allows for their variation with temperature and/or spatial coordinates.

Heat is assumed to be transferred only by conduction. This is a reasonable assumption for pure materials in small containers and moderate temperature gradients. It is also worthwhile to mention that this assumption can be relaxed by adding the mass transfer equations and considering convection. The radiation heat transfer can also be added to the model for analyzing more complicated situations.

For most of the cases modeled here, the fusion temperature is assumed constant. Furthermore, most of the cases involve an isothermal phase change. The reason is that for such cases the interface represents a moving discontinuity, for which the performance of the numerical method needs to be studied. However, for generality, one case will be studied later, in which the change of phase occurs over a temperature range, rather than a single fusion temperature.

Density change due to phase transition is ignored. This is necessary in order to prevent the movement of the fluid part. As discussed above, this assumption, although reasonable

for many cases, may not be a good one for all cases. However, it helps to construct a less complicated phase-change solver in order to study the behavior of the numerical scheme. Once the scheme is well established, this assumption may be relaxed. This can be done either by adding the entire fluid flow equations to the model, or by solving the mass conservation equation on the interface, combined with modeling volume change effects.

2.3 Enthalpy Method

The enthalpy method is used for modeling heat conduction with phase change phenomenon. This method gives the solid-liquid interface as a part of the solution without explicit tracking.

It is interesting, from a historical perspective, to note that originally, this formulation was not introduced for treating phase change problems. It was first devised, by Eyres et al., as an alternative formulation for the heat conduction problems where the thermal conductivity varies with temperature. In fact it was used in conjunction with a method that was afterwards became known as the *Kirchoff transformation*.

The governing equation, i.e., the conservation of energy, with the assumption of constant thermophysical properties within each phase is the Fourier-Biot equation that for a system with no energy generation is written in vector form as

$$\mathbf{r} \cdot \mathbf{c} \frac{\partial T}{\partial t} = \nabla \cdot (k \nabla T) \quad (2.1)$$

where T is the absolute temperature, t denotes time, and c , k , and \mathbf{r} are specific heat, thermal conductivity and density of the material, respectively. The left hand side of the above equation is related to the change of enthalpy. The procedure of the enthalpy method starts by introducing an enthalpy function $H(T)$, which is the total heat content, i.e. the sum of the sensible heat and the latent heat of phase change. The specific enthalpy may be defined as

$$\bar{h} = \int_0^T c \, dT + \mathbf{f} L_f \quad (2.2)$$

where L_f is the latent heat of fusion and \mathbf{f} , is the so-called liquid fraction, which equals 1 for liquids and 0 for solids. Using the above definition, Eq. (2.1) can be written as

$$\frac{\partial H}{\partial t} = \nabla (k \nabla T) \quad (2.3)$$

where $H = \mathbf{r} \bar{h}$ is the enthalpy per unit volume. To use the above equation when both solid and liquid phases are involved, procedures are needed for both choosing the thermal conductivity and calculating the temperature field from the enthalpy field. The specific heat c is assumed to be constant within each phase. As mentioned in [85], the enthalpy can be calculated from Eq. (2.2) as

$$\begin{aligned}
H &= \mathbf{r}(1-\mathbf{f}) \int_0^T c_S dT + \mathbf{r}\mathbf{f}L_f \left[\int_0^{T_{sf}} c_S dT + L_f + \int_{T_{sf}}^T c_L dT \right] \\
&= \mathbf{r} [c_S - (c_S - c_L)\mathbf{f}]T + \mathbf{r}\mathbf{f}[(c_S - c_L)T_{sf} + L_f]
\end{aligned} \tag{2.4}$$

where subscripts L and S refer to liquid and solid phases, respectively. For an isothermal phase change, $T_{sf} \equiv T_f$ is the fusion temperature of the material. For a non-isothermal phase change, the fusion occurs over the temperature range $T_{sf} \leq T \leq T_{Lf}$, and the liquid fraction, \mathbf{f} , changes from being a step function to other forms that may or may not contain a discontinuity (see Section 2.5).

2.4 Isothermal Phase Change

For a material that changes phase at a single temperature T_f , the enthalpy of the liquid and that of the solid, can be calculated from Eq. (2.4) as

$$\begin{aligned}
H_S &= \mathbf{r}_S \left(\int_0^T c_S dT \right) = \mathbf{r}_S c_S T \\
H_L &= \mathbf{r}_L \left(\int_0^{T_f} c_S dT + \int_{T_f}^T c_L dT + L_f \right) \\
&= \mathbf{r}_L (c_S T_f + c_L (T - T_f) + L_f)
\end{aligned} \tag{2.5}$$

For this type of problem, the temperature field can be calculated using Equation (2.4) as follows

$$T = \begin{cases} \frac{H}{\mathbf{r} c_s} & H \leq H_{sf} \\ T_f & H_{sf} \leq H \leq H_{lf} \\ \frac{(H - H_{lf})}{\mathbf{r} c_L} + T_f & H \geq H_{lf} \end{cases} \quad (2.6)$$

where $H_{lf} = \mathbf{r}(c_s T_f + L_f)$ and $H_{sf} = \mathbf{r} c_s T_f$ are enthalpies per unit volume of the fusion liquid and the fusion solid, respectively. These values can also be used in the numerical approach for determining whether each grid element is solid, liquid or undergoing melting/freezing. Corresponding thermal conductivities are then chosen for that grid element. For elements that are undergoing phase change, an average thermal conductivity is used.

2.5 Phase Change over a Temperature Range

For this type of problem, when only one phase exists, the temperature can be calculated as explained above. In the mushy zone, however, the liquid fraction needs to be defined at each point. As mentioned in [86], the liquid fraction can be a function of a number of solidification variables. In many systems, however, it is reasonable to assume that the liquid fraction is a function of temperature alone, i.e.,

$$\mathbf{f} = \begin{cases} 0 & H \leq H_{sf} \\ \tilde{F}(T) & H_{sf} \leq H \leq H_{lf} \\ 1 & H \geq H_{lf} \end{cases} \quad (2.7)$$

where H_{sf} and H_{lf} are determined from Eq. (2.4) by substituting $(f = 0, T = T_{sf})$ and $(f = 1, T = T_{lf})$, respectively.

The function $\tilde{F}(T)$ can assume a number of possible forms, e.g., linear, power, etc., depending on the equilibrium phase diagram of the specific materials involved ([85], [86]).

Once the enthalpy field is determined using the numerical solver at each time step, the temperature field needs to be determined. Unlike the isothermal phase change case, an explicit expression may not be available for the temperature when $H_{sf} \leq H \leq H_{lf}$, due to the possible complexity of the function $\tilde{F}(T)$. Therefore, a subprogram needs to be linked to the main solver, for iterative treatment of Eq. (2.4) in the mushy zone. For this purpose, a number of iterative schemes were tried with different forms of $\tilde{F}(T)$. Although computationally efficient iterative schemes provide convergence for linear $\tilde{F}(T)$, difficulties arise while handling highly non-linear forms of $\tilde{F}(T)$. Extremely flat/steep portions of the liquid fraction curve can greatly slow convergence. In order to overcome this difficulty, the following numerical technique was used:

First a sorted array was generated for enthalpy over the mushy zone's temperature range. Then at each time-step, after updating the H -field, for each node that falls in the mushy zone, a bi-section search routine was used to determine the corresponding position within the pre-calculated enthalpy array. A linear interpolation then suffices for determining the temperature. While the bi-section search guarantees the computational efficiency of the routine, the discrete pre-calculated enthalpy array can be refined to

provide the desired accuracy. The discrete nature of pre-calculated enthalpy array eliminated the difficulties associated with the flat/steep portions of $\tilde{F}(T)$, and therefore, the routine is effective regardless of the specific shape of the liquid fraction curve. As an example, see section 3.4.3.

In the next chapter, numerical modeling of the problem is initiated, starting by development of a one dimensional CE/SE phase change solver.

Chapter 3

ONE-DIMENSIONAL CE/SE PHASE-CHANGE SCHEME

It is of value to start the application of the numerical method considering the simplest phase change problem, i.e., that of a one-dimensional Cartesian geometry. In this chapter, the equations describing this category of problems are briefly reviewed. The space-time CE/SE phase change scheme is then developed for the one-dimensional governing equations. The study of the behavior of the numerical scheme is divided into two parts: 1) Analytical study, and 2) Numerical study.

- 1) Analytical study of the scheme, presented here, contains three parts: a) a mathematical proof on the equivalence of the CE/SE formulation of the enthalpy method with the conventional formulation, both for cases without discontinuity and cases having a discontinuity in the domain, b) a von Neumann stability analysis on the linearized versions of the phase change scheme. This study leads to derivation of a necessary stability condition, c) a study of the dissipative and dispersive behavior of the numerical scheme for different Stefan numbers. Parts, (a) and (b) are presented in this chapter while part (c) is contained in Chapter 7.

- 2) Numerical study of the scheme consists of application of the actual phase-change scheme to several cases for which an analytical solution is available. This way, the accuracy of the method is assessed. It is also shown that no non-physical waviness is detected using this method, in predicted profiles for temperature and enthalpy. Further, a numerical study is presented on the convergence of the scheme for different time-steps, leading to a procedure for selecting the optimum time-step for the fastest convergence. Finally, one case is studied which involves phase change over a temperature range rather than a single fusion temperature.

At the end of this chapter, the knowledge extracted from the study of the one-dimensional scheme, provides the groundwork for extending the method, to higher dimensions and more general phase change problems.

3.1 Development of a One-Dimensional CE/SE Scheme for Heat Conduction with Melting/Freezing

The governing equation (Eq.(2.3)), for one spatial dimension, is written as

$$\frac{\partial H}{\partial t} = \frac{\partial}{\partial x} \left(k \frac{\partial T}{\partial x} \right) \quad (3.1)$$

Equation (2.6) can be used without change.

Considering (x, t) as the coordinates of a two-dimensional Euclidean space-time, the computational grid that is used here can be regarded as a staggered two-dimensional

rectangular mesh. Figure 3.1 shows the computational molecule of this grid for the grid node (j, n) . Define vector \vec{U} as

$$\vec{U} = (F, H) \quad (3.2)$$

where H is enthalpy per unit volume and

$$F = -k \frac{\partial T}{\partial x} \quad (3.3)$$

is referred to as the flux function. The integral governing equation can then be written as

$$I = \oint_{\Omega(CE)} \vec{U} \cdot \hat{n} d\mathbf{s} = 0 \quad (3.4)$$

where $\Omega(CE)$ is the boundary of the rectangle ACDF that represents the *conservation element (CE)* for node (j, n) , see Fig. 3.1(a). Vector $\hat{n} = (n_x, n_t)$ represents the unit outward normal to the *CE*, and $d\mathbf{s}$ denotes a line element on $\Omega(CE)$.

For discretization, enthalpy and the flux function are represented on each *solution element (SE)* [79], as

$$\Psi(x, t; j, n) = \Psi_j^n + (\Psi_t)_j^n (t - t^n) + (\Psi_x)_j^n (x - x_j) \quad (3.5)$$

where Ψ can be either H or F , and the notation $\Psi(x, t; j, n)$ is adopted from [87]. The subscripts x and t are shorthand notations for the corresponding derivatives.

Figure 3.1(b) provides a sketch of the solution element related to node (j, n) . The solution elements need to be defined in order to assign a unique discrete value to the field parameters at each grid node². Using the SE s, consider that the line segments FA and AB belong to $SE(j-1/2, n-1/2)$, that the line segments BC and CD belong to $SE(j+1/2, n-1/2)$, and that the line segment DF belongs to $SE(j, n)$. The unit outward normals are $\hat{n}_{AB} = \hat{n}_{BC} = (0, -1)$, $\hat{n}_{CD} = (1, 0)$, $\hat{n}_{DF} = (0, 1)$, and $\hat{n}_{FA} = (-1, 0)$. Equation (3.4) can then be written as

$$\begin{aligned}
 I = & \int_{AB} -H(x, t; j-1/2, n-1/2) dx + \int_{BC} -H(x, t; j+1/2, n-1/2) dx + \\
 & \int_{CD} F(x, t; j+1/2, n-1/2) dt + \int_{DF} H(x, t; j, n) dx + \\
 & \int_{FA} -F(x, t; j-1/2, n-1/2) dt = 0
 \end{aligned} \tag{3.6}$$

Using Eq. (3.5), the above becomes

$$\begin{aligned}
 I = & \int_{AB} -\left[H_{j-1/2}^{n-1/2} + (H_x)_{j-1/2}^{n-1/2}(x - x_{j-1/2})\right] dx + \int_{BC} -\left[H_{j+1/2}^{n-1/2} + (H_x)_{j+1/2}^{n-1/2}(x - x_{j+1/2})\right] dx + \\
 & \int_{CD} \left[F_{j+1/2}^{n-1/2} + (F_t)_{j+1/2}^{n-1/2}(t - t^{n-1/2})\right] dt + \int_{DF} \left[H_j^n + (H_x)_j^n(x - x_j)\right] dx + \\
 & \int_{FA} -\left[F_{j-1/2}^{n-1/2} + (F_t)_{j-1/2}^{n-1/2}(t - t^{n-1/2})\right] dt = 0
 \end{aligned} \tag{3.7}$$

Note that we are using a regular grid in the sense that the solution points³, (points on which the solution is saved), and the cell centroids are coincident. Also note that $|AB| = |BC| = \Delta x/2$ and $|CD| = |FA| = \Delta t/2$. Using these, we get

$$\begin{aligned}
 I = & -\frac{\Delta x}{2} \left[H_{j-1/2}^{n-1/2} - x_{j-1/2} (H_x)_{j-1/2}^{n-1/2} \right] - \frac{\Delta x}{2} \left[H_{j+1/2}^{n-1/2} - x_{j+1/2} (H_x)_{j+1/2}^{n-1/2} \right] \\
 & - \frac{\Delta x}{2} (H_x)_{j-1/2}^{n-1/2} x_c^{(AB)} - \frac{\Delta x}{2} (H_x)_{j+1/2}^{n-1/2} x_c^{(BC)} + \Delta x H_j^n + \Delta x (H_x)_j^n x_c^{(DF)} \\
 & - \Delta x (H_x)_j^n x_j + \frac{\Delta t}{2} \left\{ \left[F_{j+1/2}^{n-1/2} - F_{j-1/2}^{n-1/2} - t^{n-1/2} (F_t)_{j+1/2}^{n-1/2} + t^{n-1/2} (F_t)_{j-1/2}^{n-1/2} \right] \right. \\
 & \left. + t_c^{(CD)} \left[(F_t)_{j+1/2}^{n-1/2} - (F_t)_{j-1/2}^{n-1/2} \right] \right\} = 0
 \end{aligned} \tag{3.8}$$

Noting that $x_c^{(AB)} = x_{j-1/2} + \Delta x/4$, $x_c^{(BC)} = x_{j+1/2} - \Delta x/4$, $x_c^{(DF)} = x_j$, and $t_c^{(CD)} = t^{n-1/2} + \Delta t/4$,

the above equation becomes

$$\begin{aligned}
 I = & -\frac{\Delta x}{2} \left\{ H_{j-1/2}^{n-1/2} + H_{j+1/2}^{n-1/2} + \frac{\Delta x}{4} \left[(H_x)_{j-1/2}^{n-1/2} - (H_x)_{j+1/2}^{n-1/2} \right] \right\} + \Delta x H_j^n \\
 & + \frac{\Delta t}{2} \left\{ F_{j+1/2}^{n-1/2} - F_{j-1/2}^{n-1/2} + \frac{\Delta t}{4} \left[(F_t)_{j+1/2}^{n-1/2} - (F_t)_{j-1/2}^{n-1/2} \right] \right\} = 0
 \end{aligned} \tag{3.9}$$

rearrangement results in

² More details on the solution elements are available in Chapter 4, where the two-dimensional cases are studied.

³ More details about the solution points are available in Chapter 4, where the two-dimensional cases are studied.

$$H_j^n = \frac{1}{2} \left\{ H_{j-1/2}^{n-1/2} + H_{j+1/2}^{n-1/2} + \frac{\Delta x}{4} \left[(H_x)_{j-1/2}^{n-1/2} - (H_x)_{j+1/2}^{n-1/2} \right] \right\} \\ - \frac{\Delta t}{2\Delta x} \left\{ F_{j+1/2}^{n-1/2} - F_{j-1/2}^{n-1/2} + \frac{\Delta t}{4} \left[(F_t)_{j+1/2}^{n-1/2} - (F_t)_{j-1/2}^{n-1/2} \right] \right\} \quad (3.10)$$

The above equation contains derivatives that need to be calculated. In the CE/SE method, the derivatives are treated as independent variables that are solved for. Also note that, based on Eq. (3.3), calculation of the first-order derivative of F , (needed in Eq. (3.10)), involves calculation of the second-order mixed derivative of the temperature. The following two sections contain procedures to treat the derivatives.

3.1.1. First-Order Derivatives

The first-order derivatives, are calculated using the following weighted average formula

$$(\Psi_x)_j^n = (\Psi_x^+)_j^n W^+ + (\Psi_x^-)_j^n W^- \quad (3.11)$$

with

$$W^\pm = \frac{\left[(\Psi_x^\mp)_j^n \right]^{\tilde{a}}}{\left[(\Psi_x^-)_j^n \right]^{\tilde{a}} + \left[(\Psi_x^+)_j^n \right]^{\tilde{a}}} \quad (3.12)$$

and

$$\left(\Psi_x^-\right)_j^n = \frac{\Psi_j^n - \Psi_{j-1/2}^n}{\Delta x/2}, \quad \left(\Psi_x^+\right)_j^n = \frac{\Psi_{j+1/2}^n - \Psi_j^n}{\Delta x/2} \quad (3.13)$$

Note that, to avoid dividing by zero, in practice a small positive number such as 10^{-20} is added to the denominator in Eq. (3.12). The parameter Ψ , in the above relations, can be either H or T . The value of $\tilde{\alpha}$ is usually set equal to 1. As mentioned in [69], the above weighted average provides the necessary numerical damping. In other words, $\tilde{\alpha}$ can be regarded as an adjustable dissipation parameter. In Chapters 4 and 7, we will return to this parameter and study its effects in more detail; unless mentioned otherwise, its value is set to unity.

3.1.2. Second-Order Derivatives

The second-order derivatives, required for calculation of F_t are determined using a method explained below.

Using Taylor series to expanding $(T_x)_{j\pm 1/2}^{n-1/2}$ about the space-time solution point (j, n) , the following relation can be written.

$$(T_x)_{j\pm 1/2}^{n-1/2} - (T_x)_j^n = (x_{j\pm 1/2} - x_j)(T_{xx})_j^n - \frac{\Delta t}{2}(T_{xt})_j^n \quad (3.14)$$

which results in the following system

$$(T_x)_{j\pm 1/2}^{n-1/2} - (T_x)_j^n = \pm \frac{\Delta x}{2} (T_{xx})_j^n - \frac{\Delta t}{2} (T_{xt})_j^n \quad (3.15)$$

Adding the two equations in the above system leads to

$$(T_{xt})_j^n = \left[2(T_x)_j^n - (T_x)_{j-1/2}^{n-1/2} - (T_x)_{j+1/2}^{n-1/2} \right] / \Delta t \quad (3.16)$$

Therefore, the scheme is built by Eq. (3.10), with derivatives determined from Eqs. (3.11)-(3.16).

There exists also another method for treating the second-order derivatives by ignoring them on the solution elements [66]. Both methods were tried numerically. The first method results in slightly higher accuracies, (the truncation errors were used as a measure for the accuracy). The second method offers slightly faster convergence rates, and of course it goes through a smaller number of computations. Because the difference in the computational times between these two techniques is not significant, the more accurate scheme will be used, unless mentioned otherwise.

3.2 On the Equivalence of the CESE Formulation of the Enthalpy Method with the Conventional Formulation

In 1975, Shamsundar and Sparrow [88] provided a demonstration of the equivalence between the enthalpy method and the conventional form of the energy conservation

equation for the case of a substance with a discrete phase-change temperature. For this purpose, they applied the enthalpy form, first to a control volume, fixed in space, which did not contain the interface, and then to another control volume through which the interface passed. In the first case, because of the continuity of enthalpy and partial derivatives of the temperature, the Green's Theorem [89] can be applied to the integral form, thus, the conventional form readily results. In the second case, because of the discontinuity in the enthalpy, the conditions needed for validity of the Green's Theorem [89] are not satisfied. For this case, Shamsundar and Sparrow moved the interface in time and studied the limits of the conservation laws as the time increment vanished [88].

The space-time nature of the CE/SE method's conservation elements allows us to demonstrate that proof in a more straightforward manner. Since the time dimension materializes in the shape of the conservation element, the manual movement of the phase interface to a new time can be dispensed with. Note that, although the proof is provided here for a one-dimensional Cartesian problem, it can be extended without difficulty to higher dimensions.

Consider a one-dimensional heat conduction problem involving solid-liquid phase change, for a material that changes phase at a single fusion temperature, T_f . Identical and uniform densities are assumed for both phases while other physical properties can vary with phase and/or temperature. The classical formulation provides the following governing equations in the solid region, in the liquid region, and on the phase interface.

In the liquid region:

$$\rho c_L \frac{\partial T}{\partial t} + \frac{\partial F}{\partial x} = 0 \quad (3.17)$$

In the solid region:

$$\rho c_s \frac{\partial T}{\partial t} + \frac{\partial F}{\partial x} = 0 \quad (3.18)$$

On the phase interface:

$$T(X(t), t) = T_f \quad (3.19)$$

and

$$\rho L_f \frac{d X(t)}{d t} = F_L - F_s \quad (3.20)$$

where T denotes temperature, t is time, and L_f , ρ , c , and k are latent heat of fusion, density, specific heat, and conductivity of the material, respectively. $X(t)$ denotes the location of the phase interface at time t . Subscripts L and S refer to the solid and liquid phases and F is defined as

$$F = -k \frac{\partial T}{\partial x} \quad (3.21)$$

A differential space-time conservation element of the CE/SE method can be visualized as rectangle ABCD shown in Fig. 3.2.

Points A and B are at time t , while points C and D are the same spatial nodes at time $t + dt$. Considering (x, t) as coordinates of a two-dimensional Euclidean space-time, as mentioned in the previous section, the CE/SE formulation provides the following integral equations over the space-time conservation element.

$$\int_{S(ABCD)} \vec{\nabla} \bullet \vec{U} dA = 0 \quad (3.22)$$

and

$$\oint_{\Omega} \vec{U} \bullet \hat{n} d\mathbf{s} = 0 \quad (3.23)$$

where $S(ABCD)$ and Ω denote the surface and the boundary of the rectangle ABCD, respectively. Further, dA and $d\mathbf{s}$ denote surface and line elements on $S(ABCD)$ and Ω , respectively. The unit outward normal of the rectangle is referred to as \hat{n} and $\vec{U} = (F, H)$.

Enthalpy per unit volume, H , is defined as

$$H = \int_0^T \{ \mathbf{r} c dT + \mathbf{r} L_f \mathbf{d}(T - T_f) \} dT \quad (3.24)$$

where \mathbf{d} is the Dirac impulse function.

First consider the conservation element ABCD with no interface passing through it. Since ABCD is an arbitrary conservation element, readily it can be seen that Eq.(3.22) leads to the differential form of the governing equation. Since no interface exists, it also follows that the Greens's Theorem holds and Eq.(3.23) is equivalent to Eq.(3.22). Now consider the case where the phase interface falls in the conservation element ABCD. For example, as shown in Fig. 3.2, let the interface be located at point S_1 at time t , and at point S_2 at time $t + dt$. Without any loss in generality, it can be assumed that the portions of the rectangle ABCD that are to the left of the line segment S_1S_2 , are in the liquid phase while the right portion is solid. Equation (3.23) can then be written as

$$\int_{\Omega_s} \vec{U}_s \cdot \hat{n} d\mathbf{s} + \int_{\Omega_L} \vec{U}_L \cdot \hat{n} d\mathbf{s} = 0 \quad (3.25)$$

where Ω_s and Ω_L represent solid and liquid portions of Ω , respectively. On the other hand, Eq. (3.23) can also be applied to the liquid conservation element $AS_1^-S_2^-D$, as well as the solid conservation element $S_2^+S_1^+BC$, where plus and minus superscripts relate to the immediate liquid and solid neighborhoods of the points S_1 and S_2 , respectively.

$$\oint_{\Omega_L + \Sigma^-} \vec{U}_L \cdot \hat{n} d\mathbf{s} = 0 \quad (3.26)$$

and

$$\oint_{\Omega_s + \Sigma^+} \vec{U}_s \bullet \hat{n} d\mathbf{s} = 0 \quad (3.27)$$

where Σ^- and Σ^+ are the line segments $S_1^- S_2^-$ and $S_2^+ S_1^+$, respectively. Adding Eqs. (3.26) and (3.27) and subtracting Eq.(3.25) from the resultant relation, provides

$$\int_{\Sigma^-} \vec{U}_L \bullet \hat{n} d\mathbf{s} + \int_{\Sigma^+} \vec{U}_s \bullet \hat{n} d\mathbf{s} = 0 \quad (3.28)$$

Note that for the first integral in Eq. (3.28), $\hat{n} = \frac{dt}{ds} \hat{i} - \frac{dx}{ds} \hat{j}$ is the unit normal outward to the liquid region, while for the second integral $\hat{n} = -\frac{dt}{ds} \hat{i} + \frac{dx}{ds} \hat{j}$ is the unit normal outward to the solid region. Equation (3.28) then becomes

$$\int_{S_1 S_2} \{ (Fdt - Hdx)_L + (-Fdt + Hdx)_s \} = 0 \quad (3.29)$$

Since the line segment $S_1 S_2$ is an arbitrary part of the interface, the above equation implies the following condition, everywhere on the two sides of the interface.

$$[(Fdt - Hdx)_L + (-Fdt + Hdx)_s]_{S_1 S_2} = 0 \quad (3.30)$$

Equation (3.30), taking into account Eq. (3.24), gives the classical jump conditions at the interface, i.e.

$$\left[\frac{dx}{dt} \right]_{S_1 S_2} = \frac{F_L - F_S}{r L_f} \quad (3.31)$$

Note that since the slope of $S_1 S_2$ is in fact the speed at which the interface moves during time dt , Eq.(3.31) is equivalent to Eq. (3.20). The equivalence of Eq.(3.23) with Eq.(3.22), can then be verified as follows.

The Green's Theorem holds in the liquid conservation element $AS_1^- S_2^- D$, as well as in the solid conservation element $S_2^+ S_1^+ BC$. Therefore Eqs. (3.26) and (3.27) can be substituted by the following two equations respectively.

$$\int_{S(AS_1^- S_2^- D)} \vec{\nabla} \bullet \vec{U} dA = 0 \quad (3.32)$$

and

$$\int_{S(S_2^+ S_1^+ BC)} \vec{\nabla} \bullet \vec{U} dA = 0 \quad (3.33)$$

Adding the above two leads to Eq. (3.22).

Alternatively, Eq. (3.22) can also lead to the conventional form with the jump conditions. The proof would not be different from that provided in [33] for the weak solutions.

3.3 von Neumann Stability Analysis

The von Neumann analysis [90], is mainly employed for stability analysis and can provide a necessary stability criterion for a linear scheme. Of course the analysis can not be applied to an actual phase change problem because of the geometric nonlinearity involved. However, application of the analysis to a simplified case of a heat conduction problem, non-dimensionalized using the Stefan number in its time scale, can reveal a great deal about the stability and dissipative/dispersive behavior of the numerical scheme.

Consider the heat conduction equation, Eq. (2.1), in one spatial dimension. A non-dimensional form, adopted from [27], uses the following non-dimensional parameters

$$t^* = S_t \frac{\mathbf{a} t}{L^2}, T^* = \frac{T - T_f}{T_{ref.} - T_f}, \text{ and } x^* = \frac{x}{L} \quad (3.34)$$

where \mathbf{a} denotes the diffusivity, L is an appropriate length scale, T_f represents the fusion temperature of the material, and $T_{ref.}$ is a reference temperature. The Stefan number S_t is defined as

$$S_t = \frac{c(T_{ref.} - T_f)}{L_f} \quad (3.35)$$

The non-dimensional equation, then becomes

$$\frac{\partial T^*}{\partial t^*} = \frac{1}{S_t} \frac{\partial^2 T^*}{\partial x^{*2}} \quad (3.36)$$

Application of the CE/SE scheme to Eq.(3.36) results in an equation analogous to Eq.(3.10). Dropping the * superscripts, the scheme to be analyzed, becomes

$$\begin{aligned} T_j^n = & \frac{1}{2} (T_{j-1/2}^{n-1/2} + T_{j+1/2}^{n-1/2}) + \\ & \left(\frac{\Delta x}{8} - \frac{\Delta t}{2 \Delta x S_t} \right) [(T_x)_{j-1/2}^{n-1/2} - (T_x)_{j+1/2}^{n-1/2}] + \\ & \frac{(\Delta t)^2}{8 \Delta x S_t} [(T_{xt})_{j+1/2}^{n-1/2} - (T_{xt})_{j-1/2}^{n-1/2}] \end{aligned} \quad (3.37)$$

with the first-order derivatives from Eqs.(3.11)-(3.13).

The second-order derivatives can be determined using each of the two methods mentioned in Section 3.1.2. In particular, selection of the second (less complicated) method of Section 3.1.2, leads to a scheme involving only two time levels, i.e., time level n and time level $n - 1/2$. Usage of Eq. (3.16), on the other hand, results in a scheme involving

three time levels, i.e., time levels n , $n - 1/2$, and $n - 1$. Both methods are applied and studied in the following sections.

Further, selection of different values for $\tilde{\mathbf{a}}$ in Eq. (3.12), can lead to different schemes. In particular, $\tilde{\mathbf{a}}=0$ leads to linear schemes, while non-zero values for $\tilde{\mathbf{a}}$ cause non-linearity in determination of the first-order derivatives. Both situations are studied in the following sections.

3.2.1 Linear Scheme without Second-Order Derivatives

Among the variations mentioned in the previous section, the simplest one is a linear scheme without second-order derivatives. In order to generate this scheme, set the second-order derivatives, in Eq. (3.37) equal to zero. Further, substitute for the first-order derivatives from Eqs. (3.11)-(3.13), using $\tilde{\mathbf{a}}=0$. The scheme becomes

$$T_j^n = \frac{1}{2} (T_{j-1/2}^{n-1/2} + T_{j+1/2}^{n-1/2}) + \left(\frac{1}{8} - \frac{\Delta t}{2 (\Delta x)^2 S_t} \right) (2T_j^{n-1/2} - T_{j-1}^{n-1/2} - T_{j+1}^{n-1/2}) \quad (3.38)$$

The von Neumann analysis can then be applied to the above equation by substituting $T_j^n = A^n e^{i j q}$, where A is the disturbance amplitude, $i = \sqrt{-1}$, and q is the wave number multiplied by Δx . After algebraic manipulations, the amplification factor, G , is found as follows

$$\begin{aligned}
G &= \frac{A^n}{A^{n-1/2}} \\
&= \frac{1}{2} \left(e^{-iq/2} + e^{iq/2} \right) + \left(\frac{1}{8} - \frac{\Delta t}{2 (\Delta x)^2 S_t} \right) (2 - e^{-iq} - e^{iq})
\end{aligned} \tag{3.39}$$

Now using $e^{imq} = \cos(mq) + i \sin(mq)$ in the above equation we get

$$G = \cos \frac{q}{2} + \mathbf{s} \left(1 - \cos^2 \frac{q}{2} \right) \tag{3.40}$$

where

$$\mathbf{s} \equiv \frac{1}{2} - \frac{2 \Delta t}{(\Delta x)^2 S_t} \tag{3.41}$$

Two conclusions may be drawn from Eq. (3.42): one regarding the necessary stability condition and the other regarding the method's dissipation and dispersion. The former is found by requiring $|G| \leq 1$, or

$$-1 \leq G \leq 1 \tag{3.42}$$

This inequality can be studied in two parts:

a) $G \leq 1$. Using Eq. (3.40), we get

$$\cos \frac{\mathbf{q}}{2} + \mathbf{s} \left(1 - \cos^2 \frac{\mathbf{q}}{2} \right) \leq 1 \quad (3.43)$$

or

$$-1 + \cos \frac{\mathbf{q}}{2} + \mathbf{s} \left(1 - \cos \frac{\mathbf{q}}{2} \right) \left(1 + \cos \frac{\mathbf{q}}{2} \right) \leq 0 \quad (3.44)$$

or

$$\left(1 - \cos \frac{\mathbf{q}}{2} \right) \left[-1 + \mathbf{s} \left(1 + \cos \frac{\mathbf{q}}{2} \right) \right] \leq 0 \quad (3.45)$$

Since $1 - \cos \frac{\mathbf{q}}{2} \geq 0$, for the above inequality to hold, we need

$$-1 + \mathbf{s} \left(1 + \cos \frac{\mathbf{q}}{2} \right) \leq 0 \quad (3.46)$$

or

$$\mathbf{s} \left(1 + \cos \frac{\mathbf{q}}{2} \right) \leq 1 \quad (3.47)$$

But, since

$$0 \leq 1 + \cos \frac{\mathbf{q}}{2} \leq 2 \quad (3.48)$$

for inequality (3.47) to hold we need

$$\mathbf{s} \leq \frac{1}{2} \quad (3.49)$$

Considering Eq. (3.41), and the fact that the S_r number is defined to be positive, it follows that inequality (3.49) always holds. Therefore, part (a) does not lead to any stability restriction.

b) $G \geq -1$. Using Eq. (3.40), we get

$$\cos \frac{\mathbf{q}}{2} + \mathbf{s} \left(1 - \cos^2 \frac{\mathbf{q}}{2} \right) \geq -1 \quad (3.50)$$

or

$$\left(1 + \cos \frac{\mathbf{q}}{2} \right) \left[1 + \mathbf{s} \left(1 - \cos \frac{\mathbf{q}}{2} \right) \right] \geq 0 \quad (3.51)$$

Since, $1 + \cos \frac{\mathbf{q}}{2} \geq 0$, for the above inequality to hold, we need

$$1 + \mathbf{s} \left(1 - \cos \frac{\mathbf{q}}{2} \right) \geq 0 \quad (3.52)$$

or

$$\mathbf{s} \left(\cos \frac{\mathbf{q}}{2} - 1 \right) \leq 1 \quad (3.53)$$

To study the above inequality, consider the following two cases:

i) $\mathbf{s} \geq 0$. Since, $\cos \frac{\mathbf{q}}{2} - 1 \leq 0$, for this case inequality (3.53) holds and therefore it does not

lead to stability restriction.

ii) $\mathbf{s} < 0$. Since

$$-2 \leq \cos \frac{\mathbf{q}}{2} - 1 \leq 0 \quad (3.54)$$

the worst case for (3.53) would be when $\cos \frac{\mathbf{q}}{2} - 1 = -2$, which leads to

$$-2 \mathbf{s} \leq 1$$

or

$$\mathbf{s} \geq \frac{-1}{2} \quad (3.55)$$

or, using Eq. (3.41),

$$\frac{\Delta t}{(\Delta x)^2 S_t} \leq \frac{1}{2} \quad (3.56)$$

Inequality (3.55), can be obtained, alternatively, as follows⁴

⁴ This procedure was provided by Dr. Sin-Chung Chang in his review comments.

Consider inequality (3.53). If $\cos \frac{q}{2} - 1 = 0$, (3.53) holds for all s . Now consider all cases

where

$$\cos \frac{q}{2} - 1 \neq 0 \quad (3.57)$$

Inequality (3.54), then becomes

$$-2 \leq \cos \frac{q}{2} - 1 < 0 \quad (3.58)$$

Using (3.57) and (3.58), inequality (3.53) can be written as

$$s \geq \frac{1}{\cos \frac{q}{2} - 1} \quad (3.59)$$

Further, (3.58) yields

$$-\frac{1}{2} \geq \frac{1}{\cos \frac{q}{2} - 1} \quad (3.60)$$

Considering (3.59) and (3.60), one concludes that inequality (3.55), (and therefore, (3.56)), is the stability restriction.

Figures 3.3-3.5 demonstrate plots of the amplification factor G , (see Eq. (3.40)), versus the Stefan number. These figures contain a graphic representation of the stability criterion in Eq. (3.56). Figures 3.3-3.5 are generated for $\Delta x = 0.05$ and different time-steps. For example, Fig. 3.3 shows that, for $\Delta t = 10^{-3}$, reduction of the Stefan number to values smaller than $S_t^* \cong 0.77$, leads to unstable results. This minimum Stable Stefan number, (S_t^*) , reduces to 0.08 for $\Delta t = 10^{-4}$, as seen in Fig. 3.4. Therefore, derivation of Eq. (3.56) is graphically confirmed. By reducing the time-step to $\Delta t = 10^{-6}$, as shown in Fig. 3.5, even for $S_t = 0.01$, which is the smallest Stefan number used in generating this figure, the stability criterion still holds.

Numerical experiments were also performed in order to confirm the above analysis. Considering (3.56), it is seen that the numerical examination should be done in two steps: 1) study of the effect of the Stefan number on the stability while the spatial increment is fixed, and 2) study of the effect of the spatial grid spacing on the stability while the Stefan number is fixed. The results of these numerical experiments are presented in Tables 3.1 and 3.2.

Stefan number	Δt (edge of stability)	$\frac{\Delta t}{(\Delta x)^2 S_t}$ (edge of stability)
0.01	5.04×10^{-5}	0.5040
0.1	5.04×10^{-4}	0.5040
1	5.04×10^{-3}	0.5040
10	5.04×10^{-2}	0.5040

Table 3.1: Numerical experiments of stability: effect of the Stefan number

Δx	Δt (edge of stability)	$\frac{\Delta t}{(\Delta x)^2 S_t}$ (edge of stability)
$\frac{1}{10}$	5.04×10^{-2}	0.5040
$\frac{1}{20}$	1.25×10^{-2}	0.5000
$\frac{1}{30}$	5.55×10^{-3}	0.4995
$\frac{1}{40}$	3.125×10^{-3}	0.5000

Table 3.2: Numerical experiments of stability: effect of the spatial increment

Table 3.1 presents the time-step, at the edge of stability, for a spatial increment $\Delta x = 0.1$, for different Stefan numbers. These results show that, for a specified spatial increment, smaller time-steps are needed for stability, as the Stefan number is reduced. Further, the stability criterion of (3.56) is also confirmed, on a fixed spatial grid.

Table 3.2, on the other hand, is generated for cases with $S_t = 10$, but on different spatial grids. Using these cases, the dependence of the time-step at the edge of stability, on the spatial grid spacing, is examined. Results confirm that, (3.56) holds, for a fixed Stefan number. Combining results of Tables 3.1 and 3.2, the stability criterion of (3.56) is confirmed.

It is worthwhile to note that, the above condition may not be sufficient for the stability of the original phase change scheme, or even the heat conduction equation in higher dimensions. It can, however, be used as a starting point. It also shows that by reducing the

Stefan number, while using the same spatial increments, stability may require smaller time increments.

The amplification factor in Eq. (3.40), also reveals insight regarding the dissipative/dispersive behavior of the scheme. In Chapter 7, we return to this analysis and use it to study dissipative/dispersive behavior of the numerical method.

3.2.2 Linear Scheme with Second-Order Derivatives

The equation for this scheme can be generated by substituting for the second-order derivatives in Eq. (3.37), from Eq. (3.16). The first-order derivatives are treated similar to Section 3.2.1. The scheme becomes

$$\begin{aligned}
 T_j^n = & \frac{1}{2} (T_{j-1/2}^{n-1/2} + T_{j+1/2}^{n-1/2}) + \\
 & \left(\frac{1}{8} - \frac{3\Delta t}{4(\Delta x)^2 S_t} \right) (2T_j^{n-1/2} - T_{j-1}^{n-1/2} - T_{j+1}^{n-1/2}) + \\
 & \frac{\Delta t}{8(\Delta x)^2 S_t} (T_{j-1/2}^{n-1} + T_{j+1/2}^{n-1} - T_{j-3/2}^{n-1} + T_{j+3/2}^{n-1})
 \end{aligned} \tag{3.61}$$

As can be seen, three time levels are involved in Eq. (3.61). Similar to Section 3.2.1, the von Neumann analysis can be applied to Eq. (3.61) to produce

$$\begin{aligned}
 \frac{A^n}{A^{n-1/2}} = & \cos \frac{\mathbf{q}}{2} + \bar{S} (1 - \cos \mathbf{q}) + \\
 & \frac{\Delta t}{4(\Delta x)^2 S_t} \frac{A^{n-1}}{A^{n-1/2}} \left(\cos \frac{\mathbf{q}}{2} - \cos \frac{3\mathbf{q}}{2} \right)
 \end{aligned} \tag{3.62}$$

where

$$\bar{S} \equiv \frac{1}{4} - \frac{3\Delta t}{2(\Delta x)^2 S_t} \quad (3.63)$$

Assuming $G \equiv \frac{A^n}{A^{n-1/2}} \cong \frac{A^{n-1/2}}{A^{n-1}}$, Eq. (3.62) can be written as the following quadratic equation.

$$G^2 - \left[\cos \frac{\mathbf{q}}{2} + \bar{S} (1 - \cos \mathbf{q}) \right] G - \frac{\Delta t}{4(\Delta x)^2 S_t} \left(\cos \frac{\mathbf{q}}{2} - \cos \frac{3\mathbf{q}}{2} \right) = 0 \quad (3.64)$$

Solving Eq. (3.64) produces

$$G = \frac{1}{2} \left\{ \cos \frac{\mathbf{q}}{2} + \bar{S} (1 - \cos \mathbf{q}) \pm \sqrt{\left[\cos \frac{\mathbf{q}}{2} + \bar{S} (1 - \cos \mathbf{q}) \right]^2 + \frac{\Delta t}{(\Delta x)^2 S_t} \left(\cos \frac{\mathbf{q}}{2} - \cos \frac{3\mathbf{q}}{2} \right)} \right\} \quad (3.65)$$

The above amplification factor, although too complicated for analytical stability analysis, can be studied numerically. Figures 3.6-3.8 contain plots of the amplification factor of Eq. (3.56), versus the Stefan number, using the negative sign. Usage of the positive sign shows a scheme that is stable even for relatively large time-steps. This behavior is inconsistent with the numerical experiments. The positive sign was, therefore, discarded. All figures are generated using $\Delta x = 0.05$. A pattern similar to Figs. 3.3-3.5 is also seen in Figs. 3.6-3.8.

Again, in Figs. 3.6 and 3.8, the value of S_t^* leads to a stability criterion as follows. In Fig. 3.6, the stability is confirmed for Stefan numbers larger than 0.86. In other words the stability criterion can be determined as $\frac{\Delta t}{(\Delta x)^2 S_t} \leq \frac{10^{-3}}{(0.05)^2 \times 0.86} \cong 0.465$. A similar calculation, for Fig. 3.7, provides $\frac{\Delta t}{(\Delta x)^2 S_t} \leq \frac{5 \times 10^{-4}}{(0.05)^2 \times 0.43} \cong 0.465$. Finally, the time-step is reduced to 1.1×10^{-5} in Fig. 3.8. For this case the stability criterion holds, even for the smallest Stefan number present in the figure, that is $S_t = 0.01$. These figures also contain information about the dissipative / dispersive behavior of the scheme as discussed in Chapter 7.

Numerical experiments were also performed for this scheme. Again, it was seen that reducing of the Stefan number, has a destabilizing effect. The results were similar to Tables 3.1 and 3.2, except for the value of $\frac{\Delta t}{(\Delta x)^2 S_t}$ at the edge of stability. In fact, the numerical experiments determined the stability criterion for this scheme to be

$$\frac{\Delta t}{(\Delta x)^2 S_t} \leq 0.4667 \quad (3.66)$$

Therefore, addition of the second-order derivatives to the scheme has, as expected, a destabilizing effect.

Further, the values 0.4667 agrees with the value graphically extracted from Figs. 3.6-3.8, based on the analytical amplification factor of Eq. (3.56).

3.2.3 Non-Linear Scheme without Second-Order Derivatives

In order to generate this scheme, set the second-order derivatives, in Eq. (3.37) equal to zero. Further, substitute for the first-order derivatives from Eqs. (3.11)-(3.13), using $\tilde{\alpha}=1$.

After substitutions, the scheme becomes

$$T_j^n = \frac{1}{2} (T_{j-1/2}^{n-1/2} + T_{j+1/2}^{n-1/2}) + \left(\frac{1}{4} - \frac{\Delta t}{(\Delta x)^2 S_t} \right) \times \left[\frac{(T_{j-1/2}^{n-1/2} - T_{j-1}^{n-1/2})^{\tilde{\alpha}} (T_j^{n-1/2} - T_{j-1/2}^{n-1/2}) + (T_j^{n-1/2} - T_{j-1/2}^{n-1/2})^{\tilde{\alpha}} (T_{j-1/2}^{n-1/2} - T_{j-1}^{n-1/2})}{(T_{j-1/2}^{n-1/2} - T_{j-1}^{n-1/2})^{\tilde{\alpha}} + (T_j^{n-1/2} - T_{j-1/2}^{n-1/2})^{\tilde{\alpha}}} - \frac{(T_{j+1/2}^{n-1/2} - T_j^{n-1/2})^{\tilde{\alpha}} (T_{j+1}^{n-1/2} - T_{j+1/2}^{n-1/2}) + (T_{j+1}^{n-1/2} - T_{j+1/2}^{n-1/2})^{\tilde{\alpha}} (T_{j+1/2}^{n-1/2} - T_j^{n-1/2})}{(T_{j+1/2}^{n-1/2} - T_j^{n-1/2})^{\tilde{\alpha}} + (T_{j+1}^{n-1/2} - T_{j+1/2}^{n-1/2})^{\tilde{\alpha}}} \right] \quad (3.67)$$

and using $\tilde{\alpha}=1$

$$T_j^n = \frac{1}{2} (T_{j-1/2}^{n-1/2} + T_{j+1/2}^{n-1/2}) + \left(\frac{1}{4} - \frac{\Delta t}{(\Delta x)^2 S_t} \right) \times \left[\frac{2(T_{j-1/2}^{n-1/2} - T_{j-1}^{n-1/2})(T_j^{n-1/2} - T_{j-1/2}^{n-1/2})}{-T_{j-1}^{n-1/2} + T_j^{n-1/2}} - \frac{2(T_{j+1/2}^{n-1/2} - T_j^{n-1/2})(T_{j+1}^{n-1/2} - T_{j+1/2}^{n-1/2})}{-T_j^{n-1/2} + T_{j+1}^{n-1/2}} \right] \quad (3.68)$$

As can be seen, the above equation is non-linear and, therefore, the von-Neumann analysis is inapplicable. Numerical experiments need be used for stability analysis. These experiments result in a stability criterion similar to the linear scheme without second-order derivatives, see Section 3.3.1.

The difference between this scheme and the corresponding linear scheme, explained in Section 3.3.1, is seen for time-steps larger than that required for stability. In the linear scheme, time-steps slightly above the edge of stability, cause unbounded rapid growth in the errors. In the non-linear scheme, there is a zone of time-steps, above the edge of stability, that result in non-vanishing, but bounded, errors. This comparison shows that the non-linear scheme has higher dissipation compared to the linear scheme, whereas the linear scheme has more dispersion.

3.2.4 Non-Linear Scheme with Second-Order Derivatives

Finally, this is the actual scheme used throughout this thesis. Similar to the previous section, the non-linearity inherent in this scheme makes the von-Neumann stability analysis inapplicable. Numerical experiments confirm that (3.66) is still valid as the stability criterion for this scheme.

Similar to the previous section, the difference between this scheme and the corresponding linear scheme, explained in Section 3.3.2, is seen for time-steps larger than that required for stability. In the linear scheme, for example, $\frac{\Delta t}{(\Delta x)^2 S_i} > 0.4668$ leads to unbounded rapid growth of the errors. In the non-linear scheme, on the other hand, for

$0.4668 \leq \frac{\Delta t}{(\Delta x)^2 S_t} \leq 0.6550$ the errors remain bounded and the rapid unbounded error

growth does not start until $\frac{\Delta t}{(\Delta x)^2 S_t} > 0.6550$. This comparison, again, shows that the

non-linear scheme has higher dissipation compared to the linear scheme, whereas the linear scheme has more dispersion.

3.4 Validation tests

To assess the accuracy and effectiveness of the CE/SE method applied to conduction problems with phase change, several classical cases were studied. The results were compared to analytical solutions and the method was found to be accurate, robust and efficient. Details of the validation tests, as well as numerical study of the convergence and error behavior follows.

3.4.1 Steady Linear Case

To validate the program, it is good to start from a very simple problem. For our case, that would be a linear steady state conduction problem without phase change, i.e.,

$$H = T \text{ and } T = x \quad (3.69)$$

Obviously, this distribution satisfies the governing equation (Eq. (3.1)). Using Eq. (3.3) for unit conductivity, the following flux functions are obtained

$$F = -T_x = -1, F_x = -T_{xx} = 0, \text{ and } F_t = -T_{xt} = 0 \quad (3.70)$$

The correct distribution mentioned above was applied to the boundaries and a uniform error distribution was used as initial conditions. For this steady state case, CE/SE method is exact, in the sense that no truncation error exists. This can be shown analytically as follows: Using Eqs. (3.69) and (3.70) in Eq. (3.10), we get

$$H_j^n = \frac{1}{2} \left\{ x_{j-1/2} + x_{j+1/2} + \frac{\Delta x}{4} [1-1] \right\} - \frac{\Delta t}{2\Delta x} \left\{ -1 - (-1) + \frac{\Delta t}{4} [0-0] \right\} = x_j$$

Using this in Eq. (3.11), then yields

$$(H_x)_j^n = 1$$

Similarly

$$(T_x)_j^n = 1$$

and using Eq. (3.16)

$$(T_{xt})_j^n = [2 - 1 - 1] / \Delta t = 0$$

Therefore, if Eqs. (3.69) and (3.70) are applied to the boundaries of a line segment of unit length and an error distribution over the entire domain is used as initial condition, for a suitable time step (i.e. one that leads to stability), the code should be able to proceed and finally produce the correct distribution everywhere in the field. This was observed in

practice. This simple problem can be a great help in the study of time step effects on stability and convergence rate. One can also use this case for selecting the optimum time step for a particular spatial grid. For this purpose, different time-steps are used on a fixed spatial grid, and the evolution of the errors associated with each case is studied. Error is defined as the infinity norm of the absolute value of the difference between numerical and exact values of T , over the entire domain. Numerical experiments reveal the existence of three time-step zones:

- 1) Large time steps leading to enlarging errors,
- 2) Medium time steps leading to non-vanishing but bounded errors for which the upper error bound reduces with reducing time step,
- 3) Small enough time steps that lead to stable, time step independent results, with errors vanishing to the order of machine zero.

Zone 3, in itself, is divided into two sub-zones:

- a) Larger time-steps, for which the convergence rate decreases by enlarging the time-step,
- b) Smaller time-steps, for which the convergence rate increases by enlarging the time-step.

The above two sub-zones are separated by the optimum time-step, which results in the fastest convergence rate. Figures 3.9 and 3.10 provide an illustration for the one-dimensional case's zone 3.

Figure 3.9 shows the reduction of the errors to the order of machine zero. Figure 3.10, provides an illustration of the optimum time-step for two different spatial grid increments.

Further conclusions drawn from this figure are:

- The magnitude of the optimum time-step decreases by refining the spatial grid. This was to be expected because of the stability criterion.
- The rate of convergence decreases by refining the grid. This fact is common among the numerical methods.

More details on the effects of spatial grid increments, time-dependent boundary conditions and numerical investigation of the order of accuracy of the method are discussed in the following chapters.

3.4.2 Single-Phase Stefan Problem

In order to assess the accuracy of the one-dimensional phase change scheme, a single-phase Stefan problem is used as a benchmark, under the following conditions.

Consider a slab of thickness $L = 1$ with the initial state assumed to be liquid at the fusion temperature T_f . At $t = 0$, the temperature of the surface at $x = 0$ drops to T_w and is maintained at that value. The surface at $x = L$ is effectively insulated. The analytical solution of this problem, containing the transient temperature distributions and the phase front location, can be found in [69]⁵. This problem is studied numerically for a Stefan numbers of 3. The case is modeled using a uniform spatial grid containing 1,100 nodes.

⁵ For more details about this benchmark problem see Chapter 4.

Other parameters are $T_w = -1.0^\circ C$, $T_f = 0.0^\circ C$, while the thermal diffusivity and specific heats are set equal to unity.

Figure 3.11 demonstrates the temperature distribution at $t = 0.14$ s for the above problem. As can be seen, excellent agreement is achieved in comparison to the exact solution. The same observation can be made from Fig. 3.12. This plot represents the corresponding enthalpy curve. Here it is seen that the sharp jump in the enthalpy, at the phase front, is perfectly resolved. Similar results are obtained for other Stefan numbers.

3.4.3 One-Dimensional Solidification of the Binary Al-4.5% Cu Alloy

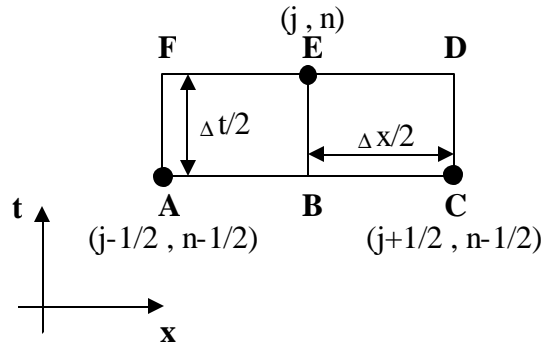
The physical situation considered thus far has involved isothermal phase change. To solve problems involving phase change over a temperature range, (see Section 2.5), the computer program was then extended. The benchmark problem used here is similar to the one explained in the previous section, except that in this case a mushy zone exists. Properties of the material, the relationship between the temperature and the liquid fraction in the mushy zone, as well as a semi-analytical solution (using a heat balance approach), are adopted from [86]. The problem involves solidification of the Binary Al-4.5% Cu Alloy. The function $\tilde{F}(T)$ (see Equation (2.7)), for this material is given as

$$\tilde{F}(T) = \left(\frac{T_F - T}{T_F - T_{L_f}} \right)^{-b}, T_{S_f} \leq T \leq T_{L_f} \quad (3.71)$$

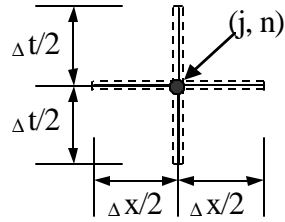
where $b = 1.163$, $T_{L_f} = 919$ K, $T_{S_f} = 821$ K, and $T_F = 933$ K is the freezing point of the solvent. Examination of Eq. (3.71) reveals a temperature range associated with a non-linear $\tilde{F}(T)$ accompanied by a step discontinuity (an isothermal phase change) at the eutectic temperature, T_{S_f} [86]. Other properties of the material are listed in Table 3.3. Initially, the material is assumed to be at T_{L_f} . A Dirichlet boundary condition of $T = 573$ K is imposed at $x = 0$, at time $t = 0$. The geometry is assumed to be a line segment of length 0.2 m. The spatial grid is uniform and contains 200 nodes. Figure 3.13 shows the results obtained using the one-dimensional extended scheme, compared to the semi-analytical solution from [86]. Figure 3.14 is a plot of the liquid fraction versus temperature for this problem. This case confirms the space-time CE/SE method's potential as an effective alternative numerical scheme for a general phase change problem.

Property	Value	Property	Value
c_s	900 J/kg.K	c_L	1100 J/kg.K
k_s	200 W/m.K	k_L	90 W/m.K
r	2800 kg/m^3	L_f	$3.9 \times 10^5 \text{ J/kg}$

Table 3.3: Properties of a binary Al-4.5% Cu alloy from [86]



(a)



(b)

Figure 3.1: Computational molecule of the CE/SE method, (a) CE (j, n) and (b) SE (j, n)

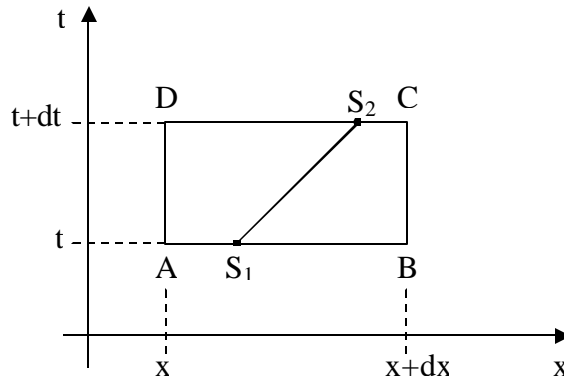


Figure 3.2: Space-time conservation element containing the phase interface

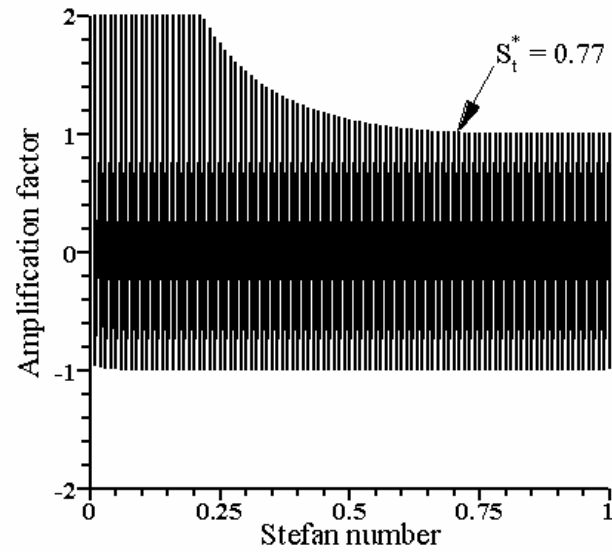


Figure 3.3: The amplification factor for time step equal to 1.E-3, for the linear scheme without the second-order derivatives

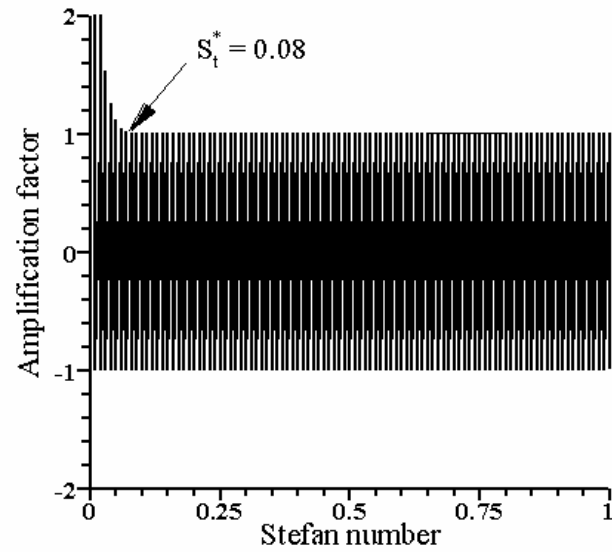


Figure 3.4: The amplification factor for time step equal to 1.E-4, for the linear scheme without the second-order derivatives

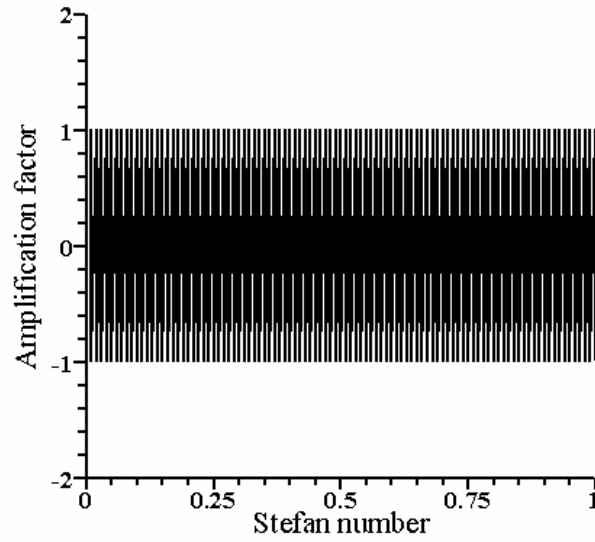


Figure 3.5: The amplification factor for time step equal to 1.E-6, for the linear scheme without the second-order derivatives

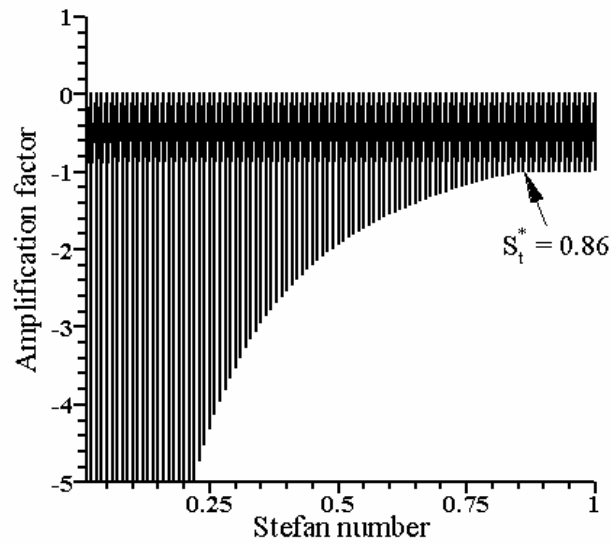


Figure 3.6: The amplification factor for time step equal to 1.E-3, for the linear scheme with the second-order derivatives

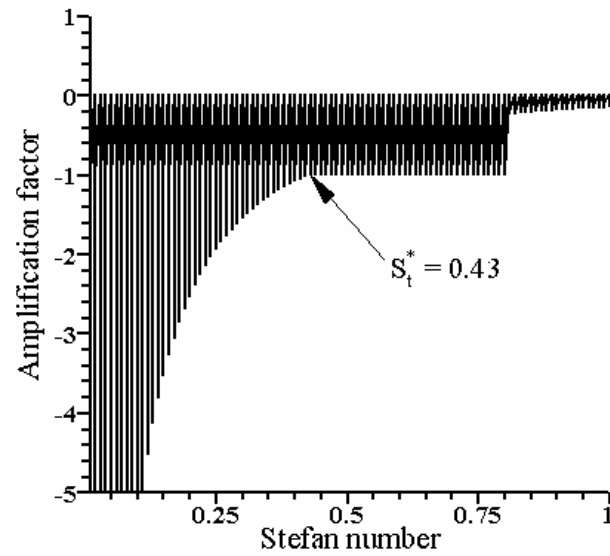


Figure 3.7: The amplification factor for time step equal to 5.E-4, for the linear scheme with the second-order derivatives

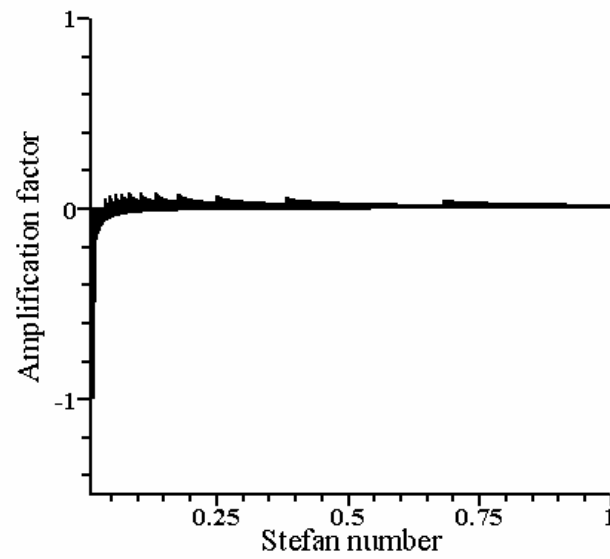


Figure 3.8: The amplification factor for time step equal to 1.1E-5, for the linear scheme with the second-order derivatives

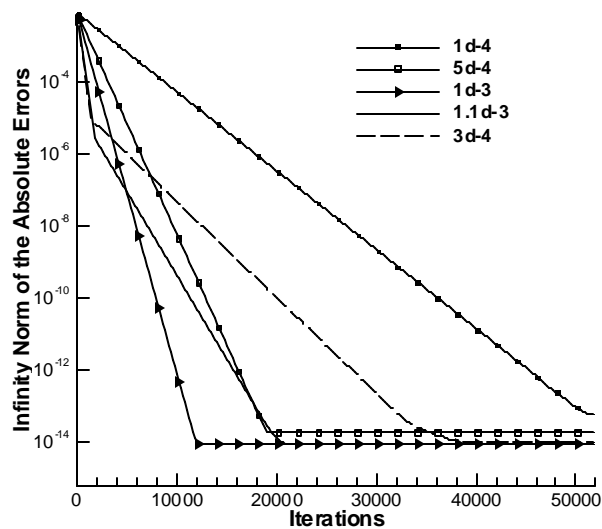


Figure 3.9: Time step zone 3 for one-dimensional code; vanishing errors for different time-steps

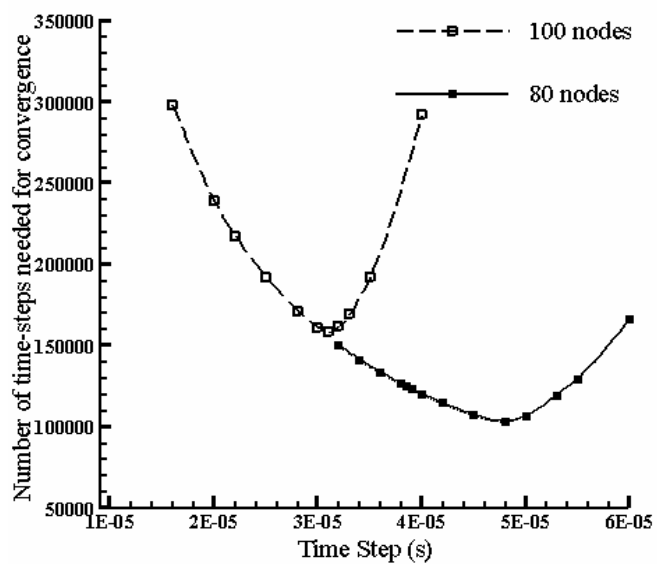
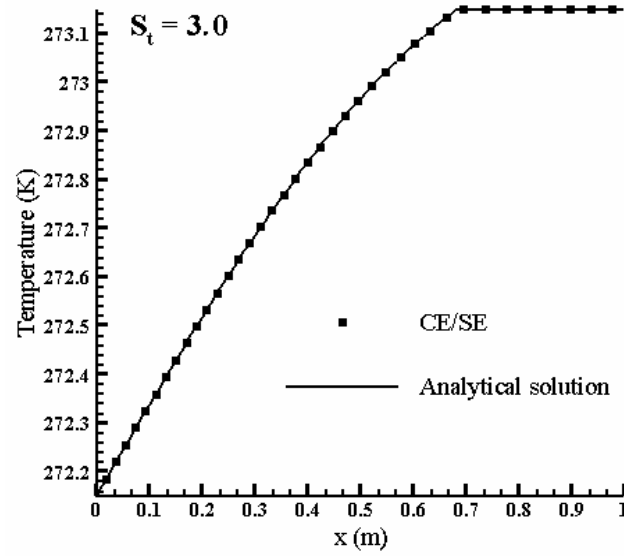
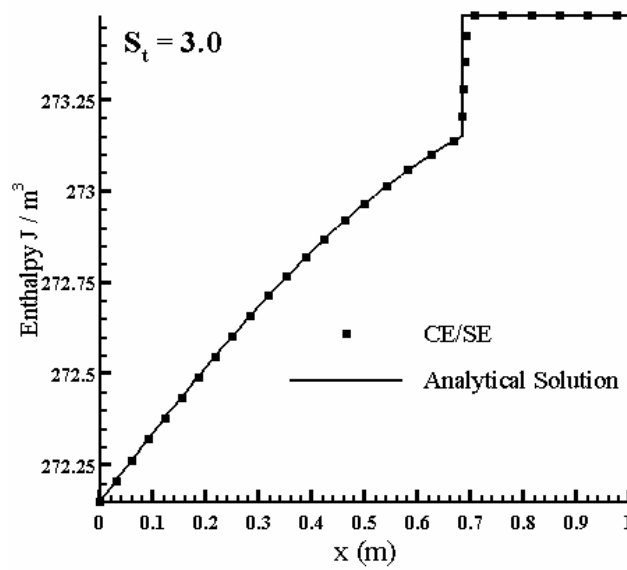


Figure 3.10: Optimum time-step

Figure 3.11: Temperature profile at $t = 0.14$ sFigure 3.12: Enthalpy distribution at $t = 0.14$ s

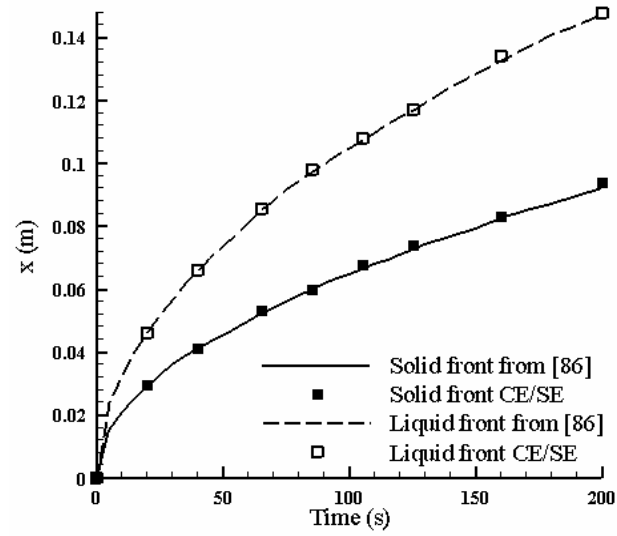


Figure 3.13: Solidification of the binary Al-4.5% Cu alloy from [86]

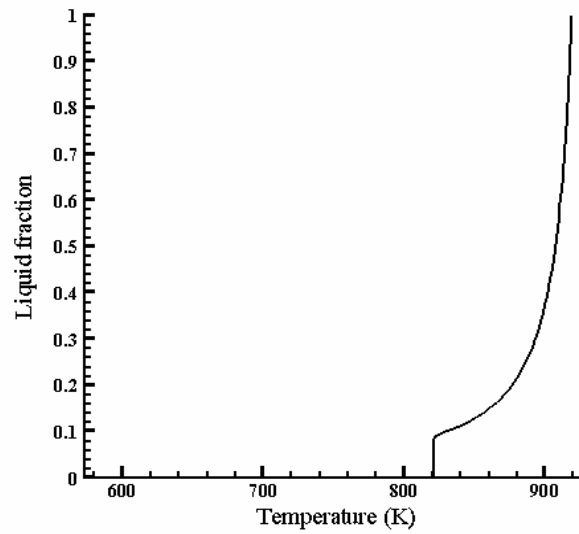


Figure 3.14: The liquid fraction function

Chapter 4

TWO-DIMENSIONAL CE/SE PHASE-CHANGE SCHEME

Many aspects of the behavior of a numerical scheme can be studied using its one-dimensional version. However, because of the geometric simplicity of such cases, many features may as well remain unrevealed. Further, features such as the one-dimensional stability condition, although useful as an initial guess, may not be readily extendable to higher dimensions. Finally, in order to make the phase change solver as general as possible, development of a two-dimensional version is essential.

In this chapter, the two-dimensional CE/SE phase change scheme is derived. Its error behavior, convergence properties, and order of accuracy are studied numerically. The computer program developed from this methodology is then validated using several phase change benchmark problems. It is found to be accurate. Further, temperature profiles and interface locations are resolved without non-physical oscillations. The behavior of the scheme is also studied at the problematic limit of small Stefan numbers.

4.1 Development of a Two-Dimensional Space-Time CE/SE Scheme for Heat Conduction with Melting/ Freezing

The governing equation (Eq.(2.3)), for two spatial dimensions, is written as

$$\frac{\partial H}{\partial t} = \frac{\partial}{\partial x} \left(k \frac{\partial T}{\partial x} \right) + \frac{\partial}{\partial y} \left(k \frac{\partial T}{\partial y} \right) \quad (4.1)$$

Equation (2.6) can be used without change. Define vector \vec{U} as

$$\vec{U} = (F, G, H) \quad (4.2)$$

where H is enthalpy per unit volume and

$$F = -k \frac{\partial T}{\partial x}, \quad G = -k \frac{\partial T}{\partial y} \quad (4.3)$$

are referred to as the flux functions. Considering (x, y, t) as the coordinates of a three-dimensional Euclidean space-time, the computational grid that is used here can be explained as follows. The spatial projection of the grid is a two-dimensional, unstructured mesh which consists of Delaunay triangulation [91] on the xy -plane that, considering the time axis as the third dimension, makes prisms perpendicular to the xy -plane. The computational molecule of this grid is shown in Fig. 4.1(a), where nodes V_1 , V_2 , and V_3 are

the vertices of a triangular cell j at time level $n - 1/2$, with C as its centroid, while points C_1 , C_2 , and C_3 denote the centroids of three neighboring cells j_1 , j_2 , and j_3 , respectively. The neighbors are named in a way that any vertex V_k , $k = 1, 2$, and 3 , of cell j faces the side shared by cell j and its neighbor j_k . Primed points represent the same spatial nodes one-half time-step later. For each cell, the integral form of the governing equation may be applied to the octahedral element that is the union of three tetragonal prisms: $C V_2 C_1 V_3 V'_3 C' V'_2 C'_1$, $C V_3 C_2 V_1 V'_1 C' V'_3 C'_2$, and $C V_1 C_3 V_2 V'_2 C' V'_1 C'_3$. The octahedron will be called the *Conservation Element*, (CE), of cell j . The integral conservation law will then be

$$\int_{S(CE)} \vec{U} \cdot \hat{n} \, ds = 0 \quad (4.4)$$

where $S(CE)$ denotes the boundary of the conservation element while $\hat{n} (= (n_x, n_y, n_t))$ and ds , respectively, denote the unit outward normal vector and the area of a surface element on $S(CE)$. In order to perform the above surface integration, \vec{U} may be replaced by a first order Taylor series approximation about a suitably chosen node, (called a *solution point*), where the discretized values of \vec{U} and its derivatives are saved. In this method both \vec{U} and its first-order derivatives are considered the independent variables which must be determined. By “suitably chosen”, as will be shown shortly, it is intended that solution points are selected such that the method is explicit. Let (x'_j, y'_j) represent the spatial coordinates of the solution point related to cell j . Therefore, components of \vec{U} may be approximated as

$$\begin{aligned}\Psi(x, y, t; j, n) = & \Psi_j^n + (\Psi_x)_j^n (x - x'_j) \\ & + (\Psi_y)_j^n (y - y'_j) + (\Psi_t)_j^n (t - t^n)\end{aligned}\quad (4.5)$$

where Ψ_j^n , $(\Psi_x)_j^n$, $(\Psi_y)_j^n$, and $(\Psi_t)_j^n$ are constant coefficients associated with the solution point (x'_j, y'_j, t^n) , and Ψ can be any of the components of \vec{U} . Further, the derivatives of F and G can be found from Eq. (4.3), i.e.,

$$\begin{aligned}(F_x)_j^n = -k(T_{xx})_j^n, \quad (F_y)_j^n = -k(T_{xy})_j^n, \quad (F_t)_j^n = -k(T_{xt})_j^n \\ (G_x)_j^n = -k(T_{yx})_j^n, \quad (G_y)_j^n = -k(T_{yy})_j^n, \quad (G_t)_j^n = -k(T_{yt})_j^n\end{aligned}\quad (4.6)$$

where the coefficients $(T_{xx})_j^n$, $(T_{xy})_j^n$, $(T_{xt})_j^n$, $(T_{yx})_j^n$, $(T_{yy})_j^n$ and $(T_{yt})_j^n$ will be calculated later in the section related to the second-order derivatives.

In Eq. (4.5), the notation $H(x, y, t; j, n)$ [87] means the value of H at the point (x, y, t) is evaluated using the nodal values saved at the solution point (x'_j, y'_j, t^n) . The reason these need to be defined can be understood by considering the fact that each point on any of the surfaces indicated in Fig. 4.1(a) may be evaluated using different discrete values, e.g., the value of \vec{U} at a point on the $CV_1V_1'C'$ plane may be found using the expansion point of cell j at time level n as well as time level $n - 1 / 2$. Also, the value of \vec{U} at a point on the $CV_2C_1V_3$ plane may be found using the expansion point of cell j at time level $n - 1 / 2$ as

well as that of the neighboring cell, j_1 , at the same time level. To assign a unique value to each surface point while integrating, each surface needs to be related to one and only one (j, n) entity, which is called a *solution element*, (SE). Consequently, solution elements must be defined so that each component surface on the boundary of any conservation element belongs to an assigned solution element. Figure 4.1(b) shows two of four solution elements related to the cell j , i.e., $SE(j, n)$ which consists of the hexagon $C'_1 V'_3 C'_2 V'_1 C'_3 V'_2$ combined with three vertical rectangular planes cutting through it, $SE(j_3, n-1/2)$ that consists of the hexagon $C V_1 A B D V_2$ combined with three vertical rectangular planes cutting through it, where A , B , and D are related to the neighbor j_3 of cell j (not shown), and two other SE 's $(j_1, n-1/2)$ and $(j_2, n-1/2)$ that are built the same way. Using the notation convention introduced in [65], consider the $SE(j_1, n-1/2)$. The two lateral faces related to this SE , i.e., $C_1 V_2 V'_2 C'_1$ and $C_1 V_3 V'_3 C'_1$, (see Fig. 4.1(a)), will be referred to as $S(1, 1)$ and $S(2, 1)$, respectively. Furthermore, the areas of $S(1, 1)$ and $S(2, 1)$ will be referred to as $S^{(1,1)}$ and $S^{(2,1)}$, respectively, while $\hat{n}^{(1,1)}$, and $\hat{n}^{(2,1)}$ represent the unit normals of the above lateral faces, outward with respect to the octahedron. Furthermore, spatial coordinates of the centroid of each of these faces will be referred to as $(x_c^{(1,1)}, y_c^{(1,1)})$, and $(x_c^{(2,1)}, y_c^{(2,1)})$, respectively. Also the surface $C_1 V_3 C V_2$, that is the horizontal plane related to this SE , will be called $S(1)$, while its area will be referred to as $S^{(1)}$. The unit outward normal to this surface is $(0, 0, -1)$. In general, for $SE(j_k, n-1/2)$, $k = 1, 2, 3$, the lateral faces will be called $S(l, k)$, while their area, unit outward normal, and the spatial coordinates of their centroid will be referred to as $S^{(l,k)}$, $\hat{n}^{(l,k)} = (n_x^{(l,k)}, n_y^{(l,k)}, 0)$, and

$(x_c^{(l,k)}, y_c^{(l,k)})$, $l = 1, 2$, respectively. Also the corresponding horizontal plane will be denoted by $S(k)$, while its area, and the spatial coordinates of its centroid will be represented by $S^{(k)}$, and $(x_c^{(k)}, y_c^{(k)})$, respectively. Note that the so-called horizontal planes form the bottom of the octahedron. The horizontal planes that contain the top of the octahedron, however, belong to $SE(j, n)$. The area and spatial coordinates of the centroid of the top surfaces are equal to those of the bottom surfaces but their unit outward normal is $(0, 0, +1)$. Using the above conventions and performing the inner products, Eq. (4.4) can be written as

$$\begin{aligned}
 \int_{S(CE)} \vec{U} \cdot \hat{n} ds &= \sum_{k=1}^3 \left\{ \int_{S(k)} H(x, y, t; j, n)(+1) ds + \right. \\
 &\int_{S(k)} H(x, y, t; j_k, n-1/2)(-1) ds + \sum_{l=1}^2 \\
 &\left. \int_{S(l,k)} [F(x, y, t; j_k, n-1/2)n_x^{(l,k)} + G(x, y, t; j_k, n-1/2)n_y^{(l,k)}] ds \right\}
 \end{aligned} \tag{4.7}$$

where the first and second integrals are performed over the top and bottom surfaces, respectively, and the third integral is related to the lateral faces of the octahedral CE . Using Eq. (4.5), the third integral of Eq. (4.7) can be evaluated as follows

$$\begin{aligned}
I^{(l,k)} &= \int_{S(l,k)} [F(x, y, t; j_k, n-1/2) n_x^{(l,k)} + G(x, y, t; j_k, n-1/2) n_y^{(l,k)}] ds \\
&= \int_{S(l,k)} \{ [F_{j_k}^{n-1/2} + (F_x)_{j_k}^{n-1/2} (x - x'_{j_k}) + (F_y)_{j_k}^{n-1/2} (y - y'_{j_k}) + \\
&\quad (F_t)_{j_k}^{n-1/2} (t - t^{n-1/2})] n_x^{(l,k)} + [G_{j_k}^{n-1/2} + (G_x)_{j_k}^{n-1/2} (x - x'_{j_k}) + \\
&\quad (G_y)_{j_k}^{n-1/2} (y - y'_{j_k}) + (G_t)_{j_k}^{n-1/2} (t - t^{n-1/2})] n_y^{(l,k)} \} ds
\end{aligned} \tag{4.8}$$

Rearranging leads to

$$\begin{aligned}
I^{(l,k)} &= \int_{S(l,k)} ds \{ [F_{j_k}^{n-1/2} - (F_x)_{j_k}^{n-1/2} x'_{j_k} - \\
&\quad (F_y)_{j_k}^{n-1/2} y'_{j_k} - (F_t)_{j_k}^{n-1/2} t^{n-1/2}] n_x^{(l,k)} + \\
&\quad [G_{j_k}^{n-1/2} - (G_x)_{j_k}^{n-1/2} x'_{j_k} - (G_y)_{j_k}^{n-1/2} y'_{j_k} - (G_t)_{j_k}^{n-1/2} t^{n-1/2}] n_y^{(l,k)} \} \\
&\quad + [(F_x)_{j_k}^{n-1/2} n_x^{(l,k)} + (G_x)_{j_k}^{n-1/2} n_y^{(l,k)}] \int_{S(l,k)} x ds \\
&\quad + [(F_y)_{j_k}^{n-1/2} n_x^{(l,k)} + (G_y)_{j_k}^{n-1/2} n_y^{(l,k)}] \int_{S(l,k)} y ds \\
&\quad + [(F_t)_{j_k}^{n-1/2} n_x^{(l,k)} + (G_t)_{j_k}^{n-1/2} n_y^{(l,k)}] \int_{S(l,k)} t ds
\end{aligned} \tag{4.9}$$

But $\int_{S(l,k)} ds$ is the area of the corresponding lateral face and the rest of the above integrals

may be evaluated using the space-time coordinates of its centroid. Therefore, the integral becomes

$$\begin{aligned}
I^{(l,k)} &= \{ F(x_c^{(l,k)}, y_c^{(l,k)}, t^n - \Delta t/4; j_k, n-1/2) n_x^{(l,k)} \\
&\quad + G(x_c^{(l,k)}, y_c^{(l,k)}, t^n - \Delta t/4; j_k, n-1/2) n_y^{(l,k)} \} S^{(l,k)}
\end{aligned} \tag{4.10}$$

Following a similar procedure, the first and second integrals of Eq. (4.7) become

$$\int_{S^{(k)}} H(x, y, t; j, n) (+1) ds = S^{(k)} \left[H_j^n + (H_x)_j^n (x_c^{(k)} - x'_{j_k}) + (H_y)_j^n (y_c^{(k)} - y'_{j_k}) \right] \quad (4.11)$$

and

$$\begin{aligned} \int_{S^{(k)}} H(x, y, t; j_k, n - 1/2) (-1) ds &= -S^{(k)} \left[H_{j_k}^{n-1/2} + (H_x)_{j_k}^{n-1/2} (x_c^{(k)} - x'_{j_k}) + (H_y)_{j_k}^{n-1/2} (y_c^{(k)} - y'_{j_k}) \right] \\ &= -S^{(k)} H(x_c^{(k)}, y_c^{(k)}, t^{n-1/2}; j_k, n - 1/2) \end{aligned} \quad (4.12)$$

respectively. Equation (4.7), after substitution of the evaluated integrals, provides an expression for H_j^n . The expression contains three unknowns H_j^n , $(H_x)_j^n$, and $(H_y)_j^n$, but examination of the expressions which contain $(H_x)_j^n$ and $(H_y)_j^n$ suggests that they may be eliminated, resulting in an explicit method, provided the solution point is chosen at the centroid of the hexagon $C_1V_3C_2V_1C_3V_2$ formed by the vertices of cell j and the centroids of its three neighbors. Using this, the equation for H_j^n can be written in a convenient manner. Note that despite the apparent complexity, the equation for H_j^n is in fact composed of three similar parts, each related to one of the neighboring cells.

$$H_j^n = \sum_{k=1}^3 R^{(k)} / \sum_{k=1}^3 S^{(k)} \quad (4.13)$$

where

$$R^{(k)} = S^{(k)} H \left(x_c^{(k)}, y_c^{(k)}, t^{n-1/2}; j_k, n-1/2 \right) - \sum_{l=1}^2 I^{(l,k)} \quad (4.14)$$

and $I^{(l,k)}$ is evaluated using Eq. (4.10).

The above formulation has the important attribute of being able to handle nonlinearities that may exist in the definition of functions H , F and G .

Once the values of enthalpy are updated over the entire domain, Eq. (2.6) can be used to obtain the temperature field, and the first and second order derivatives of the field parameters may be calculated as presented in the following sections.

4.1.1. First-Order Derivatives

As described in detail in [87], the first-order derivatives of the field parameters can be evaluated from

$$\left(\Psi_x \right)_j^n = \frac{\sum_{k=1}^3 \left| \mathbf{q}_m \mathbf{q}_p \right|^{\tilde{\mathbf{a}}} \Psi_x^{(k)}}{\sum_{k=1}^3 \left| \mathbf{q}_m \mathbf{q}_p \right|^{\tilde{\mathbf{a}}}}, \quad \left(\Psi_y \right)_j^n = \frac{\sum_{k=1}^3 \left| \mathbf{q}_m \mathbf{q}_p \right|^{\tilde{\mathbf{a}}} \Psi_y^{(k)}}{\sum_{k=1}^3 \left| \mathbf{q}_m \mathbf{q}_p \right|^{\tilde{\mathbf{a}}}} \quad (4.15)$$

where

$$\mathbf{q}_k = \sqrt{\left(\Psi_x^{(k)} \right)^2 + \left(\Psi_y^{(k)} \right)^2}, \quad k = 1, 2, 3 \quad (4.16)$$

and, for any given integer, $k = 1, 2, 3$, $\{k\} \cup \{m, p\} = \{1, 2, 3\}$. Parameters $\Psi_x^{(k)}$ and $\Psi_y^{(k)}$ are calculated solving the following three systems, each containing two equations and two unknowns. Parameter Ψ can be either H or T .

$$\begin{aligned}
 (x'_{j_k} - x'_j)\Psi_x^{(1)} + (y'_{j_k} - y'_j)\Psi_y^{(1)} &= \Psi_{j_k}^n - \Psi_j^n, & k=2,3 \\
 (x'_{j_k} - x'_j)\Psi_x^{(2)} + (y'_{j_k} - y'_j)\Psi_y^{(2)} &= \Psi_{j_k}^n - \Psi_j^n, & k=1,3 \\
 (x'_{j_k} - x'_j)\Psi_x^{(3)} + (y'_{j_k} - y'_j)\Psi_y^{(3)} &= \Psi_{j_k}^n - \Psi_j^n, & k=1,2
 \end{aligned} \tag{4.17}$$

The constant $\tilde{\alpha}$, in Eq.(4.15), is usually set equal to 1. The above weighted average provides the necessary numerical damping [69]. Note that, to avoid dividing by zero, in practice a small positive number (e.g. 10^{-20}) is added to the denominators in Eq. (4.15).

4.1.2. Second-Order Derivatives

As explained in [69], once the first order derivatives of the temperature field are known, expanding $(T_x)_{j_k}^{n-1/2}$, $k=1,2,3$, which is saved at the solution point $(S_k, n-1/2)$ about the space-time solution point (S, n) , results in three equations

$$\begin{aligned}
 (x'_{j_k} - x'_j)(T_{xx})_j^n + (y'_{j_k} - y'_j)(T_{xy})_j^n - \frac{\Delta t}{2}(T_{xt})_j^n = \\
 (T_x)_{j_k}^{n-1/2} - (T_x)_j^n, \quad k=1, 2, 3
 \end{aligned} \tag{4.18}$$

These may be solved simultaneously for $(T_{xx})_j^n$, $(T_{xy})_j^n$, and $(T_{xt})_j^n$. A similar system gives $(T_{yx})_j^n$, $(T_{yy})_j^n$, and $(T_{yt})_j^n$. Using this technique, the mesh values of second-order derivatives of T can be evaluated in order to be used in Eq. (4.6). The first-order derivatives of flux functions, evaluated from Eq. (4.6), can then be used in Eq. (4.13).

4.1.3. Boundary Conditions

In order to treat the boundary conditions, a ghost cell is defined for each boundary cell. Geometrically, the ghost cell is a mirror image of the corresponding boundary cell with respect to the boundary, as shown in Fig. 4.2 where S_j and S_g denote solution points related to the boundary cell and the ghost cell, respectively, and B is the intersection of the line segment $S_g S_j$ with the boundary. Let Ψ be a field parameter, which can be either enthalpy or temperature.

- 1) Constant temperature boundary $\Psi_B = Const.:$

Using a linear interpolation

$$\Psi_g = 2\Psi_B - \Psi_j \quad (4.19)$$

All the derivatives at “g” may then be set equal to their corresponding values at “j”.

2) An insulated boundary or axis of symmetry:

Let \mathbf{s} and \mathbf{t} be the normal and tangential directions to the boundary,

respectively. The insulation condition is then $\left(\frac{\partial T}{\partial \mathbf{s}} \right)_{boundary} = 0$ and considering

$$\frac{\partial H}{\partial \mathbf{s}} = c \frac{\partial T}{\partial \mathbf{s}} \text{ it also leads to } \left(\frac{\partial H}{\partial \mathbf{s}} \right)_{boundary} = 0. \text{ The reader is referred to [87]}$$

for details of reflecting boundary conditions.⁶

4.2 Numerical results and discussion

To assess the accuracy and effectiveness of the two-dimensional CE/SE method applied to conduction problems with phase change, several classical cases were solved and the results were compared to the existing analytical solutions.

In order to begin the validation of the computer program, and specially to study the error behavior of the numerical scheme, the following two cases were designed and applied to a unit square geometry, with $k = 1$.

Case 1. $H = T$ and $T = x + y$, (4.20)

Case 2. $H = T$ and $T = 2t + (x^2 + y^2) / 2$. (4.21)

⁶ Also see Chapter 6, where the insulated boundary conditions are derived, in detail, for a general three-dimensional problem. Further, see Chapter 5 for boundary conditions of the third kind, i.e., convective boundary conditions.

As can be seen, the above temperature distributions satisfy the governing equation, (Eq. (4.1)). The following, contains the details of the above cases, along with several other phase change validation cases.

4.2.1 The Steady Linear Case

This case is a steady linear problem, for which it can be easily shown that the CE/SE formulation is exact, in the sense that no truncation error exists. Therefore, the spatial grid is not an issue in this case. On the other hand, the time-step issue needs to be studied. Equation (4.20) was applied on the boundaries, with an initially imposed error distribution over the entire domain. The results confirmed that, after a period of time, the temperature converges to the accurate distribution everywhere in the field.

The error behavior was studied, for the steady case above, for different time-steps. Since the present method is explicit, there are stability restrictions on the time-step. Numerical experiments reveal the existence of three time-step zones:

- 1) Large time steps leading to enlarging errors.
- 2) Medium time steps leading to non-vanishing but bounded errors for which the upper error bound reduces with reducing time step. This zone can be seen in Fig. 4.3, where absolute error (norm of infinity of the difference between the numerical and exact solutions) is depicted versus the iterations.
- 3) Small time steps that lead to stable, time step independent results, with errors vanishing to the order of machine zero. This zone is shown in Fig. 4.4. As can

be seen, the fastest convergence rate is achieved by using the largest time-step that falls within this category.

Figure 4.4 also shows that once the lower bound is achieved, the errors do not grow with further iteration. Additional numerical experiments confirmed the following facts: a) The same pattern was detected for other problems, b) once the time-step is selected for a spatial mesh, it can be used for other phase-change problems on the same mesh.

It is worthwhile to note that in both zone 2 and zone 3, a stable converged solution is achievable, while only one of them gives the correct solution. This problem can be easily resolved noting that by slightly changing the time-step in zone 2, results change dramatically, a phenomenon that does not occur in zone 3. Based on the above results, the procedure of choosing the optimum time-step for a spatial grid, may be summarized as starting from a large time-step, (a good initial guess could be obtained from the one-dimensional, necessary, stability condition derived in the previous chapter), and reducing it until stable, time-step independent results are achieved.

Comparison of the above zone 3 with the zone 3 of the one-dimensional version, (see section 3.4.1), confirms the fact that the two-dimensional stability criterion is more restrictive. Zone 3(a) of the one-dimensional case does not exist for its two-dimensional counterpart.

4.2.2 A Problem with Time-Dependent Boundary Conditions

For this transient problem, unlike the previous case, there is a truncation error associated with the second-order accuracy of the CE/SE method. Clearly, this error should decrease by

using finer spatial grids. Equation (4.21) was applied on the boundaries. Both the exact solution and a uniform error distribution were used as initial conditions. Several spatial grids were used for this case. A grid that has 50 nodes on each side of the unit square will be referred to as the coarse grid, while the so-called fine grid consists of 100 nodes on each side of the unit square. The absolute errors (error is defined as the infinity norm of the absolute value of the difference between the numerical and exact solutions over the entire domain) are shown in Fig. 4.5. This figure confirms that refining the grid reduces the size of the truncation error. The rate of this decrease is related to the actual order of accuracy of the numerical scheme. Therefore, using a number of different spatial grid increments, we can numerically demonstrate that the method is second-order. In Fig. 4.6, the average absolute errors are plotted versus the spatial grid spacing. Examining the slope of this log-log plot, the second-order accuracy of the method is confirmed.

4.2.3 Freezing of a Finite Slab (a One-Phase Stefan Problem)

Consider a slab of thickness L with the initial state assumed to be liquid at the fusion temperature T_f (Fig. 4.7). At $t = 0$, the temperature of the surface at $x = 0$ drops to T_w and is held there. The surface at $x = L$ is effectively insulated. The analytical solution of this problem, from [92] determines the phase change interface is located at

$$x_{\text{int.}} = 2g\sqrt{a_s t} \quad (4.22)$$

where \mathbf{a}_s is the thermal diffusivity of the solid phase and \mathbf{g} is obtained by solving

$$\mathbf{g} e^{\mathbf{g}^2} \operatorname{erf}(\mathbf{g}) = \frac{c_s(T_f - T_w)}{L_f \sqrt{\mathbf{p}}} \quad (4.23)$$

where c_s denotes the specific heat of the solid phase and L_f is the latent heat of fusion.

Also the temperature in the solid region is determined from

$$T = T_w + \frac{T_f - T_w}{\operatorname{erf}(\mathbf{g})} \operatorname{erf}(\mathbf{h}) \quad (4.24)$$

where $\mathbf{h} = \frac{x}{2\sqrt{\mathbf{a}_s t}}$.

In order to model this one-dimensional problem using the two-dimensional code, the top and bottom of the slab are assumed to be insulated since any horizontal line can be regarded as a line of symmetry in this problem.

The above problem is studied for a range of Stefan numbers. Other parameters are $T_w = -1.0^\circ\text{C}$, $T_f = 0.0^\circ\text{C}$, while the thermal diffusivity and specific heats are set equal to unity. Figure 4.8 shows the position of phase-change interface compared to the analytical solution for $S_t = 0.05, 0.1, 4.0$, and 10.0 , where $S_t = c_s(T_f - T_w)/L_f$ is the Stefan number. Temperature distributions at $t = 0.14$ s are also compared to the analytical solution in Fig.

4.9. As can be seen, accurate results are obtained for a range of large and small Stefan numbers.

For small Stefan numbers, the accuracy was improved by using a slightly different method for calculation of first-order derivatives. The CE/SE method, in its present form, loses its second-order accuracy and becomes dissipative for $S_t < 1$. The dissipation, however, is adjustable by the changing the parameter \tilde{a} , as mentioned in Section 4.1.1. Accurate results for $S_t = 0.05$, and 0.1 are obtained using $\tilde{a} < 1$. It is possible, however, to design a CE/SE scheme in a way that the above adjustment occurs automatically and the method becomes insensitive to the size of Stefan number. Chapter 7 is a detailed study of this subject.

4.2.4 Heat Conduction with Freezing in a Corner

The problem under consideration here is the phase change of a liquid contained in an infinite corner (Fig. 4.10). The liquid has a uniform temperature $T_L \geq T_f$ and for time $t \geq 0$, the surfaces $x = 0$ and $y = 0$ are maintained at a constant temperature $T_w < T_f$.

The analytical solution of this problem, which is of similarity nature, is discussed in detail in [93]. Briefly, the non-dimensional interface position, $f(x^*)$, can be determined from

$$f(x^*) = \left[I^m + \frac{C}{x^{*m} - I^m} \right]^{1/m} \quad (4.25)$$

where $x^* = \frac{x}{\sqrt{4\mathbf{a}t}}$, \mathbf{a} is the thermal diffusivity which is assumed to be equal for both solid and liquid phases, \mathbf{l} (asymptote shown in Fig. 4.10) is calculated by solving the following equation

$$\frac{\exp(-\mathbf{l}^2)}{\operatorname{erf}(\mathbf{l})} - \frac{T_i^* \exp(-\mathbf{l}^2)}{\operatorname{erfc}(\mathbf{l})} = \sqrt{\mathbf{p}} \mathbf{b} \mathbf{l} \quad (4.26)$$

where $T_i^* = \frac{k_L}{k_S} \left(\frac{T_L - T_f}{T_f - T_w} \right)$, the non-dimensional initial temperature and $\mathbf{b} = \frac{L_f}{c_S (T_f - T_w)}$,

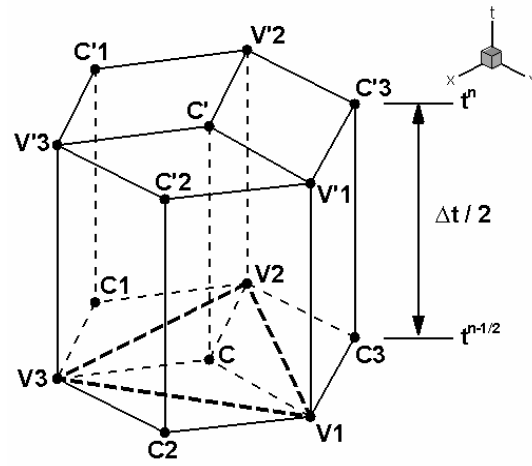
the latent to sensible heat ratio are two non-dimensional parameters needed for completely defining this problem. Constants C and m in Eq. (4.25) are determined for each case using T_i^* and \mathbf{b} [93]. The numerical simulation is performed using insulated walls at $x = 3.0$ and $y = 3.0$. Results are shown for $\mathbf{b} = 0.25$ and $T_i^* = 0.3$ (which imply that $C = 0.159$ and $m = 5.02$ [94]). Constant temperature contours, at $t = 0.02$ seconds, are shown in Fig. 4.11 and the non-dimensional interface position is compared to the analytical results in Fig. 4.12. An example of the unstructured mesh used for all of the square domain cases is shown in Fig. 4.13.

4.2.5 Inward Freezing in a Circular Pipe

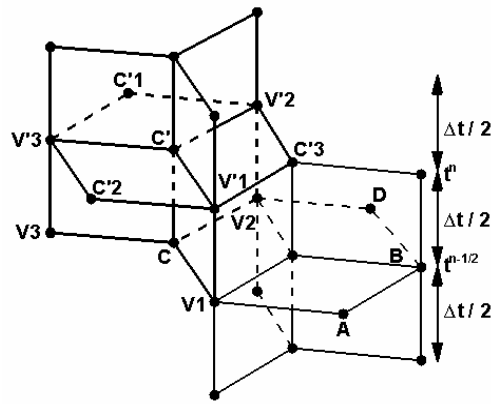
The inward phase change of a liquid within a cylindrical boundary is important in dealing with freezing of water in pipes and allied problems. A number of approximate solutions are available for this finite domain problem [92]. As a result of symmetry, only a quarter of a circle need be studied; the geometry is given in Fig. 4.14 and an example of the spatial mesh is shown in Fig. 4.15. The numerical results are obtained for a quarter circle of unit radius with the initial state assumed to be liquid at the fusion temperature. Other parameters are $T_w = -1.0^\circ C$, $T_f = 0.0^\circ C$, and $L_f = 0.25 J/kg$ while the thermal diffusivity and specific heats are set equal to unity. The position of the phase change interface at different times is shown in Fig. 4.16, these graphs are generated using enthalpy contours that range from H_{sf} to H_{lf} . The enthalpy distribution in the circle is given in Fig. 4.17 for an intermediate time of $t = 0.11$ s. The total freezing time (t_f) is determined to be between 0.18 s and 0.19 s, which is in agreement with the approximate solution given in [92]. This approximate solution may be expressed as

$$\frac{a t_f}{R^2} = \frac{1}{4S_t} + \frac{1}{8} \quad (4.27)$$

where R is the radius of the circle, a denotes the diffusivity. This approximate relation, for this case, gives a total freezing time of $t_f = 0.1875$ s.



(a)



(b)

Figure 4.1: Computational molecule of CE/SE method, (a) CEs and (b) SEs

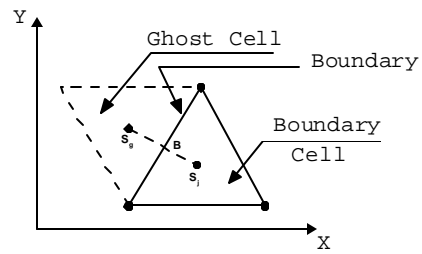


Figure 4.2: Boundary and ghost cells.

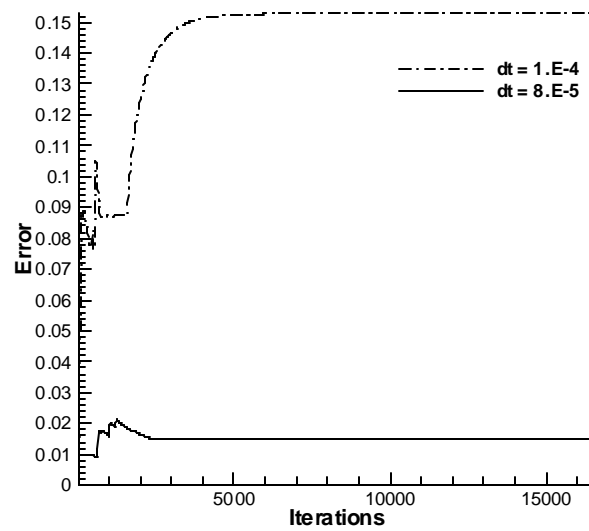


Figure 4.3: Bounded growth of errors (Zone 2)

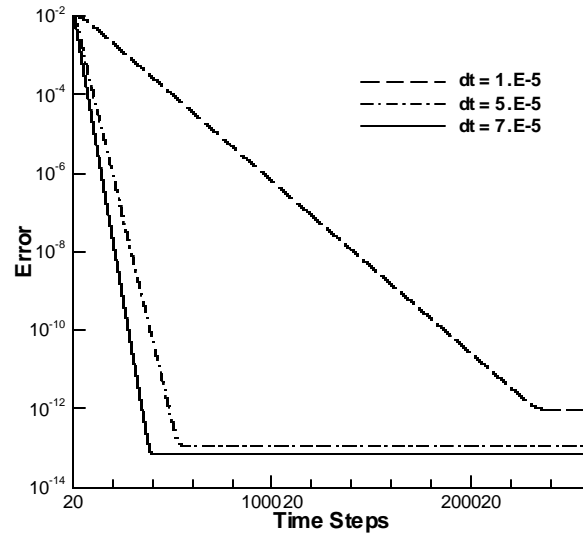


Figure 4.4: Vanishing errors (zone 3)

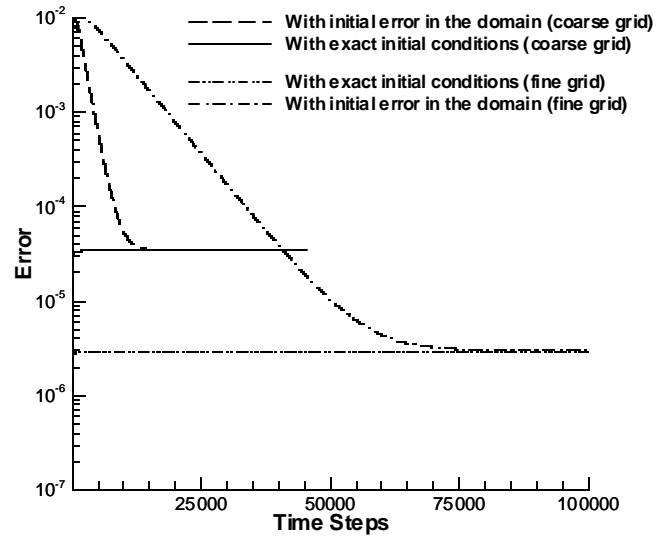


Figure 4.5: The grid-dependent truncation error.

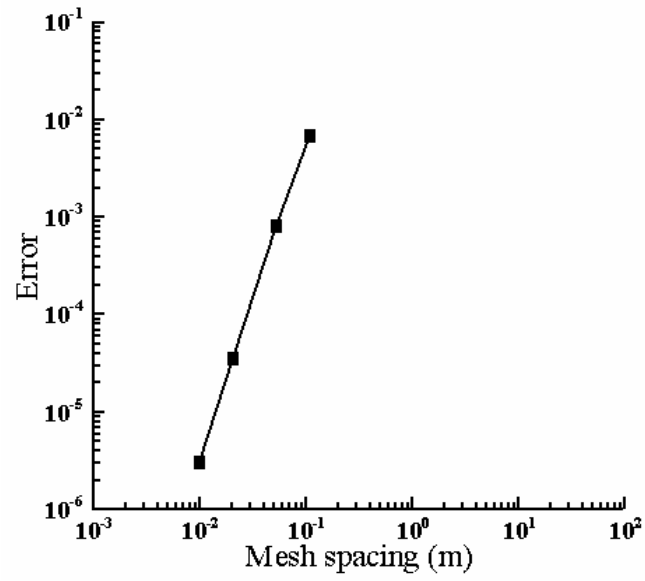


Figure 4.6: Demonstration of two-dimensional CE/SE scheme's second-order accuracy

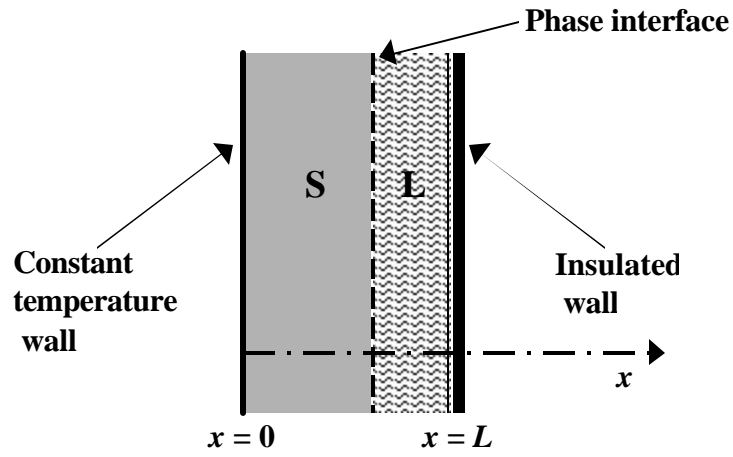


Figure 4.7: Geometry of the freezing slab case

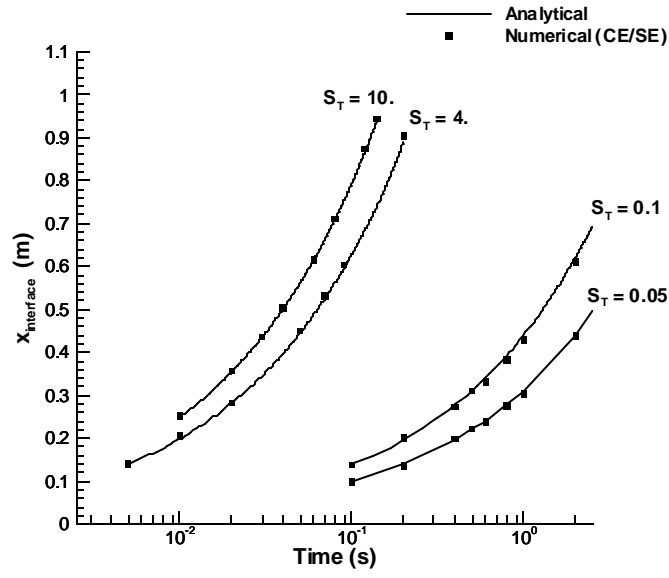


Figure 4.8: Location of the interface for the freezing slab case

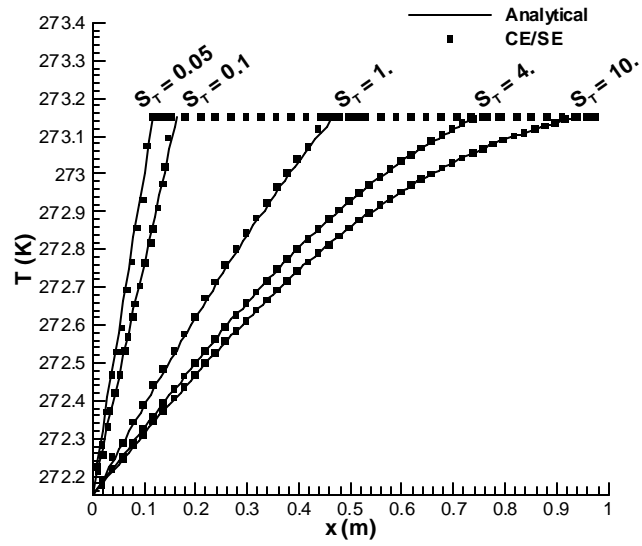


Figure 4.9: Temperature distribution at $t = 0.14$ for the freezing slab case

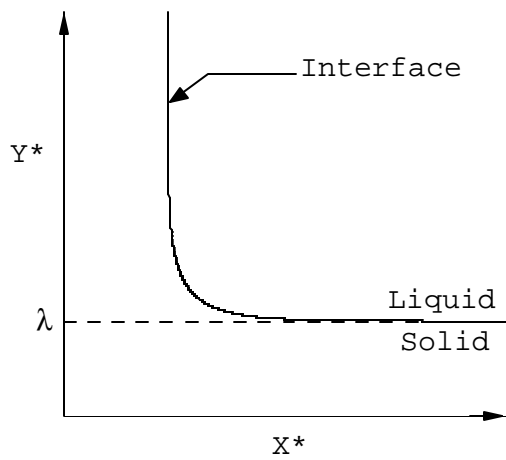


Figure 4.10: Geometry for the freezing corner case

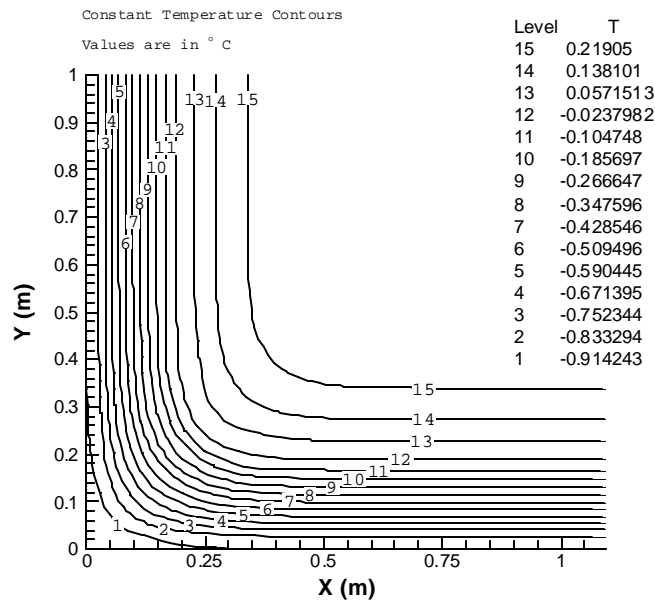


Figure 4.11: Temperature isotherms at $t = 0.02$ s, for the freezing corner case

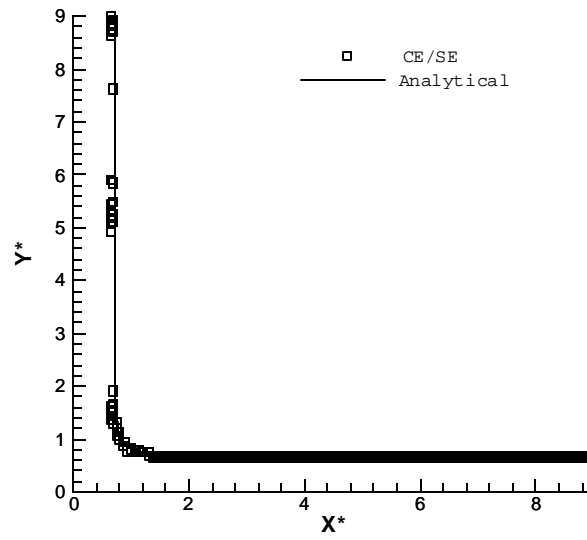


Figure 4.12: Non-dimensional interface for the freeing corner case

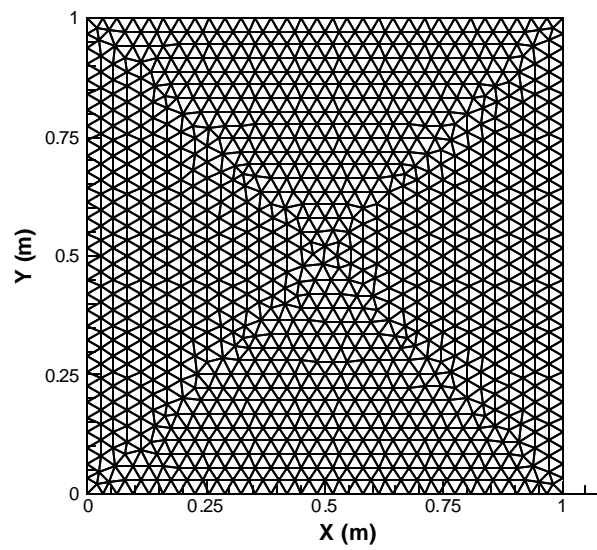


Figure 4.13: An example of the grid within a square

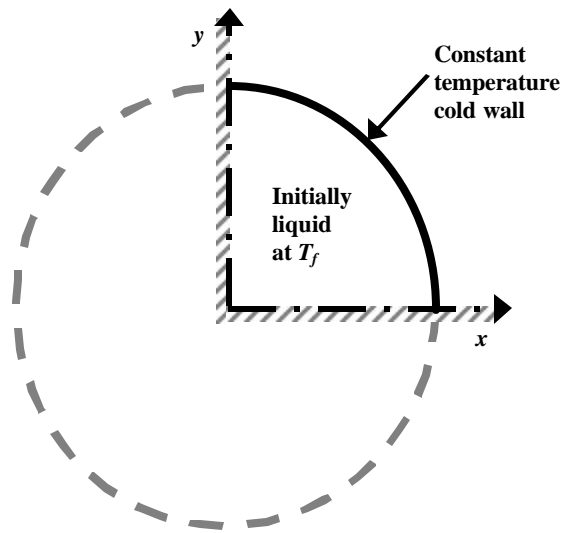


Figure 4.14: Geometry of the inward freezing pipe case

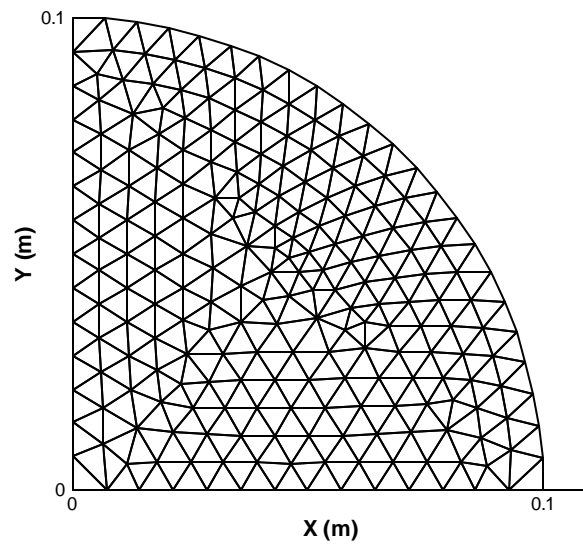


Figure 4.15: An example mesh for the inward freezing pipe case

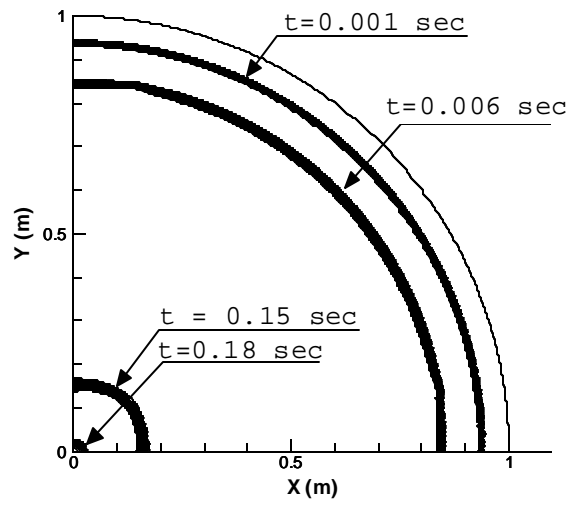


Figure 4.16: The interface position for the inward freezing pipe case

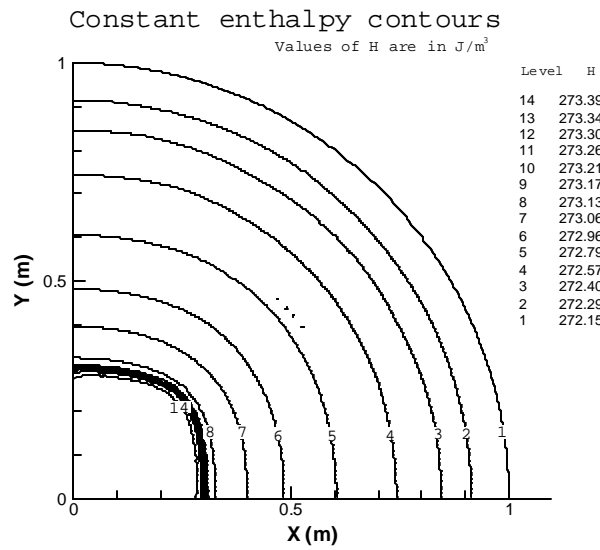


Figure 4.17: Enthalpy contours at $t = 0.11$ s for the inward freezing pipe case

Chapter 5

AXISYMMETRIC CE/SE PHASE-CHANGE SCHEME

Many three-dimensional problems can be modeled as axisymmetric. Therefore, having an axisymmetric version of the solver can save a great amount of time and computational power while treating those problems.

In this chapter the development of an axisymmetric CE/SE phase change solver is undertaken. It explores axisymmetric formulation options and determines which option leads to a stable efficient solver. In addition to the derivation, several numerical validations are also presented to demonstrate convergence and accuracy of the axisymmetric scheme. The boundary conditions are also extended to include the convective boundary condition and its numerical implementation.

5.1 Development of an Axisymmetric CE/SE Scheme for Heat Conduction with Melting/Freezing

The axisymmetric version of the governing equation (Eq.(2.3)), can be written as

$$\frac{\partial H}{\partial t} = k \left(\frac{\partial^2 T}{\partial r^2} + \frac{1}{r} \frac{\partial T}{\partial r} + \frac{\partial^2 T}{\partial z^2} \right) \quad (5.1)$$

Equation (2.6) can be used without change.

Consider the following PDE which can represent a variety of conservation laws depending upon the definition of H and the flux functions F and G

$$\frac{\partial H}{\partial t} + \frac{\partial F}{\partial x_1} + \frac{\partial G}{\partial x_2} = 0 \quad (5.2)$$

where x_1 and x_2 are coordinates of a two-dimensional Cartesian system. As a special case note that the two-dimensional Cartesian version of Eq. (2.3), in the xy -plane, can be written in the above form defining for example

$$F = -k \frac{\partial T}{\partial x}, \quad G = -k \frac{\partial T}{\partial y} \quad (5.3)$$

The CE/SE method applied to the above case was studied in the previous chapter, and its accuracy and efficiency were assessed.

The axisymmetric governing equation, (Eq. (5.1)), can also be written in the form of Eq. (5.2) by letting $x_1 = r$ and $x_2 = z$ represent the radial and axial coordinates, respectively, and writing Eq. (5.1) in its conservation form

$$\frac{\partial(rH)}{\partial t} + \frac{\partial}{\partial r} \left(-k r \frac{\partial T}{\partial r} \right) + \frac{\partial}{\partial z} \left(-k r \frac{\partial T}{\partial z} \right) = 0 \quad (5.4)$$

The CE/SE formulation, presented in the previous chapter, would be therefore directly applicable. However, after writing the code it was observed that the above formulation does not lead to a stable numerical method for axisymmetric cases. An explanation for this phenomenon follows.

Although Eq.(5.2) can be used as a general form for describing many physical phenomena, the properties of the resulting numerical schemes may be very different depending on each individual PDE. Further, even for different formulations of a single PDE, the resulting numerical schemes may vary in performance, dissipative/dispersive behavior, and stability range, depending on the specific forms of the functions H , F , and G for each individual formulation. Some formulations, such as Eq. (5.4), may render unconditionally unstable schemes. Therefore, in search of a stable, (or marginally stable), axisymmetric scheme, an alternative approach is used in which the $\frac{1}{r} \frac{\partial T}{\partial r}$ term in Eq. (5.1) is treated as a source term,

i.e.,

$$\frac{\partial H}{\partial t} + \frac{\partial}{\partial r} \left(-k \frac{\partial T}{\partial r} \right) + \frac{\partial}{\partial z} \left(-k \frac{\partial T}{\partial z} \right) = \frac{k}{r} \frac{\partial T}{\partial r} \quad (5.5)$$

Or, in a general form similar to that in Eq. (5.2)

$$\frac{\partial H}{\partial t} + \frac{\partial F}{\partial r} + \frac{\partial G}{\partial z} = \tilde{S} \quad (5.6)$$

where $\tilde{S} = \frac{k}{r} \frac{\partial T}{\partial r}$ represents the source term, and the flux functions F and G are

defined as $F = -k \frac{\partial T}{\partial r}$ and $G = -k \frac{\partial T}{\partial z}$.

Considering (r, z, t) as coordinates of a three-dimensional Euclidean space-time, Eq. (5.6) can be written as

$$\vec{\nabla} \bullet \vec{U} = \tilde{S}, \quad \vec{U} = (F, G, H) \quad (5.7)$$

A two-dimensional, unstructured, space-time mesh is used here which consists of Delaunay triangulation on the rz -plane that, considering the time axis as the third dimension, makes prisms perpendicular to the rz -plane. Axisymmetric CE's and SE's are defined in an analogous manner to the two-dimensional case. The integral conservation law will then be

$$\int_{S(CE)} \vec{U} \bullet \hat{n} ds = \int_{V(CE)} \tilde{S} dV \quad (5.8)$$

where $S(CE)$ denotes the boundary of the conservation element while $\hat{n} (= (n_r, n_z, n_t))$ and ds , respectively, denote the unit outward normal vector and the

area of a surface element on $S(CE)$. In order to perform the above surface integrations related to the left hand side of the above equation can be calculated as in the two-dimensional case, as explained in the previous chapter. For calculating the right hand side of Eq. (5.8), \tilde{S} is approximated as follows

$$\begin{aligned} \tilde{S}(r, z, t; j, n) = & \tilde{S}_j^n + \left(\tilde{S}_r\right)_j^n (r - r'_j) + \left(\tilde{S}_z\right)_j^n (z - z'_j) \\ & + \left(\tilde{S}_t\right)_j^n (t - t^n) \end{aligned} \quad (5.9)$$

By replacing (x, y) in Fig. 4.1 with (r, z), its axisymmetric counterpart results, in which, $V(CE)$ can be written as

$$V(CE) = \sum_{k=1}^3 V^{(k)} \quad (5.10)$$

where

$$V^{(k)} = S^{(k)}(\Delta t/2) \quad (5.11)$$

Therefore, the right hand side integral of Eq. (5.8), can be calculated as follows

$$\begin{aligned}
\int_{V(CE)} \tilde{S} dV &= \sum_{k=1}^3 \int_{V^{(k)}} \{ \tilde{S}_{j_k}^{n-1/2} + (\tilde{S}_r)_{j_k}^{n-1/2} (r - r'_{j_k}) \\
&\quad + (\tilde{S}_z)_{j_k}^{n-1/2} (z - z'_{j_k}) + (\tilde{S}_t)_{j_k}^{n-1/2} (t - t^{n-1/2}) \} dV \\
&= \frac{\Delta t}{2} \sum_{k=1}^3 S^{(k)} \{ \tilde{S}_{j_k}^{n-1/2} + (\tilde{S}_r)_{j_k}^{n-1/2} (r_c^{(k)} - r'_{j_k}) \\
&\quad + (\tilde{S}_z)_{j_k}^{n-1/2} (z_c^{(k)} - z'_{j_k}) + \frac{\Delta t}{4} (\tilde{S}_t)_{j_k}^{n-1/2} \}
\end{aligned} \tag{5.12}$$

Quantities $\tilde{S}_{j_k}^{n-1/2}$, $(\tilde{S}_r)_{j_k}^{n-1/2}$, $(\tilde{S}_z)_{j_k}^{n-1/2}$, and $(\tilde{S}_t)_{j_k}^{n-1/2}$ are saved at the solution point of cell j_k , and are considered constant on the corresponding solution element. Using a definition analogous to that of Eq. (5.9), the above volume integral can also be written as

$$\int_{V(CE)} \tilde{S} dV = \frac{\Delta t}{2} \sum_{k=1}^3 S^{(k)} \tilde{S}(r_c^{(k)}, z_c^{(k)}, t^n - \Delta t/4; j_k, n-1/2) \tag{5.13}$$

Equation (5.8), after substitution of the evaluated integrals, provides an expression for H_j^n . The expression contains three unknowns H_j^n , $(H_r)_j^n$, and $(H_z)_j^n$, but examination of the expressions which contain $(H_r)_j^n$ and $(H_z)_j^n$ suggests that they may be eliminated, resulting in an explicit method, provided the solution point is chosen at the centroid of the hexagon $C_1 V_3 C_2 V_1 C_3 V_2$ formed by the vertices of cell j and the centroids of its three neighbors. Following this approach, the equation

for H_j^n can be written in a convenient manner. Note that despite the apparent complexity, the equation for H_j^n is in fact composed of three similar parts, each related to one of the neighboring cells.

$$H_j^n = \sum_{k=1}^3 R^{(k)} \bigg/ \sum_{k=1}^3 S^{(k)} \quad (5.14)$$

where

$$R^{(k)} = S^{(k)} \left\{ H\left(r_c^{(k)}, z_c^{(k)}, t^{n-1/2}; j_k, n-1/2\right) + \frac{\Delta t}{2} \tilde{S}\left(r_c^{(k)}, z_c^{(k)}, t^n - \Delta t/4; j_k, n-1/2\right) \right\} - \sum_{l=1}^2 I^{(l,k)} \quad (5.15)$$

and $I^{(l,k)}$ is calculated from

$$I^{(l,k)} = \left\{ F\left(r_c^{(l,k)}, z_c^{(l,k)}, t^n - \Delta t/4; j_k, n-1/2\right) n_r^{(l,k)} + G\left(r_c^{(l,k)}, z_c^{(l,k)}, t^n - \Delta t/4; j_k, n-1/2\right) n_z^{(l,k)} \right\} S^{(l,k)} \quad (5.16)$$

Determination of the first and second-order derivatives is performed just as in those of the two-dimensional Cartesian case.

5.1.1. Convective Boundary Conditions

In addition to the boundary conditions explained in Chapter 4, here the boundary condition of the third kind, i.e., convection boundary condition, is also used:

Assuming a film coefficient, h , at an ambient temperature of T_∞ , this boundary condition can be written as

$$h(T_B - T_\infty) = -k \left(\partial T / \partial \mathbf{s} \right)_B \quad (5.17)$$

where \mathbf{s} is the outward normal direction to the boundary. Central differences can then be easily used to extract an expression for T_g , using T_B from the Eq. (5.17).

5.2 Numerical Results and Discussion

To assess the validity and accuracy of the axisymmetric CE/SE formulation, the following problems were designed and applied to a unit cylindrical geometry, using a fictitious material with unit conductivity.

$$\textbf{Case 1.} \quad H = T \text{ and } T = z \quad (5.18)$$

$$\textbf{Case 2.} \quad H = T \text{ and } T = 3 \, t + r^2 / 2 + z^2 / 2 \quad (5.19)$$

As can be seen, the above temperature distributions satisfy the axisymmetric governing equation (Eq. (5.1)). The following, contains the details of the above cases, along with several other axisymmetric phase change cases.

5.2.1. Case 1: Time-Step Effects

This case is a steady linear problem, for which it can be easily shown that the CE/SE formulation is exact, in the sense that no truncation error exists. Therefore, the spatial grid is not an issue in this case. On the other hand, the time-step issue needs to be studied. Equation (5.18) was applied on the boundaries, with an initially imposed error distribution over the entire domain. The results obtained confirmed that, after a period of time, the temperature converges to the accurate distribution everywhere in the field. Figure 5.1 shows the absolute error (which is defined as the infinity norm of the difference between the numerical and exact solutions) versus the iterations for different time steps. The errors are seen to vanish to the order of machine zero.

Using this case, the error behavior was studied, for different time-steps. Since the present method is explicit, there are stability restrictions on the time-step. The error behavior for the axisymmetric case was observed to be similar to that obtained for the two-dimensional analysis, which was discussed in detail in Chapter 4.

5.2.2. Case 2: Spatial Grid Size Effects

For this transient problem (see Eq. (5.19)), unlike the previous case, there is a truncation error associated with second-order accuracy of the CE/SE method. Clearly, this error should decrease by using finer spatial grids. Figure 5.2 was generated using two spatial grids. A grid that has 1,700 cells will be referred to as the coarse grid, while the so-called fine grid consists of 3,964 cells. Equation (5.19) was then applied on the boundaries. Both the exact solution and a uniform error distribution were used as initial conditions. The absolute average errors (defined as the arithmetic average of the absolute value of the difference between the numerical and exact solutions, over the entire domain) are shown in Fig. 5.2. This figure confirms that refining the grid reduces the size of the truncation error. As mentioned in the previous chapter, the rate of this decrease is related to the actual order of accuracy of the numerical scheme. Therefore, using a number of different spatial grid increments, we can numerically demonstrate that the method is second-order. In Fig. 5.3, the average absolute errors are plotted versus the spatial grid spacing. Examining the slope of this log-log plot, the second-order accuracy is also confirmed for the axisymmetric scheme.

5.2.3. Cases of the Thawing Cone

Thawing of a cone, with a cone half angle of 30 degrees, was studied using the axisymmetric scheme. All cases start from a frozen initial state at the fusion

temperature with different boundary conditions. An example mesh for all conical cases is given in Fig. 5.4. For these cases, the position of the phase change interface at different times is shown in Figs. 5.5, 5.6, and 5.7. Figures 5.5 and 5.7 are generated using constant enthalpy contours that range from enthalpy of the fusion solid, H_{sf} , to that of the fusion liquid, H_{lf} . For all of the cases studied, $L_f = 0.25 \text{ J} / \text{kg}$, $T_f = 0.0^\circ \text{C}$ and the thermal diffusivity and specific heats are set equal to unity.

The cases are:

1) Insulated sides, constant temperature on the base. The results are shown on the right half of Fig. 5.5 for $T_{Base} = 0.3^\circ \text{C}$.

2) Insulated sides, boundary condition of the third kind on the base. The results are shown on the left half of Fig. 5.5 for $T_\infty = 0.3^\circ \text{C}$, and a film coefficient $h = 10 \text{ W} / \text{m}^2 \cdot \text{K}$ on the base. As can be seen, the convection resistance creates a delay in thawing, depending on the magnitude of the film coefficient. As the film coefficient is enlarged, the expectation is for the so-called delay to vanish. The results should then converge to the constant temperature results. This experiment was conducted numerically and the expected results were obtained. Figure 5.6 shows this process by comparing the position of phase change interface, on the axis of symmetry, versus time for different film coefficients.

3) Constant temperature boundary condition, with $T = 0.3^{\circ} C$, on all outer surfaces of the cone. The phase change interface at different times is given in Fig. 5.7.

The results discussed in this chapter offer, in addition to an axisymmetric CE/SE phase change solver, a confirmation of the robustness of the numerical approach adopted.

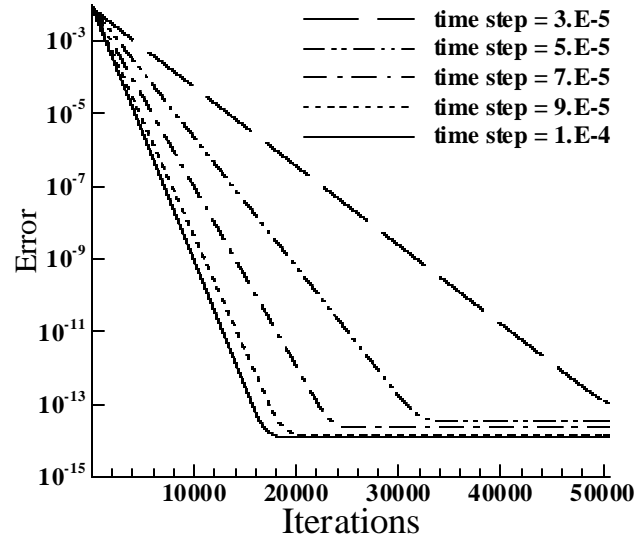


Figure 5.1: Vanishing errors for case 1

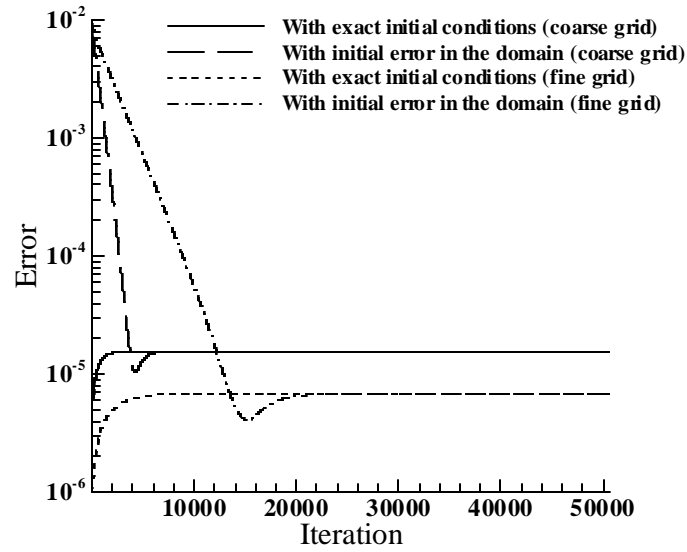


Figure 5.2: Grid size effects for case 2

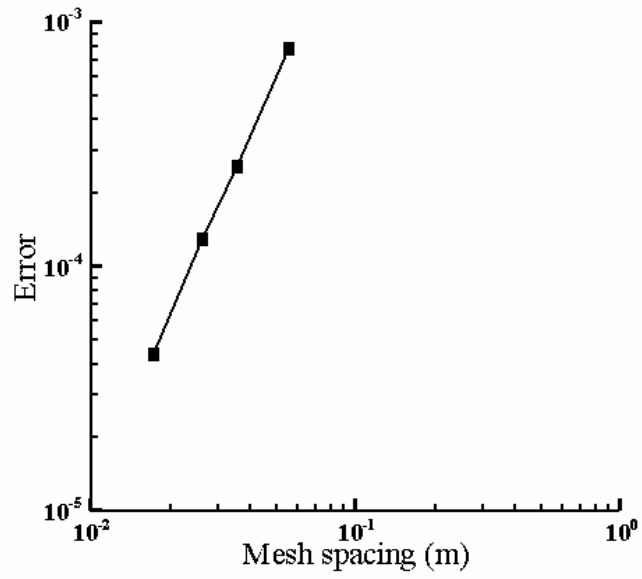


Figure 5.3: Demonstration of the axisymmetric CE/SE scheme's second-order accuracy

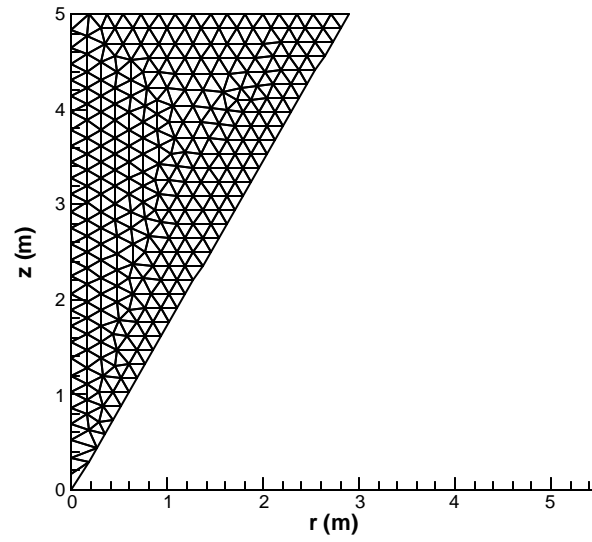


Figure 5.4: An example of the grid for conical cases

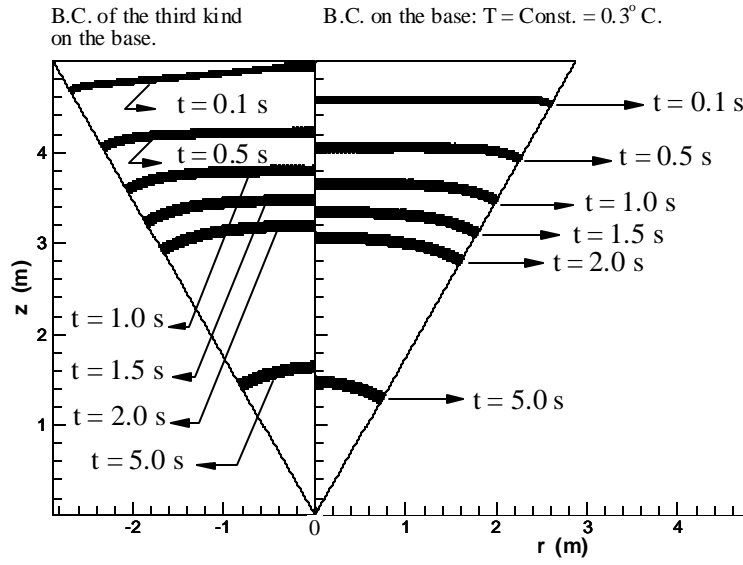


Figure 5.5: Position of the interface at different times, using enthalpy contours.

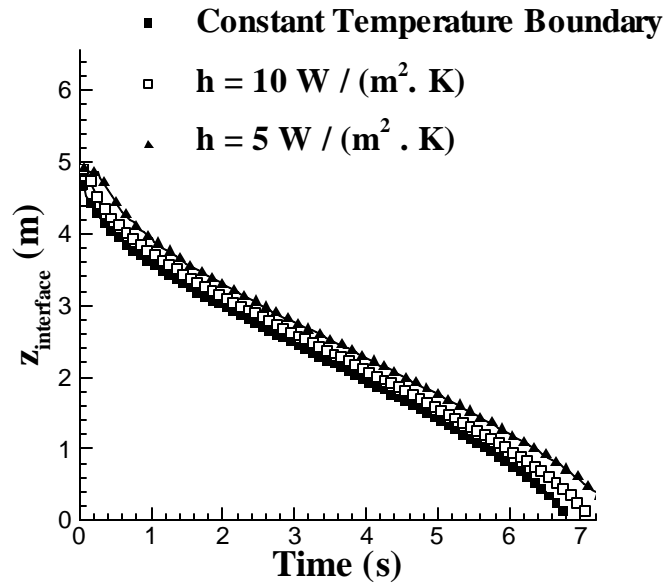


Figure 5.6: Position of the phase change interface on the axis of symmetry for the thawing cone case 2

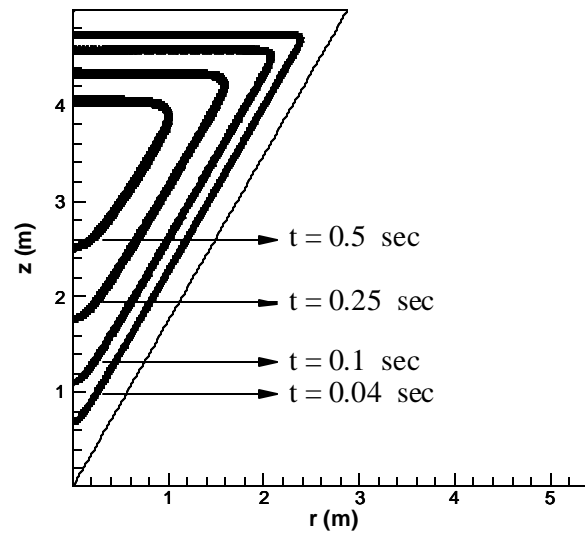


Figure 5.7: Interface position for the thawing cone case 3

Chapter 6

THREE-DIMENSIONAL CE/SE PHASE-CHANGE SCHEME

This chapter concerns the development of a three-dimensional CE/SE phase change solver. It contains a detailed derivation of the four-dimensional space-time scheme needed for solving phase change problems in three spatial dimensions. As presented in the previous chapters, the convergence and accuracy of the three-dimensional scheme is also assessed numerically, by comparing the results to the available analytical and semi-analytical solutions for specific benchmark problems.

6.1 Development of a Three-Dimensional CE/SE Scheme for Heat Conduction with Melting/Freezing

In three spatial dimensions, Eq. (2.3) becomes

$$\frac{\partial H}{\partial t} = \frac{\partial}{\partial x} \left(k \frac{\partial T}{\partial x} \right) + \frac{\partial}{\partial y} \left(k \frac{\partial T}{\partial y} \right) + \frac{\partial}{\partial z} \left(k \frac{\partial T}{\partial z} \right) \quad (6.1)$$

Equation (2.6) can be used without change. Define vector \vec{U} as

$$\vec{U} = (F, G, P, H) \quad (6.2)$$

where

$$F = -k \frac{\partial T}{\partial x}, \quad G = -k \frac{\partial T}{\partial y}, \quad P = -k \frac{\partial T}{\partial z} \quad (6.3)$$

and H is the enthalpy per unit volume.

Considering (x, y, z, t) as coordinates of a four-dimensional Euclidean space-time, Eq. (4.4) will still be valid. The spatial projection of the unstructured grid used here consists of tetrahedral elements. To provide a clear geometric description of the CE, an analogy with the two-dimensional formulation is helpful. As described in previous sections, the integrations involved in the two-dimensional case are performed on the CE 's top, bottom and lateral faces that are two-dimensional surfaces. Similarly, the integrations for the three-dimensional case are performed on the CE 's top, bottom and lateral 'faces' that are three-dimensional volumes.

6.1.1. Top/Bottom Faces

These faces are constant-time faces. Consider a tetrahedral element 'cell j ' at time level $n-1/2$, e. g., the tetrahedron $V_1 V_2 V_3 V_4$ depicted in Fig. 6.1. Let nodes V_1, V_2, V_3 , and V_4 represent vertices of cell j while its four neighboring cells are referred to as cells j_1, j_2, j_3 ,

and j_4 . The neighbors are named in a way that any vertex V_k , $k = 1, 2, 3$, and 4 , of cell j faces the side shared by cell j and its neighbor j_k . Further, let point C denote the centroid of cell j while C_k represents the centroid of the neighboring cell j_k . The three-dimensional analogue of the hexagon $V_1C_2V_3C_1V_2C_3$ of Fig. 4.1(a) can be visualized as follows. For each face of tetrahedral cell j , a hexahedron can be constructed using vertices of that face, the centroid of cell j , and the centroid of the corresponding neighbor. These hexahedra, i.e., $CV_2V_3V_4C_1$, $CV_1V_3V_4C_2$, $CV_1V_2V_4C_3$, and $CV_1V_2V_3C_4$, are three-dimensional analogues of the two-dimensional bottom faces $CV_2V_3C_1$, $CV_3V_1C_2$, and $CV_1V_2C_3$ depicted in Fig. 4.1(a). The hexahedron related to neighbor j_1 , i.e., $CV_2V_3V_4C_1$, is depicted in Fig. 6.1. The union of these 4 hexahedra is a polyhedron with 12 triangular faces. The centroid of this polyhedron is the solution point of cell j , and its spatial coordinates will be referred to as x'_j , y'_j , and z'_j . This polyhedron is the three-dimensional analogue of the bottom face of the hexagonal prism depicted in Fig. 4.1(a). A similar polyhedron represents the top face of the three-dimensional case's CE .

Adopting a notation convention similar to that introduced in [65], the volume of each of the four hexahedra introduced above will be referred to as $V^{(k)}$, $k = 1, 2, 3$, and 4 where $V^{(k)}$ is volume of the hexahedron related to neighbor j_k . Further, let coordinates of the centroid of the hexahedra be represented by $x_c^{(k)}$, $y_c^{(k)}$, and $z_c^{(k)}$ where $k = 1, 2, 3$, and 4 . The unit outward normals for top and bottom faces are $(0, 0, 0, 1)$ and $(0, 0, 0, -1)$, respectively.

6.1.2. Lateral Faces

These faces simply connect the top and bottom faces in the 4th dimension. Therefore, there are 3 lateral ‘faces’ (which are in fact three-dimensional volumes) associated with each neighbor. To visualize these faces, note that 3 lateral faces associated with neighbor j_1 are volumes $C_1V_2V_3C'_1V'_2V'_3$, $C_1V_3V_4C'_1V'_3V'_4$, and $C_1V_2V_4C'_1V'_2V'_4$ where the primed nodes refer to the same spatial position as the corresponding unprimed nodes, but at the new time level, n . The volume of these lateral faces will be referred to as $V^{(l,k)}$ where $l = 1, 2, 3$, and $k = 1, 2, 3, 4$ refers to the associated neighbor. The centroid of each lateral face is represented by the space-time point $(x_c^{(l,k)}, y_c^{(l,k)}, z_c^{(l,k)}, t^n - \Delta t/4)$. The unit outward normal of each lateral face is represented by $\hat{n}^{(l,k)} = (\hat{n}_x^{(l,k)}, \hat{n}_y^{(l,k)}, \hat{n}_z^{(l,k)}, 0)$. These unit normals are defined outward with respect to the hexahedra introduced in the previous section.

Analogous to the two-dimensional case, each lateral face represented by $V^{(l,k)}$, as well as each bottom face represented by $V(k)$, is associated with $SE(j_k, n-1/2)$, $k = 1, 2, 3, 4$. The top face is associated with $SE(j, n)$. Using the three-dimensional analogue of Eq. (4.5), i.e.,

$$\begin{aligned} \Psi(x, y, t; j, n) = & \Psi_j^n + (\Psi_x)_j^n (x - x'_j) + \\ & (\Psi_y)_j^n (y - y'_j) + (\Psi_z)_j^n (z - z'_j) + (\Psi_t)_j^n (t - t^n) \end{aligned} \quad (6.4)$$

where Ψ_j^n , $(\Psi_x)_j^n$, $(\Psi_y)_j^n$, $(\Psi_z)_j^n$, and $(\Psi_t)_j^n$ are constant coefficients associated with the solution point (x'_j, y'_j, z'_j, t^n) , and Ψ can be any of the components of \vec{U} . With integrations similar to the two-dimensional case, the three-dimensional analogue of Eq. (4.13) becomes

$$H_j^n = \sum_{k=1}^4 R^{(k)} / \sum_{k=1}^4 V^{(k)} \quad (6.5)$$

where

$$\begin{aligned} R^{(k)} = & V^{(k)} H(x_c^{(k)}, y_c^{(k)}, z_c^{(k)}, t^{n-1/2}; j_k, n-1/2) - \\ & \sum_{l=1}^3 \{ F(x_c^{(l,k)}, y_c^{(l,k)}, z_c^{(l,k)}, t^n - \Delta t/4; j_k, n-1/2) n_x^{(l,k)} + \\ & G(x_c^{(l,k)}, y_c^{(l,k)}, z_c^{(l,k)}, t^n - \Delta t/4; j_k, n-1/2) n_y^{(l,k)} + \\ & P(x_c^{(l,k)}, y_c^{(l,k)}, z_c^{(l,k)}, t^n - \Delta t/4; j_k, n-1/2) n_z^{(l,k)} \} V^{(l,k)} \end{aligned} \quad (6.6)$$

6.1.3. First-Order Derivatives

Using an approach similar to the two-dimensional case, the process of determining the first-order derivatives of the field parameters can be summarized in solving the following 4 linear systems, each having 3 equations and 3 unknowns.

$$\begin{aligned} (x'_{j_k} - x'_j) \Psi_x^{(1)} + (y'_{j_k} - y'_j) \Psi_y^{(1)} + \\ (z'_{j_k} - z'_j) \Psi_z^{(1)} = \Psi_{j_k}^n - \Psi_j^n, \quad k = 2, 3, 4 \end{aligned} \quad (6.7)$$

$$\begin{aligned} (x'_{j_k} - x'_j) \Psi_x^{(2)} + (y'_{j_k} - y'_j) \Psi_y^{(2)} + \\ (z'_{j_k} - z'_j) \Psi_z^{(2)} = \Psi_{j_k}^n - \Psi_j^n, \quad k = 1, 3, 4 \end{aligned} \quad (6.8)$$

$$\begin{aligned}
& (x'_{j_k} - x'_j)\Psi_x^{(3)} + (y'_{j_k} - y'_j)\Psi_y^{(3)} + \\
& (z'_{j_k} - z'_j)\Psi_z^{(3)} = \Psi_{j_k}^n - \Psi_j^n, \quad k = 1, 2, 4
\end{aligned} \tag{6.9}$$

$$\begin{aligned}
& (x'_{j_k} - x'_j)\Psi_x^{(4)} + (y'_{j_k} - y'_j)\Psi_y^{(4)} + \\
& (z'_{j_k} - z'_j)\Psi_z^{(4)} = \Psi_{j_k}^n - \Psi_j^n, \quad k = 1, 2, 3
\end{aligned} \tag{6.10}$$

The above systems can be solved for $\Psi_x^{(k)}$, $\Psi_y^{(k)}$ and $\Psi_z^{(k)}$, where $k = 1, 2, 3$, and 4 . A weighted average may then be used to calculate $(\Psi_x)_j^n$, $(\Psi_y)_j^n$ and $(\Psi_z)_j^n$ as follows

$$(\Psi_w)_j^n = \frac{\sum_{k=1}^3 |\mathbf{q}_m \mathbf{q}_q \mathbf{q}_r|^{\tilde{a}} (\Psi_w)_{O_k}^n}{\sum_{k=1}^3 |\mathbf{q}_m \mathbf{q}_q \mathbf{q}_r|^{\tilde{a}}} \tag{6.11}$$

where

$$\mathbf{q}_k = \sqrt{(\Psi_x^{(k)})^2 + (\Psi_y^{(k)})^2 + (\Psi_z^{(k)})^2}, \quad k = 1, 2, 3, 4 \tag{6.12}$$

and, for any given integer, $k = 1, 2, 3, 4$, $\{k\} \cup \{m, q, r\} = \{1, 2, 3, 4\}$. The subscript w in Eq. (6.11) can be x , y , or z while parameter Ψ represents either H or T . The constant \tilde{a} is usually set equal to 1. Note that, to avoid dividing by zero, in practice a small positive number such as 10^{-20} is added to the above denominators.

6.1.4. Second-Order Derivatives

Using an approach similar to the two-dimensional case, the process of determining the second-order derivatives can be summarized in solving the following 3 linear systems, each having 4 equations and 4 unknowns.

$$\begin{aligned} (x'_{jk} - x'_j)(T_{wx})_j^n + (y'_{jk} - y'_j)(T_{wy})_j^n + (z'_{jk} - z'_j)(T_{wz})_j^n \\ - \frac{\Delta t}{2}(T_{wt})_j^n = (T_w)_{jk}^{n-1/2} - (T_w)_j^n, \quad k=1,2,3,4 \end{aligned} \quad (6.13)$$

These may be solved simultaneously for second-order derivatives of temperature, i.e., $(T_{wx})_j^n$, $(T_{wy})_j^n$, $(T_{wz})_j^n$ and $(T_{wt})_j^n$ where subscript w can be x , y , or z . Using this technique, the mesh values of second-order derivatives of T can be evaluated and used in the solution procedure which is similar to that of the two-dimensional case.

6.1.5. Boundary Conditions

In order to treat the boundary conditions, a ghost cell is defined for each boundary cell. Geometrically, the ghost cell is the mirror image of the corresponding boundary cell with respect to the boundary. The three-dimensional case's reflecting boundary conditions are derived using a technique similar to that described in [87] for the two-dimensional case. As explained in section 4.1.3 and, in more detail in [87], reflecting boundary conditions can be easily defined in a boundary fitted coordinate system. However, a transformation (of a rotation nature) is then needed in order to describe the boundary conditions back in the original coordinate system of the problem. Appendix A is devoted to derivation of this

transformation matrix for an arbitrarily oriented insulated boundary, for a general three-dimensional problem.

Other, phase-change related details of both constant temperature and convective boundary conditions are as described in the previous chapters.

6.2 Numerical Results and Discussion

In order to validate the computer program for three-dimensional cases, and study the error behavior of the numerical scheme, the following two cases were designed and applied to a unit cube, for a fictitious material with unit conductivity.

Case 1. $H = T$ and $T = x + y + z + \text{const.}$ (6.14)

Case 2. $H = T$ and $T = x^2 + y^2 + z^2 + 6t$ (6.15)

As can be seen, the above temperature distributions satisfy the governing equation, Eq.(6.1). The following sections contain the details of the above cases, along with several other phase change problems.

Before starting the case studies, it is of value to mention the grid generation method that was applied. The unstructured grids used here, are generated employing the following three grid generators:

- 1) A regular tetrahedral grid generator, which uses cubic building blocks (each divided into a number of tetrahedra) and assembles them to construct the domain of interest, (see Appendix B for geometric details of these blocks),
- 2) An advancing front tetrahedral Delaunay grid generator [95],
- 3) A commercial grid generation code (GAMBIT).

6.2.1. Case 1: A Steady Linear Problem

This case is a steady first-order problem, for which it can be easily shown that the CE/SE formulation is exact, in the sense that no truncation error exists. Therefore, the spatial grid is not an issue in this case. On the other hand, the time-step issue needs to be studied. Equation (6.14) was applied on the boundaries, with an initially imposed error distribution over the entire domain. The results confirmed that, after a period of time, the temperature converges to the accurate distribution everywhere in the field. Figure 6.2 shows the absolute error (which is defined as the infinity norm of the difference between the numerical and exact solutions) versus the iterations for different time steps. As may be observed the errors vanish to the order of machine zero.

Using this case, the error behavior was studied, for different time-steps. Since the present method is explicit, there are stability restrictions on the time-step. The error behavior for the three-dimensional case was observed to be similar to that obtained for the two-dimensional analysis, discussed in detail in Chapter 4.

6.2.2. Case 2: A Problem with Time-Dependent Boundary Conditions

For this transient problem (see Eq. (6.15)), unlike the previous case, there is a mesh-dependent error associated with second-order accuracy of the CE/SE method. Clearly, this error should decrease by using finer spatial grids. Different spatial grids were used for this case. A grid that has 9 nodes on each edge of the unit cube will be referred to as the coarse grid, while the so-called medium grid consists of 21 nodes on each edge of the unit cube. The grid referred to as fine grid contains 31 nodes on each edge of the unit cube. Equation (6.15) was applied on the boundaries. Both exact solution and a uniform error distribution were used as initial conditions. The absolute average errors (defined as the arithmetic average of the absolute value of the difference between the numerical and exact solutions, over the entire domain) are shown in Fig. 6.3.

In Fig. 6.4, the absolute average errors are plotted versus the spatial mesh spacing for different grids. This figure presents a visual demonstration of the second-order accuracy of the three-dimensional scheme.

6.2.3. Case 3: Freezing of a Finite Slab

Consider the freezing slab problem discussed in Chapter 4. In order to model this one-dimensional problem using the three-dimensional code, all sides of the unit cube are assumed to be insulated, except one side, (plane $y = 0$), which acts like the $x = 0$ wall of the problem stated in Chapter 4.

This problem is studied for $S_t = 4$ where $S_t = c_s(T_f - T_w)/L_f$ is the Stefan number. Other parameters are $T_w = -1.0^\circ C$, $T_f = 0.0^\circ C$, while the thermal diffusivity and specific heats are set equal to unity. An example of the spatial mesh for the unit cube is given in Fig. 6.5. Figure 6.6 shows the position of the phase-change interface compared to the analytical solution versus time. The temperature distribution in the y direction at time $t = 0.14$ s are compared to the analytical solution in Fig. 6.7. No changes occur in either x or z directions. As can be seen, accurate results are obtained.

This case is also solved using another commonly used fixed domain scheme from [86]. This method (usually called the source based method), is constructed based on an alternation of the enthalpy formulation. The basis of the method can be described in simple terms as follows. Assume, (for a constant density), that the enthalpy per unit volume, H , is a function of both temperature and the liquid fraction, i.e., $H \equiv H(T, \mathbf{f})$ instead of temperature only [96]. The chain rule can then be used to get

$$\frac{\partial H}{\partial t} = \frac{\partial H}{\partial T} \frac{\partial T}{\partial t} + \frac{\partial H}{\partial \mathbf{f}} \frac{\partial \mathbf{f}}{\partial t} \quad (6.16)$$

where $\frac{1}{\rho} \frac{\partial H}{\partial T} \equiv c$ can be regarded as the specific heat of the material, and $\frac{1}{\rho} \frac{\partial H}{\partial \mathbf{f}} \equiv L_f$ as the latent heat of phase transformation. Then by substituting Eq. (6.16) into Eq. (6.1), a new formulation results as follows

$$\mathbf{r} \left(c \frac{\partial T}{\partial t} + L_f \frac{\partial \mathbf{f}}{\partial t} \right) = \frac{\partial}{\partial x} \left(k \frac{\partial T}{\partial x} \right) + \frac{\partial}{\partial y} \left(k \frac{\partial T}{\partial y} \right) + \frac{\partial}{\partial z} \left(k \frac{\partial T}{\partial z} \right) \quad (6.17)$$

This formulation is called *source based* because the term involving the time derivative of the liquid fraction, is usually treated as a source term. Although the above formulation is written conveniently in terms of the temperature, there is a drawback associated with it: the liquid fraction is also unknown along with the temperature. Therefore iterative corrections are needed in order to resolve both temperature and the liquid fraction fields. The above formulation is numerically treated in [86], using an implicit finite difference scheme with iterations in each step for correcting the liquid fraction field. This method is applied to the same freezing slab problem in order to compare the error distributions.

The error percentages within the domain are depicted in Fig. 6.8, for both the CE/SE method and the method of [86], using an identical time step and identical spatial grid spacing. As can be seen, the error associated with the CE/SE method is more uniform over the domain, compared with the method of [86]. The mean values and standard deviations associated with Fig. 6.8, are given in Table 6.1.

	CE/SE	Method of [86]
Mean Error (%)	0.000836	0.001275
Standard Deviation	0.000521	0.001227

Table 6.1: Statistical parameters associated with Fig. 6.8

6.2.4. Case 4: Thawing of a Cube

Consider a unit cube that is initially frozen at the fusion temperature T_f . At time $t = 0$, the temperature of all outer surfaces is raised to T_w and held there. This case is studied for $S_t = 4$, $T_w = 1.0^\circ C$, and $T_f = 0.0^\circ C$, while the thermal diffusivity and specific heats are set equal to unity. Figure 6.9(a) shows the frozen core of the cube at different times. These graphs are generated using a shaded view of the frozen cells in the mesh. Figure 6.9(b) shows the xy -view of the phase-change interface location at different times. The plots are generated using constant enthalpy contours ranging from H_{sf} to H_{Lf} . The top graph also contains the xy -view of the spatial mesh, from which the interface width is observed to be roughly equal to the size of one cell. This demonstrates the ability of the CE/SE method for capturing the discontinuities sharply.

6.2.5. Case 5: Thawing of an ellipsoid

Consider a prolate ellipsoid that is initially frozen at the fusion temperature T_f . At time $t = 0$, the temperature of its outer surface is raised to T_w and held there. This case is studied for $S_t = 1$, $T_w = 1.0^\circ C$, and $T_f = 0.0^\circ C$, while the thermal diffusivity and specific heats are set equal to unity. The geometry has a half major axis equal to 0.4 m and a half minor axis of 0.25 m. The frozen core is shown in Fig. 6.10(a) at different times. The top graph shows both the spatial mesh and the initial frozen ellipsoid.

By reducing the eccentricity of the original ellipse, the above case approaches the case of a thawing sphere, for which, approximations for the total melting time are available in [27]. It is worthwhile, therefore, to also study this limiting case of a thawing sphere.

6.2.6. Case 6: Thawing of a sphere

Consider a sphere that is initially frozen at the fusion temperature T_f . At time $t = 0$, the temperature of its outer surface is raised to T_w and held there. This case is studied for $S_t = 1, 2, 3$, and 4 . The thermal diffusivity and specific heats are set equal to unity while $T_w = 1.0^\circ C$, and $T_f = 0.0^\circ C$. The radius of the sphere is taken to be 0.25 m. The frozen core is represented in Fig. 6.10(b) at different times, for a case where $S_t = 4$. The top graph shows both the spatial mesh and the initial frozen sphere. The total melting times, as shown in Fig. 6.11, agree with the results from [27]. However, for the freezing slab case, the error associated with the approximate relations given in [27], is reported to be 5%, while the comparison of CE/SE results with the exact solution of that case shows a maximum error of about 1%. A similar relation between the errors can then be expected for the case of the thawing sphere.

In conclusion, this chapter offered the derivation and performance study of a three-dimensional CE/SE phase change solver. Specifically in comparison to another second order fixed-domain method, (see section 6.2.3 and Fig. 6.8), on the same grid, the CE/SE

results are slightly more accurate and provide a more uniform error distribution over the domain.

One noteworthy observation regarding the three-dimensional code, concerns its increased sensitivity to irregularities in the spatial grid, compared to the two-dimensional and axisymmetric versions. It is therefore imperative to keep the sliver element in the spatial grid to a minimum. This increased sensitivity is common among numerical schemes. An explanation for this behavior involves the error accumulation due to the increased number of calculations in a three-dimensional code, compared to the lower dimension versions.

In the next chapter, we will return to the one-dimensional version of the solver, developed in Chapter 3. We will study its dissipative/dispersive behavior in detail and offer a modification to it, regarding the limit of small Stefan numbers.

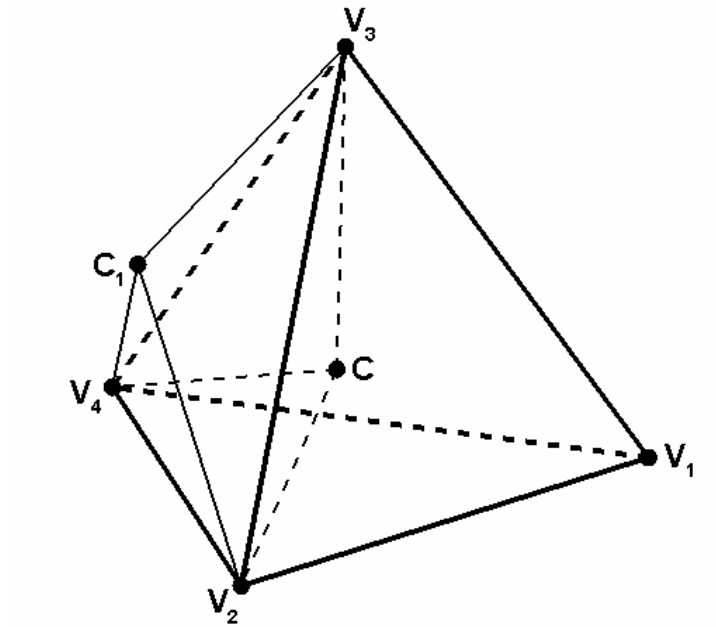


Figure 6.1: Geometry for 3D formulation

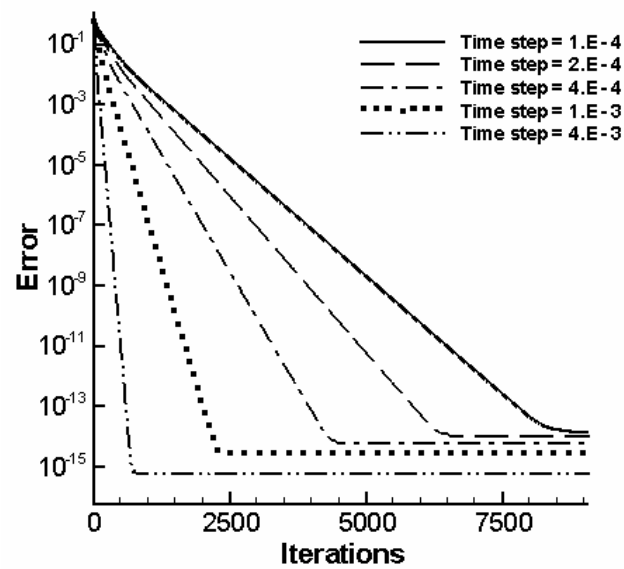


Figure 6.2: Vanishing errors for case 1

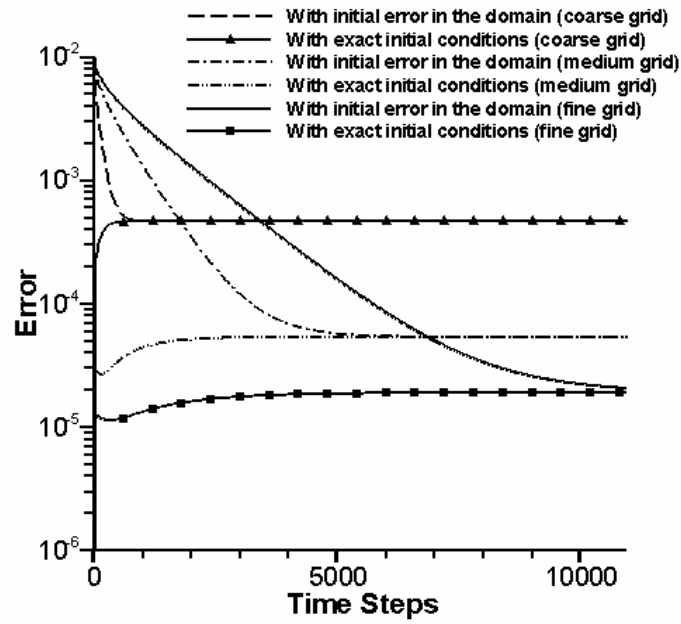


Figure 6.3: Grid size effects for case 2

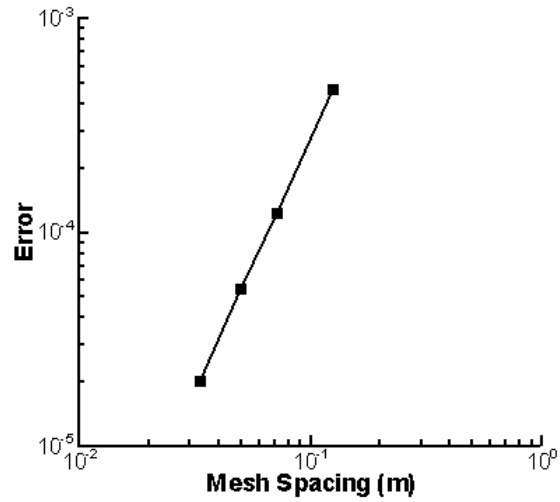


Figure 6.4: Demonstration of the CE/SE scheme's second-order accuracy

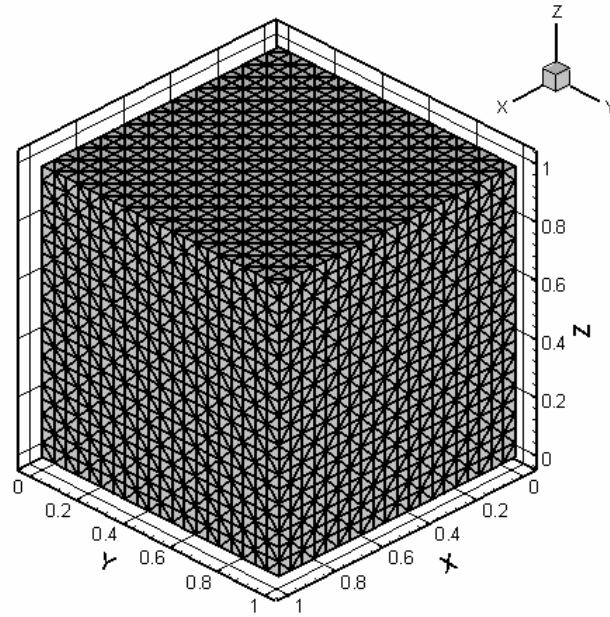


Figure 6.5: Spatial grid for the unit cube

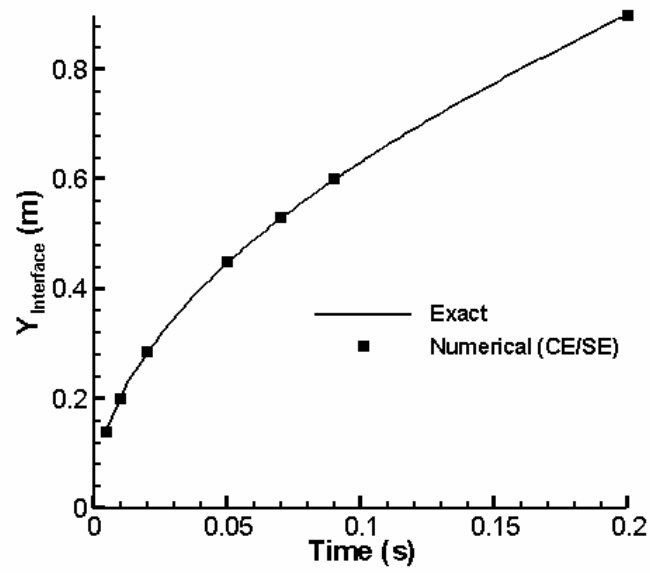


Figure 6.6: Location of the phase change interface for case 3

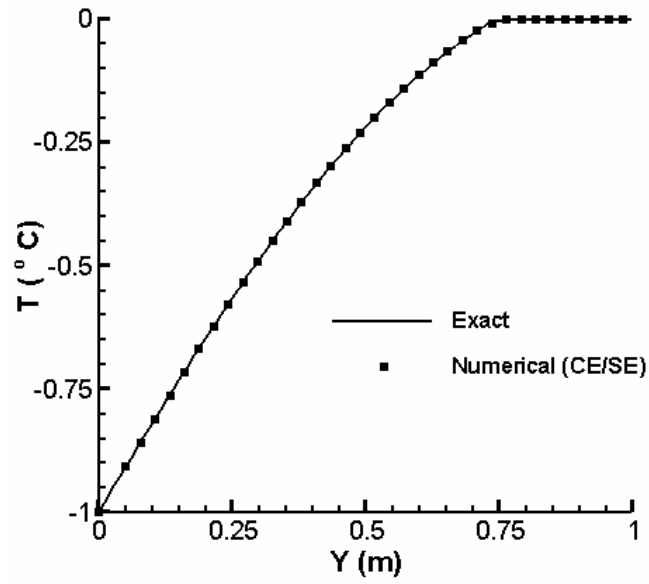


Figure 6.7: Temperature distribution at $t = 0.14 \text{ s}$ for case 3

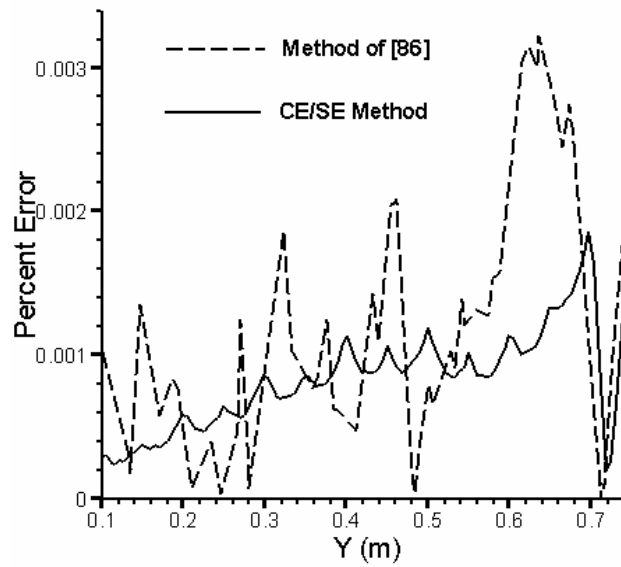


Figure 6.8: Comparison of the errors at $t = 0.14 \text{ s}$ for case 3

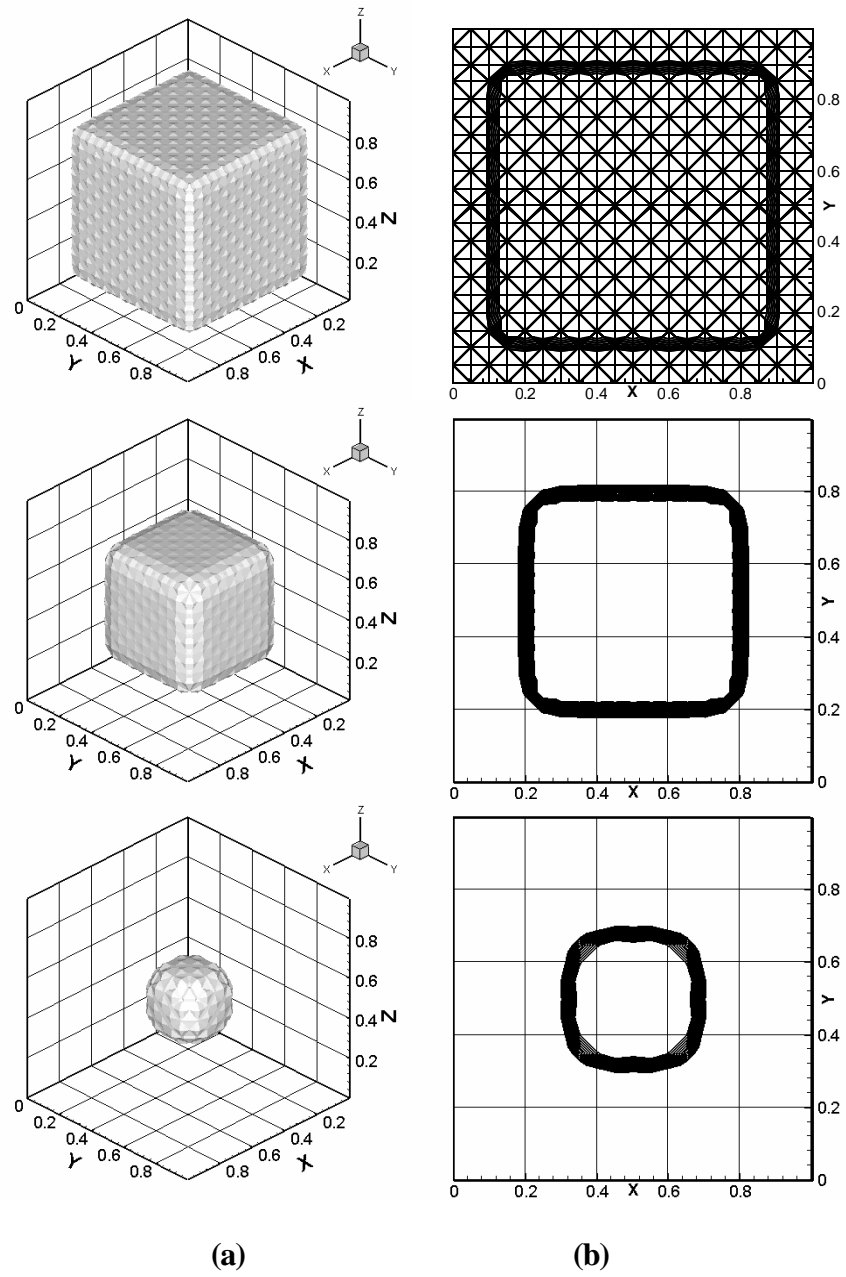


Figure 6.9: The thawing cube, (case 4), at $t = 0.005, 0.02$, and 0.05 s

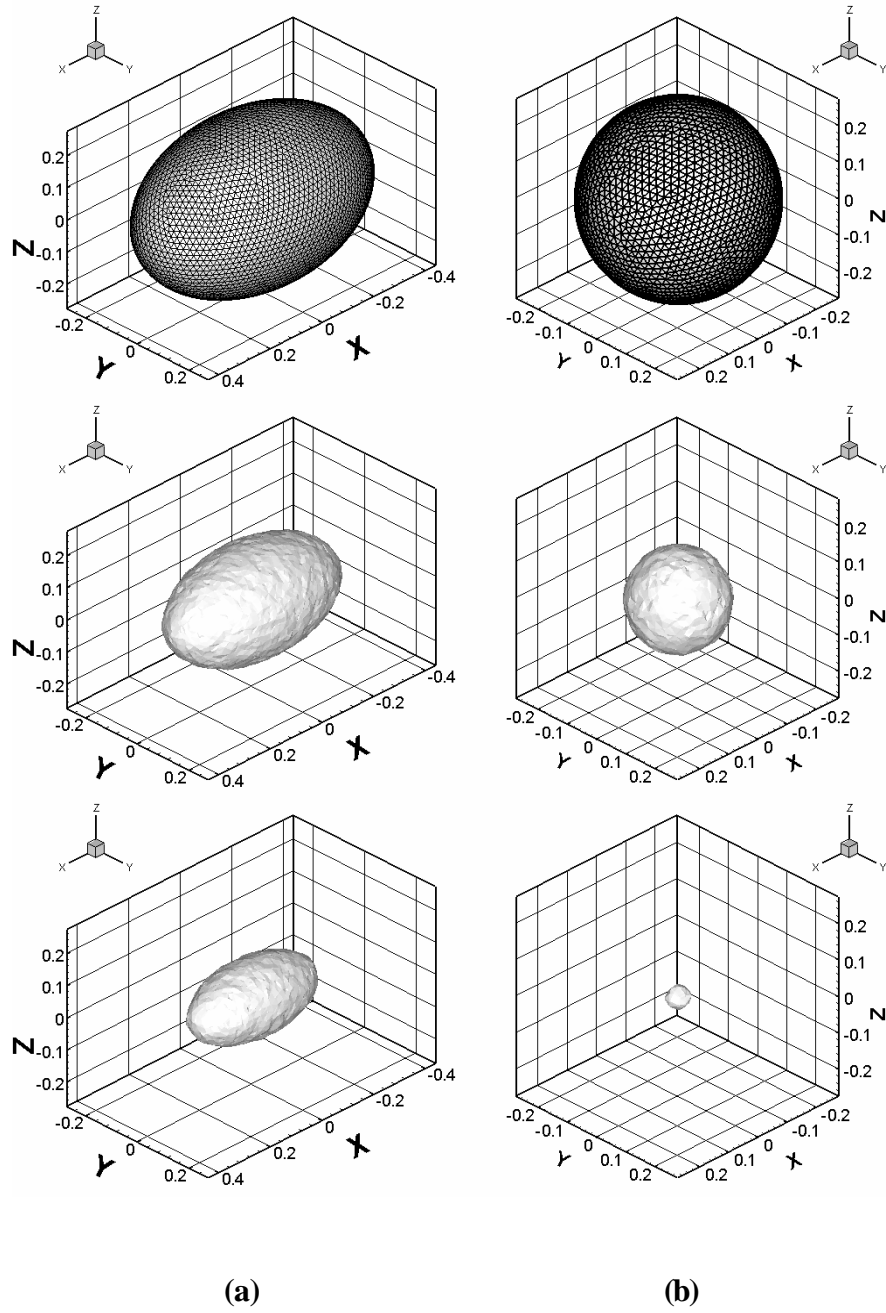


Figure 6.10: (a) Thawing ellipsoid, (case 5), at $t = 0, 0.0035,$ and 0.0085 s; (b) Thawing sphere, (case 6), at $t = 0, 0.0025,$ and 0.0065 s

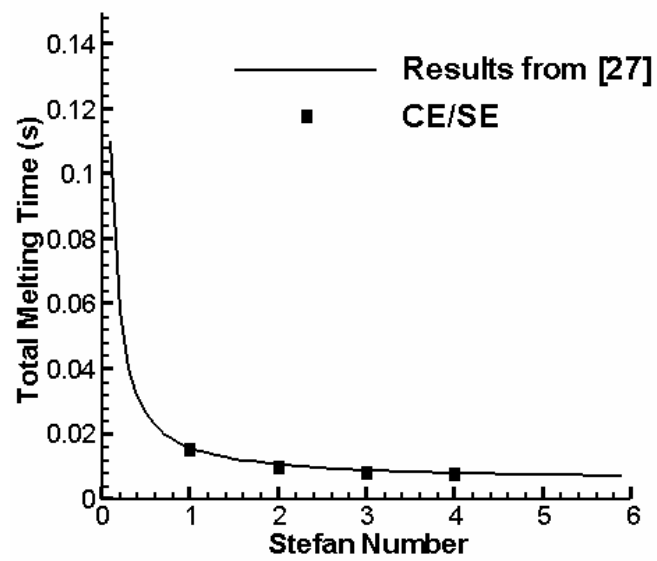


Figure 6.11: Total melting time for the thawing sphere of case 6

Chapter 7

THE STEFAN-NUMBER INSENSITIVE CE/SE PHASE-CHANGE SCHEME

The space-time CE/SE method was applied in the previous chapters to heat conduction problems with isothermal phase change, for one-dimensional, two-dimensional, axisymmetric and three-dimensional geometries. The results for several cases were compared to available analytical and semi-analytical solutions. The method's convergence and error behavior were also studied and it was found to be effective and accurate for these applications. No non-physical oscillations in the phase change interface were detected. Therefore, the SE/CE scheme was recognized as being able to resolve one of the weaknesses mentioned for the numerical simulations of the enthalpy method.

This chapter addresses the second difficulty associated with the enthalpy method, i.e. the limit of small Stefan numbers. It was shown, in Chapter 4, that numerical simulation of the Stefan problem using the CE/SE method is capable of providing accurate results for both large and small Stefan numbers. However, for small Stefan numbers, the accuracy had to be improved by using an alternate method for calculation of the first-order derivative terms.

The original CE/SE phase change scheme, like other numerical schemes for the enthalpy method, loses its accuracy and becomes dissipative for small Stefan numbers. The dissipation, nevertheless, is adjustable. The adjustment, that was employed in order to obtain accurate results for small Stefan numbers, is an *ad hoc* feature and therefore undesirable. Recently, space-time CE/SE methods have been designed for solving fluid flow problems without being sensitive to the size of the Courant number ([80], [29]). Using an analogous concept, it is possible to design a CE/SE scheme that is, to a considerable degree, insensitive to the size of the Stefan number.

In this chapter, the problem formulation using the enthalpy method and the original CE/SE method applied to it, for one-dimensional geometries are summoned from Chapter 3. The dissipation of the original method is then studied through numerical experiments and is found to vary with the Stefan number in a way that the accuracy reduces for small Stefan numbers. The new insensitive CE/SE scheme is then described for numerical simulation of phase change problems. A single-phase Stefan problem is selected as a benchmark problem for comparing the behavior of the original and the new scheme. Finally, the convergence and accuracy of the new scheme is assessed without any case-dependent adjustment.

7.1 The Original One-Dimensional Scheme

As developed in Chapter 3, the space-time CE/SE phase change scheme can be written as

$$H_j^n = \frac{1}{2} \left\{ H_{j-1/2}^{n-1/2} + H_{j+1/2}^{n-1/2} + \frac{\Delta x}{4} \left[(H_x)_{j-1/2}^{n-1/2} - (H_x)_{j+1/2}^{n-1/2} \right] \right\} \\ - \frac{\Delta t}{2 \Delta x} \left\{ F_{j+1/2}^{n-1/2} - F_{j-1/2}^{n-1/2} + \frac{\Delta t}{4} \left[(F_t)_{j+1/2}^{n-1/2} - (F_t)_{j-1/2}^{n-1/2} \right] \right\} \quad (7.1)$$

where the second-order derivatives, required for calculation of F_t are determined as described in Section 3.1.2. The first-order derivatives are calculated from

$$(\Psi_x)_j^n = (\Psi_x^+)_j^n W^+ + (\Psi_x^-)_j^n W^- \quad (7.2)$$

with

$$W^\pm = \frac{\left[(\Psi_x^\mp)_j^n \right]^{\tilde{a}}}{\left[(\Psi_x^-)_j^n \right]^{\tilde{a}} + \left[(\Psi_x^+)_j^n \right]^{\tilde{a}}} \quad (7.3)$$

and

$$(\Psi_x^-)_j^n = \frac{\Psi_j^n - \Psi_{j-1/2}^n}{\Delta x/2}, \quad (\Psi_x^+)_j^n = \frac{\Psi_{j+1/2}^n - \Psi_j^n}{\Delta x/2} \quad (7.4)$$

Note that, to avoid dividing by zero, in practice a small positive number such as 10^{-20} is added to the denominator in Eq. (7.3). The parameter Ψ , in the above relations, can be either H or T . The value of \tilde{a} is usually set equal to 1. As mentioned in [69], the above weighted average provides the necessary numerical damping. In other words, \tilde{a} can be

regarded as an adjustable dissipation parameter. It was by adjusting this parameter that accurate results were obtained for the cases with small Stefan numbers in Chapter 4. The *ad hoc* nature of this feature is undesirable. The new CE/SE scheme introduced in the following sections is designed to overcome this difficulty. Before introducing the new scheme, however, it is of value to study the dissipation of the above scheme, and, in particular, its variation with the Stefan number.

7.2 The Dissipative / Dispersive Behavior of the Numerical Scheme

Numerical results of Chapter 4 show that, when the Stefan number is small, in order to sharply capture the discontinuities, the value of $\tilde{\alpha}$, (see Eq. (7.3)), needs be adjusted. Experiments conducted in Chapter 4 also confirmed that the dissipation of the schemes reduces by reducing $\tilde{\alpha}$. The dispersive behavior, however, increases by reducing $\tilde{\alpha}$. At the limit $\tilde{\alpha} = 0$, the resultant scheme is purely dispersive, if second-order derivatives are excluded.

Since the schemes with $\tilde{\alpha} = 0$ are linear, their behavior can be studied analytically. Two versions of the schemes with $\tilde{\alpha} = 0$ were studied in sections 3.3.1 and 3.3.2. Their dispersive behavior is manifest in Figs. 3.3-3.8, through the presence of negative amplification factors. Figures 3.3-3.5 represent the behavior of the linear scheme without second-order derivatives. The pure dispersive behavior is deduced because the amplification factor covers the entire range of $[-1, 1]$. Further, it was shown that reduction

of the Stefan number has a destabilizing effect. This destabilization, however, is ,by no means, sever enough to stall the program at the limit of small Stefan numbers. Stable results can still be easily obtained. Accuracy, on the other hand, is reduced by the oscillations that appear close to the discontinuities, and that are caused by the dispersive behavior.

The non-linear schemes, having $\tilde{\alpha} = 1$, do not show the above-mentioned oscillations. Their accuracy at the limit of small Stefan numbers, however, is reduced due to another factor: increased dissipation. To show this numerically, the original phase change scheme of Section 7.1 is applied to the benchmark phase change problem of Section 3.4.2, for Stefan numbers ranging from 0.01 to 10. The solution to this problem contains a discontinuity in the enthalpy field. A space-time grid was selected which provided stability for the range of interest. The width of the discontinuity was then measured. For the selected space-time grid, for $S_t = 10$, the discontinuity was captured very sharply, over a length slightly larger than the width of one cell. By reducing the Stefan number, the discontinuity became smeared. For example, for $S_t = 0.01$, the discontinuity is spread over more than 7 cells. These results are shown in Fig. 7.1. Two facts can be deduced from this figure:

- For Stefan numbers close to, and larger than, 1, the dissipation of the method is very low. This leads to accurate capturing of moving discontinuities.⁷

⁷ There is a dissipation term that automatically acts only in the neighborhood of the discontinuities and serves as a means of suppressing non-physical oscillations without affecting the solution at the smooth regions [80].

- For smaller Stefan numbers, the method manifests dissipation and the dissipation increases by reducing the S_t . Furthermore, the rate of increase of the dissipation also increases by reducing the Stefan number.

The objective is then to design a CE/SE method which is less sensitive to the value of S_t than the original scheme (with $\tilde{a} = 1$), and which also avoids the dispersive behavior of the scheme with $\tilde{a} = 0$.

7.3 A New CE/SE Phase Change Scheme

Recently a new generation of CE/SE schemes was introduced ([80], [81]). These schemes provide, for the Euler equations, CE/SE solvers that are insensitive to the local value of the Courant number in the flow field. A new CE/SE phase change scheme may be designed by adopting the same concept. The methodology, however, differs in some aspects in order to accommodate the physics of phase change problems.

It is worthwhile to emphasize that the new and the original CE/SE phase change schemes differ only in the calculation of the first-order derivatives, namely in Eqs.(7.2-7.4). As introduced in [81], define points M^+ , M^- , P^+ , and P^- as indicated in Fig. 7.2. It is through the variable parameter, $0 \leq t \leq 1$, that the automatic adjustment will occur in the new method's dissipation. Using points P^+ and P^- instead of points D and F, respectively, a new version of Eqs.(7.2-7.4) can be written as

$$(\Psi_x)_j^n = (\hat{\Psi}_x^+)_j^n \hat{W}^+ + (\hat{\Psi}_x^-)_j^n \hat{W}^- \quad (7.5)$$

with

$$\hat{W}^{\pm} = \frac{\left[\left(\hat{\Psi}_x^{\mp} \right)_j^n \right]^{\tilde{a}}}{\left[\left(\hat{\Psi}_x^{-} \right)_j^n \right]^{\tilde{a}} + \left[\left(\hat{\Psi}_x^{+} \right)_j^n \right]^{\tilde{a}}} \quad (7.6)$$

and

$$\left(\hat{\Psi}_x^{-} \right)_j^n = \frac{\Psi_j^n - \Psi_{P^{-}}^n}{(1+t)\Delta x/4}, \quad \left(\hat{\Psi}_x^{+} \right)_j^n = \frac{\Psi_{P^{+}}^n - \Psi_j^n}{(1+t)\Delta x/4} \quad (7.7)$$

In order to calculate $\Psi_{P^{-}}^n$ and $\Psi_{P^{+}}^n$, first-order Taylor series are used around the expansion points of A and C, respectively. In a similar way to that mentioned in [81] for the advection equation, it can be shown that, for $t = 1$, this scheme becomes equivalent to the original phase change scheme, i.e., Eqs.(7.2-7.4) with $\tilde{a} = 1$. On the other hand, for $t = 0$, it becomes equivalent to the scheme composed of Eqs.(7.2-7.4) with $\tilde{a} = 0$, which produces undesirable dispersive behavior. To overcome this problem, another scheme was suggested in [81], which was composed by combining the original and the above schemes as follows

$$\left(\Psi_x \right)_j^n = \left(\hat{\Psi}_x^{+} \right)_j^n W^{+} + \left(\hat{\Psi}_x^{-} \right)_j^n W^{-} \quad (7.8)$$

with W^{\pm} from Eq.(7.3) and $\left(\hat{\Psi}_x^{\pm} \right)_j^n$ from Eq.(7.7).

The parameter $0 \leq t \leq 1$ needs to be defined in a proper way that accounts for the physics involved. Consider the following parameter (in practice, a very small positive number is added to the denominator in order to avoid dividing by zero)

$$z = \frac{\Delta x}{\left| H_{j+1/2}^n - H_{j-1/2}^n \right|} \quad (7.9)$$

The parameter z is related to the inverse of an approximation of the spatial derivative of the enthalpy field. By considering a reference state where the value of $\left| H_{j+1/2}^n - H_{j-1/2}^n \right|$ equals the value of Δx , a reference z , (z_{ref}), can be defined that has the value of 1. This reference z can then be used in order to non-dimensionalize z as

$$z^* = \frac{z}{z_{ref}} \quad (7.10)$$

Dropping the * superscript, the parameter t is defined as

$$t = \begin{cases} z, & z \leq 1 \\ 1, & z > 1 \end{cases} \quad (7.11)$$

One feature of the above definition is that the small values of t occur closer to the phase change interface. Further, the larger the latent heat of fusion of the phase change material, the smaller the minimum value of t will be. Therefore, for moderate temperature

gradients, the largest deviation from the original CE/SE phase change scheme occurs for the small Stefan numbers and close to the phase front.

The scheme based on Eq.(7.8) was programmed using the above definition for \mathbf{t} . Although the corresponding Euler scheme was shown to be highly accurate [81], the resulting phase change scheme still suffered from unwanted oscillations. Another modification was then made in the definition of \mathbf{t} . This time a lower limit was also set for it

$$\mathbf{t} = \begin{cases} C_1, & \mathbf{z} \leq C_2 \\ \mathbf{z}, & C_2 \leq \mathbf{z} \leq 1 \\ 1, & \mathbf{z} > 1 \end{cases} \quad (7.12)$$

where C_1 and C_2 , are arbitrary parameters to be defined. Numerical experiments were used in order to set suitable, case-independent values for these parameters. A highly accurate non-oscillatory scheme resulted by setting the values of C_1 and C_2 in Eq.(7.12) equal to the Stefan number itself, i.e., for $S_t < 1$

$$\mathbf{t} = \begin{cases} S_t, & \mathbf{z} \leq S_t \\ \mathbf{z}, & S_t \leq \mathbf{z} \leq 1 \\ 1, & \mathbf{z} > 1 \end{cases} \quad (7.13)$$

Therefore, the new CE/SE phase change scheme is constructed using Eq. (7.1) with the first-order derivatives calculated from Eq.(7.8), and with \mathbf{t} calculated from Eqs.(7.9) and

(7.10). Note that for $S_t \geq 1$, no deviation from the original scheme is needed therefore, $t = 1$.

In the following section, comparison is made over a range of Stefan numbers, between the original CE/SE phase change scheme, the new scheme, and yet another commonly used fixed domain scheme adopted from [86]⁸. The benchmark problem used for these comparisons is selected to be a single-phase Stefan problem, for which an analytical solution exists [92].

7.4 Numerical Results and Discussion

In order to compare the accuracy of the new modified scheme with that of the original scheme, a single-phase Stefan problem is used as a benchmark, under the following conditions.

Consider a slab of thickness $L = 1$ with the initial state assumed to be liquid at the fusion temperature T_f . At $t = 0$, the temperature of the surface at $x = 0$ drops to T_w and is maintained at that value. The surface at $x = L$ is effectively insulated. The analytical solution of this problem, containing the transient temperature distributions and the phase front location, was discussed in detail in section 4.2.3. This problem is studied numerically for Stefan numbers ranging from 0.01 to 10. The Stefan number is defined as $S_t = c_s (T_f - T_w) / L_f$ where c_s denotes the specific heat of the solid and L_f is the latent heat of fusion. All cases are modeled using a uniform spatial grid containing 1,100 nodes. Other

⁸ See section 6.2.3 for a description of this alternative method.

parameters are $T_w = -1.0^\circ C$, $T_f = 0.0^\circ C$, while the thermal diffusivity and specific heats are set equal to unity.

Some of the studied cases are shown in Fig. 7.3-7.6 in order to illustrate the conclusions that are drawn. Figures 7.3(a), 7.4(a), 7.5(a), and 7.6(a) demonstrate the temperature distribution at $t = 0.14$ s for various small Stefan numbers. As can be seen, the deviation of the results obtained by the original CE/SE phase change scheme, from the analytical solution, increases as the Stefan number is reduced. The modified CE/SE phase change scheme, however, retains its accuracy at small Stefan numbers. In fact it does not show a distinguishable sensitivity to the magnitude of the Stefan number. The same observation can be made from Figs. 7.3(b), 7.4(b), 7.5(b), and 7.6(b). These plots represent the corresponding enthalpy values. Again it is seen that as Stefan number is reduced, the original CE/SE phase change scheme shows a dissipated interface while the modified scheme consistently resolves the phase front sharply. Figures 7.3(a) and 7.4(a) also contain the results of another commonly used method (from [86]). This third method shows behavior similar to the original CE/SE scheme for $S_t = 0.01$. However, comparing Figs. 7.3(a) and 7.4(a), it is observed that by increasing the Stefan number, the error associated with the original CE/SE scheme, vanishes at a higher rate compared to that of the method of [86]. Furthermore, the original CE/SE phase change scheme consumes less computational resources, resulting in a much faster scheme.

It is also observed that, for these cases, the original and the modified CE/SE schemes are both identically accurate for $S_t > 0.5$. For $S_t > 1.0$, as concluded from the formulations, the two schemes become theoretically identical.

The evolution of the interface location in time, obtained by the modified scheme, was also compared to the analytical solutions, for $S_t = 0.01$ and $S_t = 0.05$. This comparison is shown in Fig.7.7.

The computational cost imposed on the CE/SE scheme by the modification, although significant in one spatial dimension, will not be a factor in two- and three-dimensional simulations. This is due to the fact that, while the main body of calculations increases significantly by adding more dimensions, the extra computations needed for the modification remain of the same order.

Before concluding this chapter, it is worthwhile to mention that the modified scheme is easy to extend to higher dimensions.

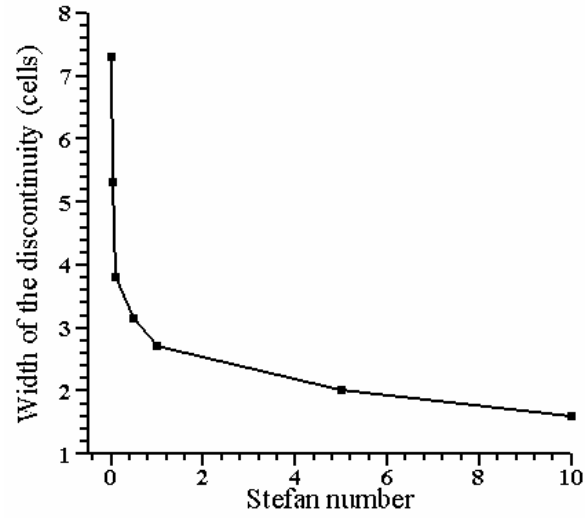


Figure 7.1: Effect of the Stefan number on the dissipation of the original phase change scheme

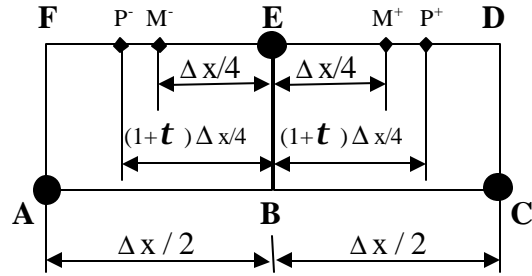


Figure 7.2: Geometry for the modified scheme

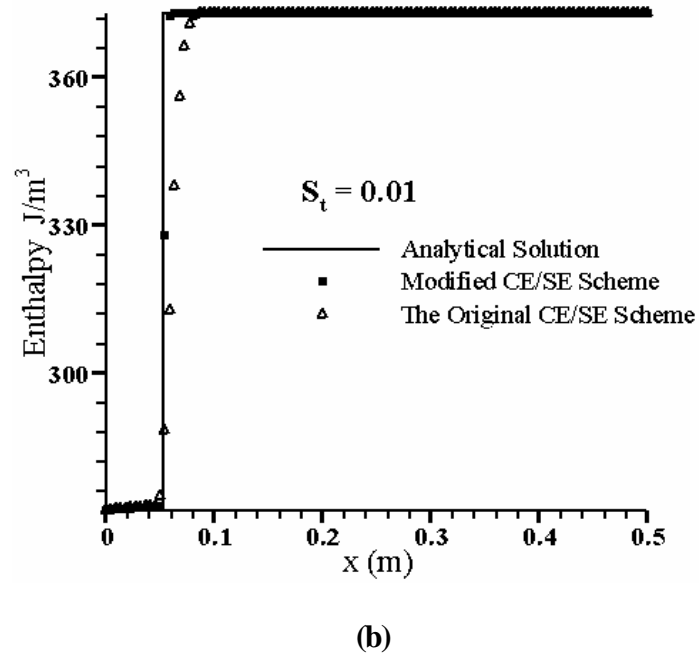
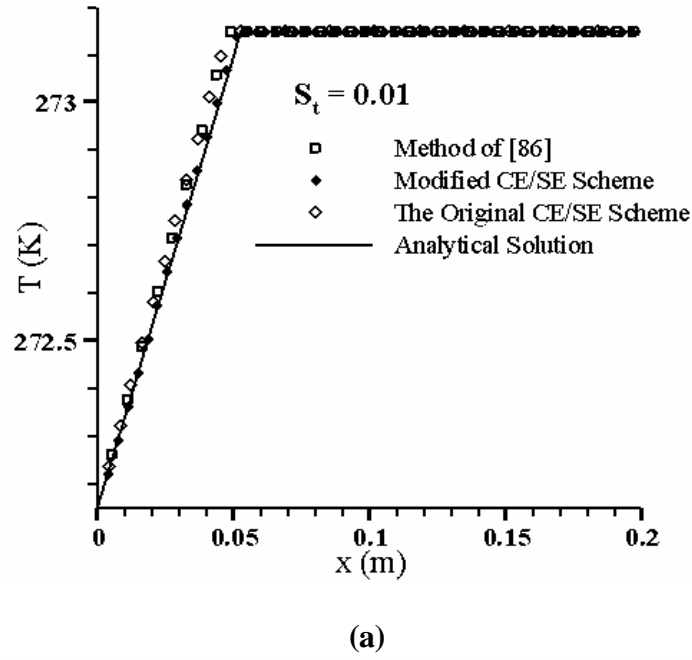


Figure 7.3: Temperature and enthalpy distributions at $t = 0.14$ s, for $St = 0.01$

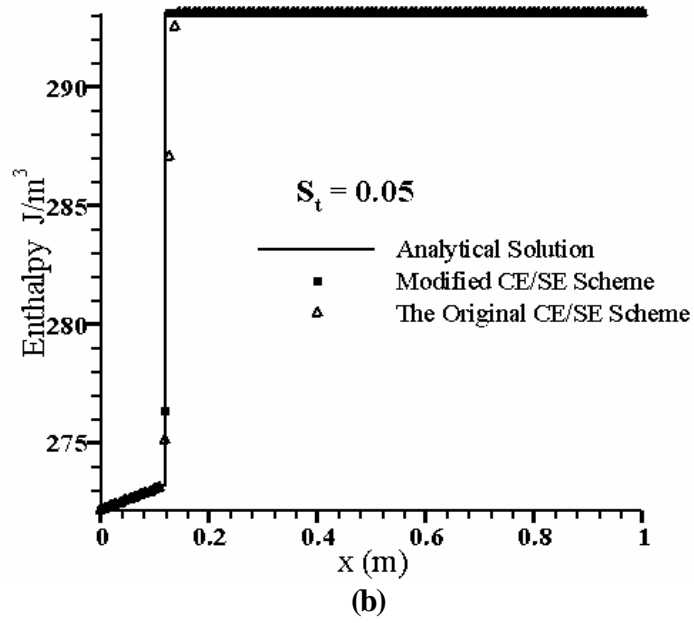
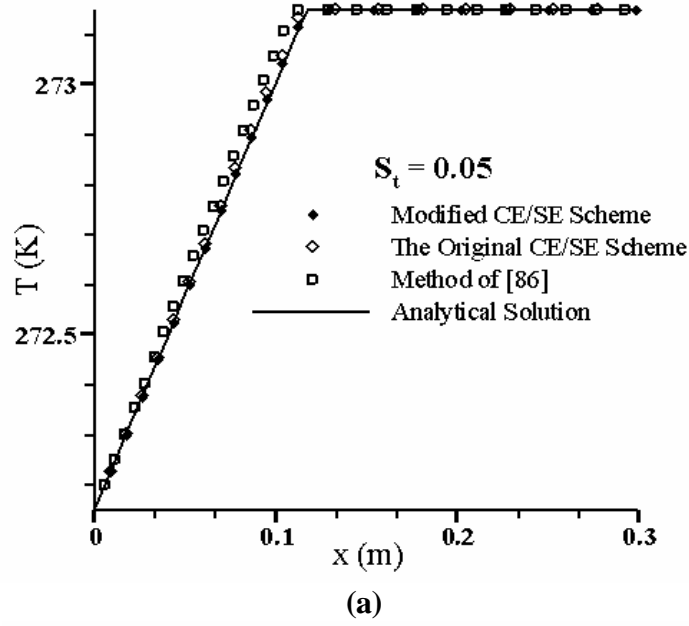


Figure 7.4: Temperature and enthalpy distributions at $t = 0.14$ s, for $St = 0.05$

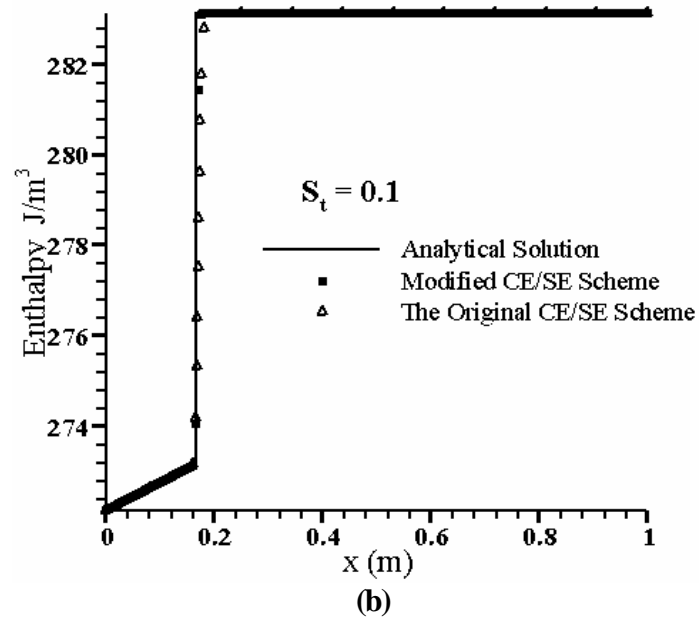
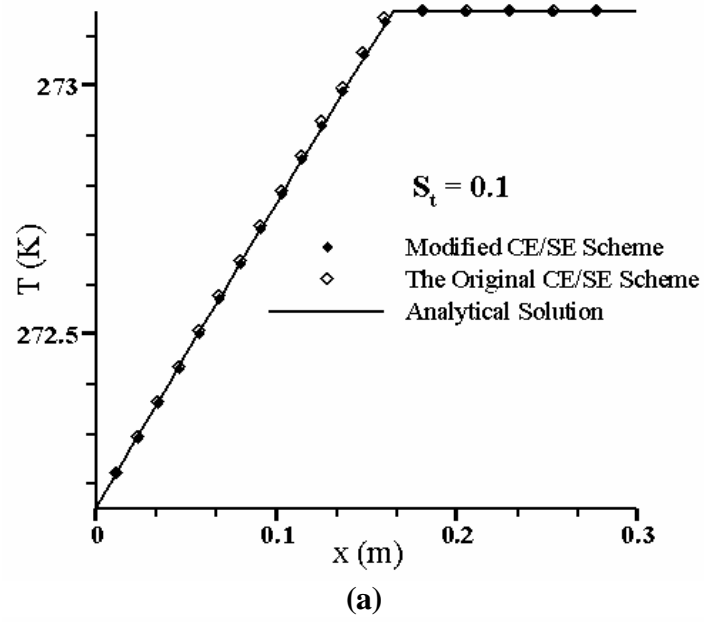


Figure 7.5: Temperature and enthalpy distributions at $t = 0.14$ s, for $St = 0.1$

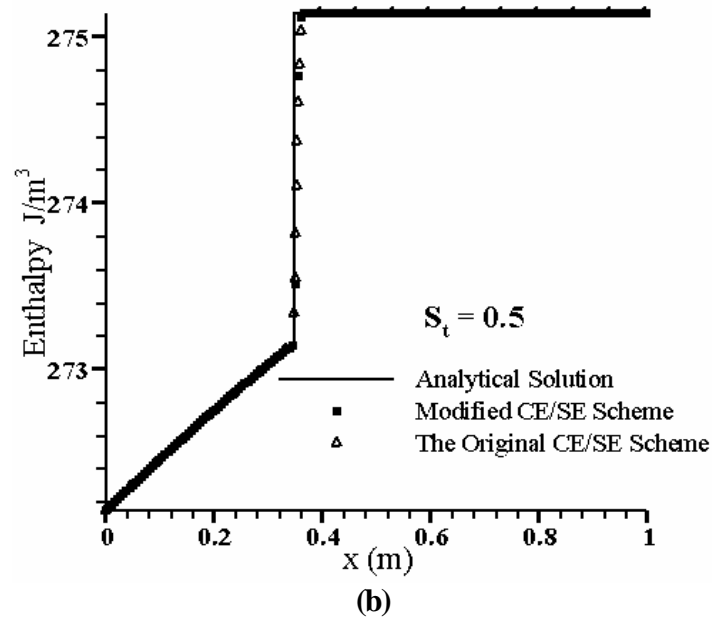
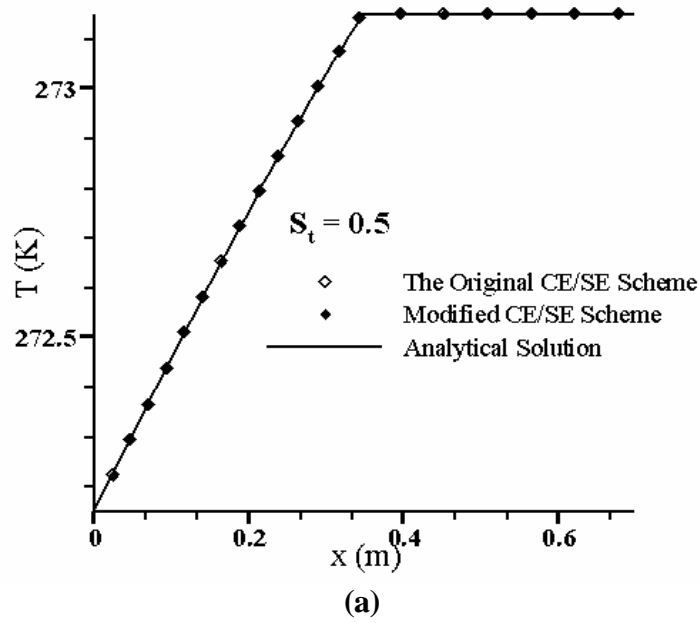


Figure 7.6: Temperature and enthalpy distributions at $t = 0.14$ s, for $St = 0.5$

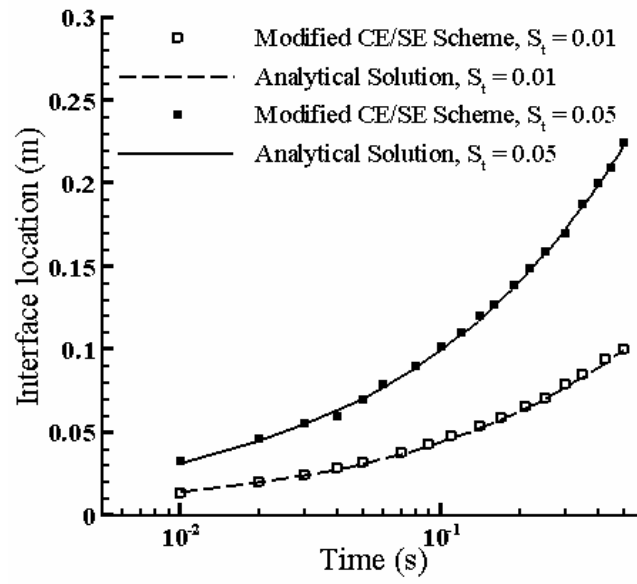


Figure 7.7: Location of the phase interface at different times

Chapter 8

A SPACE-TIME CE/SE NAVIER-STOKES SOLVER

This chapter provides a starting point for the future work towards construction of a general phase change solver based on the previous chapters. In this chapter, the “no convection-no density change” assumption made in the physical modeling of the problem is relaxed. A full CE/SE Navier-Stokes solver is derived, in which, a new procedure is explored for the treatment of the viscous terms. The program is validated for some standard benchmark fluid flow problems, and proved accurate and ready to be extended to include phase change phenomenon.

Both natural convection and density change have effects on the shape and speed of the phase interface. From a physical standpoint, discussion on the kinematics of the freezing and melting with density change is given in [97]. This paper also includes considerations at the molecular level. Further, Reference [98] provides a helpful analysis on the scales of phase change in the presence of natural convection.

A front tracking formulation of the solid-liquid phase change, taking into account the effects of the convection in the melt is presented in [99]. In this paper, the change of

density due to phase transition is neglected. The melt is considered incompressible and the natural convection is modeled using the Boussinesq⁹ approximation. The mushy zone is treated as a liquid with very large viscosity. A finite volume method is used; however special numerical treatments were necessary to improve the stability.

Reference [100], presents a finite difference treatment of a one-dimensional phase change problem with density change, again formulated using the front tracking approach. In this paper, the density of the liquid phase, (modeled as incompressible), is assumed to be much greater than that of the solid. A somewhat non-realistic assumption that simplifies the problem by setting the velocity of the liquid phase equal to that of the moving interface.

Reference [101] treats the phase change problem accounting for both density change and convection effects. In this paper a front fixing formulation is used for two-dimensional geometries. The liquid is, however, assumed incompressible and the effect of convection is modeled through the Boussinesq approximation.

Another paper that also uses a front fixing phase change modeling is [102]. This paper, although only applicable for a special one-dimensional case, provides an analytical study on the effects of both convection and density change. A literature review on the subject is also available in this paper.

A one-dimensional enthalpy formulation of the phase change problem with density change is available in [103]. This paper provides a single-domain formulation in which, the solid phase is modeled as a liquid with infinite viscosity. The change of density is modeled,

⁹ The Boussinesq approximation is based on neglecting the change of density in a fluid, everywhere except in the buoyancy term.

in this paper, using sources/sinks on the interface. The convection effects, however, are neglected using a low gravity assumption.

There are other references, such as [104], [105], [106], which deal with the effect of convection on the solid/liquid phase change phenomenon, neglecting the density change. References [104] and [105] also contain some experimental results. Further experimental results concerning melting of ice spheres, under forced and mixed convection, are found in [107]. Reference [108] provides extensive experimental results of convective solidification of gallium, and is considered as a benchmark for validation of numerical results.

Although we do not intend to provide, here, a thorough literature review on the subject, a brief survey reveals that many researchers have addressed the convection effects of the phase change problem, without density change. The density change effect, on the other hand, has received less attention, mainly due to the complexity of the subject. Very little literature is available concerning both effects. In the works that do consider both effects, other simplifying assumptions are used, reducing, to some degree, the generality of the approach.

In the search for a more general approach, a recent study, [109], is noteworthy. This paper, addresses a general multidimensional liquid-liquid transition of phase. The two liquids are considered to have different densities; further, one of the liquids is assumed stationary. This paper provides mathematical proof of the existence of a unique solution for the above problem, formulated using compressible fluids each expressed by an equation of state. Although no numerical implication is provided in this paper, because of its generality, this is the approach that we elect to follow here. The objective would then be to build a

general solver, based on a single-domain formulation, which expresses both solid and liquid phases. The generality of the approach may even allow, through the future work, to also add the gas phase to the system.

The choice of the numerical method is another important issue to address. As mentioned above, one difficult aspect of the problem of interest is the natural convection effects. A study of the literature on the numerical modeling of natural convection through a full Navier-Stokes formulation, (no phase change involved), reveals convergence difficulties related to low Mach number stiffness. Most of the compressible solvers used for this purpose, need low Mach number preconditioning to overcome this problem, see for example [110], [111].

A feature observed (see [112]) for the space-time CE/SE method, is that the method performs well through a wide range of Mach numbers, including low Mach numbers. Therefore, it is logical to expect that the CE/SE method could be an effective alternative for numerical simulation of natural convection too. If this hypothesis is validated through numerical experiments, it could limit the special treatments needed for pre-conditioning and stabilizing of present numerical methods used to simulate natural convection.

Few papers are available on the development of the CE/SE Navier-Stokes schemes. These papers, e.g., Refs. [112], [69], [66], [113], differ mainly in the method they use for treating the viscous terms. In this chapter, we use an approach for which the theoretical basis is discussed in [79]. The CE/SE method of this chapter, also differs from the above-mentioned references in the fact that, here, the gravity-related body force is treated as a source term.

The following sections explain in detail the development of this CE/SE Navier-Stokes solver, in two spatial dimensions. The three-dimensional extension would be straight forward. A standard benchmark problem, i.e., the driven cavity problem, is used to validate the computer program. This chapter will not cover validation cases including change of phase. The phase change related parameters and related details, however, are included in the program. As mentioned before, this chapter serves as a starting point for the continuation of the future work related to this research.

8.1 Governing Equations

As explained in the above introduction, compressible Navier-Stokes equations are used with a body force due to the gravity. In two spatial dimensions, these equations can be written in conservation form as follows (see, [90])

$$\frac{\partial \vec{U}}{\partial t} + \frac{\partial \vec{F}}{\partial x} + \frac{\partial \vec{G}}{\partial y} = \vec{S} \quad (8.1)$$

where \vec{U} , \vec{S} , \vec{F} , and \vec{G} are vectors given by

$$\vec{U} = \begin{bmatrix} \mathbf{r} \\ \mathbf{r}u \\ \mathbf{r}v \\ \mathbf{r}E \end{bmatrix}, \quad \vec{S} = \begin{bmatrix} 0 \\ 0 \\ -\mathbf{r}g \\ \dot{q} - \mathbf{r}g v \end{bmatrix},$$

$$\vec{F} = \begin{bmatrix} \mathbf{r} u \\ \mathbf{r} u^2 + p - \mathbf{t}_{xx} \\ \mathbf{r} u v - \mathbf{t}_{xy} \\ (\mathbf{r} E + p) u - u \mathbf{t}_{xx} - v \mathbf{t}_{xy} - k T_x \end{bmatrix}, \vec{G} = \begin{bmatrix} \mathbf{r} v \\ \mathbf{r} u v - \mathbf{t}_{xy} \\ \mathbf{r} v^2 + p - \mathbf{t}_{yy} \\ (\mathbf{r} E + p) v - u \mathbf{t}_{xy} - v \mathbf{t}_{yy} - k T_y \end{bmatrix}$$

where \mathbf{r} , u , v , and p represent density, horizontal component of velocity, vertical component of velocity, and pressure respectively. Total energy is denoted by E where

$$E = e + \frac{1}{2}(u^2 + v^2) \quad (8.2)$$

and e is the internal energy. Further, the shear stresses are calculated from

$$\mathbf{t}_{xx} = \frac{2}{3} \mathbf{m} (2u_x - v_y), \mathbf{t}_{xy} = \mathbf{m} (u_y + v_x) = \mathbf{t}_{yx}, \mathbf{t}_{yy} = \frac{2}{3} \mathbf{m} (2v_y - u_x) \quad (8.3)$$

where \mathbf{m} is the viscosity.

One more equation is needed in order to close the system: an equation of state. For the validation purpose, the ideal gas equation of state is used. This equation can be written as follows

$$p = (\mathbf{g} - 1) \mathbf{r} e \quad (8.4)$$

where $\mathbf{g} = \frac{C_p}{C_v}$ is the ratio of specific heats.

For the actual phase change cases, however, other equations of state need to be used. A useful equation of state, which is also valid for the liquid phase, is called the *stiffened gas equation of state* [114] and can be written as

$$p = (\tilde{g} - 1) \rho e - \tilde{g} B \quad (8.5)$$

where \tilde{g} and B are constants, available in the literature, for different materials at different ranges of pressure/temperature.

Note that once the energy field is calculated using the numerical method, the enthalpy field will be known. The temperature field can then be computed from the enthalpy field, using the same procedures that were explained in the previous chapters. The phase change effects will, therefore, be accounted for in the Navier-Stokes code.

8.2 A Space-Time CE/SE Navier-Stokes Scheme

Consider Eq. (8.1). This equation is similar, in the form of representation, to the axisymmetric governing equation, i.e., Eq. (5.6). Of course Eq. (5.6) is a scalar equation while Eq. (8.1) is a vector equation. Therefore, the vector analogue of the same CE/SE procedure used for the axisymmetric case, including treatment of the source term, can be employed here. The integral governing equation can then be written analogous to Eq. (5.8). The final CE/SE equation, therefore, becomes

$$\vec{U}_j^n = \sum_{k=1}^3 \vec{R}^{(k)} \bigg/ \sum_{k=1}^3 S^{(k)} \quad (8.6)$$

where

$$\begin{aligned} \bar{R}^{(k)} = & S^{(k)} \{ \bar{U}(x_c^{(k)}, y_c^{(k)}, t^{n-1/2}; j_k, n-1/2) + \\ & \frac{\Delta t}{2} \tilde{S}(x_c^{(k)}, y_c^{(k)}, t^n - \Delta t/4; j_k, n-1/2) \} - \sum_{l=1}^2 \bar{I}^{(l,k)} \end{aligned}$$

and $\bar{I}^{(l,k)}$ is calculated from

$$\begin{aligned} \bar{I}^{(l,k)} = & \{ \bar{F}(x_c^{(l,k)}, y_c^{(l,k)}, t^n - \Delta t/4; j_k, n-1/2) n_x^{(l,k)} \\ & + \bar{G}(x_c^{(l,k)}, y_c^{(l,k)}, t^n - \Delta t/4; j_k, n-1/2) n_y^{(l,k)} \} S^{(l,k)} \end{aligned} \quad (8.7)$$

Note that the notation used above is defined in vector form as

$$\begin{aligned} \bar{\Psi}(x, y, t; j, n) = & \bar{\Psi}_j^n + (\bar{\Psi}_x)_j^n (x - x'_j) \\ & + (\bar{\Psi}_y)_j^n (y - y'_j) + (\bar{\Psi}_t)_j^n (t - t^n) \end{aligned} \quad (8.8)$$

where $\bar{\Psi}$ can be \bar{U} , \tilde{S} , \bar{F} , or \bar{G} . In the above equation, first-order time and space derivatives of the flux functions are needed. As explained in [79], the independent parameters needed in this CE/SE formulation are \bar{U} , \bar{U}_x , and \bar{U}_y . Therefore, using the chain rule we have

$$\frac{\partial y_i}{\partial w} = \frac{\partial y_i}{\partial U_j} \frac{\partial U_j}{\partial w}, \quad i=1,2,3,4, \text{ and } j=1,2,3,4 \quad (8.9)$$

where \vec{y} is either \vec{F} or \vec{G} , and w can be either x or y . Further, y_i and U_i refer to components of \vec{y} and \vec{U} , respectively. The derivation of the Jacobian components, i.e. $\frac{\partial y_i}{\partial U_j}$ are given in Appendix C.

Once $\frac{\partial y_i}{\partial w}$, $i=1,2,3,4$, is calculated in the above mentioned manner, the time derivatives of the flux functions, (needed in Eq. (8.8)), can be computed. To perform this, the chain rule is used again

$$\frac{\partial y_i}{\partial t} = \frac{\partial y_i}{\partial U_j} \frac{\partial U_j}{\partial t}, \quad i=1,2,3,4, \text{ and } j=1,2,3,4 \quad (8.10)$$

where $\frac{\partial U_j}{\partial t}$ can be computed using the differential form of the conservation law, i.e. Eq.

(8.1)

$$\frac{\partial \vec{U}}{\partial t} = \tilde{S} - \frac{\partial \vec{F}}{\partial x} - \frac{\partial \vec{G}}{\partial y} \quad (8.11)$$

An important issue to discuss next is the set of boundary conditions. The following section summarizes the boundary conditions used in the cases studied in this chapter.

8.3 A Note on the Boundary Conditions

In order to apply the boundary conditions more accurately, in the Navier-Stokes application, the ghost cells are defined differently, compared to the previous chapters. Consider Fig. 4.2. Let the ghost cell shrink to zero area, in a way that its solution point becomes the normal projection of the solution point of the boundary cell on the boundary. In this way the no-slip boundary conditions, for the solid wall, are applied exactly on the boundary. Since the main benchmark problem that will be studied in this chapter concerns a square driven cavity problem, the boundary conditions are explained in reference to that case.

The density boundary condition is assumed *soft*, i.e., the density of the ghost cell is set equal to that of the boundary cell. Further, the equation of state can be used in order to relate the energy boundary condition to that of pressure.

As mentioned previously, the derivatives of vector \vec{U} , are also considered independent variables. Therefore, boundary conditions are needed for the derivatives. Again consider Eq. (8.1). The first component of this vector equation, i.e. the continuity equations can be helpful in determining some of the derivative boundary conditions. The continuity equation is

$$\frac{\partial \mathbf{r}}{\partial t} + \frac{\partial(\mathbf{r}u)}{\partial x} + \frac{\partial(\mathbf{r}v)}{\partial y} = 0 \quad (8.12)$$

and for a steady state problem, (such as the driven cavity problem), it becomes

$$(\mathbf{r}u)_x + (\mathbf{r}v)_y = \mathbf{r}_x u + \mathbf{r}u_x + \mathbf{r}_y v + \mathbf{r}v_y = 0 \quad (8.13)$$

but the velocity components vanish on the solid boundary, therefore, on a solid wall

$$u_x + v_y = 0 \quad (8.14)$$

Finally, for the square driven cavity problem, consider the horizontal stationary wall. The no-slip condition requires the u component of the velocity to vanish along x -axis. This implies

$$u_x = 0 \quad (8.15)$$

and using Eq. (8.14)

$$v_y = 0 \quad (8.16)$$

Note that Eqs. (8.15) and (8.16) are also valid for a horizontal moving wall, as long as it moves with a constant speed. Further, a similar argument shows that Eqs. (8.15) and (8.16) are also valid for stationary vertical walls. These equations lead to two of the momentum-related derivative boundary conditions, i.e.,

$$\left[\frac{\partial U_2}{\partial x} \right]_{wall} = 0 \quad (8.17)$$

and

$$\left[\frac{\partial U_3}{\partial y} \right]_{wall} = 0 \quad (8.18)$$

The other two momentum-related derivative boundary conditions, i.e., those related to

$\left[\frac{\partial U_2}{\partial y} \right]_{wall}$ and $\left[\frac{\partial U_3}{\partial x} \right]_{wall}$ can be considered *soft*. They can either be assumed equal to

their counterparts on the boundary cell, or alternatively, they can be calculated based on one-sided differences using the values of U_2 and U_3 on the boundary cell.

The derivative boundary conditions, related to the energy, as well as those related to the density, can be considered *soft*.

The subject of the boundary conditions, for a Navier-Stokes scheme, still continues to attract the attention of researchers. An interesting paper that covers this subject is [115].

8.4 Validation tests

The simplest validation case for a flow solver could be the case of a uniform flow in an unbounded domain with non-reflecting boundaries. Therefore, in this section, we start the validation process using this case. Then continue with a more complicated flow benchmark problem of the square driven cavity.

8.4.1. The Uniform Flow Cases

The case of a uniform flow, in an unbounded domain with non-reflecting boundaries, was studied using the computer program. The uniform flow of interest was imposed on the boundaries of a unit square. Two different flows were used as initial conditions: 1) a

uniform flow matching the one imposed on the boundaries, and 2) a uniform flow with a different magnitude and flow angle, compared to the one imposed on the boundaries. Using the former, the program was able to maintain the solution without change for a large number of iterations. Using the latter, the program was able to produce the correct flow. The residuals were studied for these two cases and convergence, (to the order of machine zero), was verified.

8.4.2. The Driven Cavity Problem

The problem considered here, belongs to a class of internal flows, usually bounded, of an incompressible, viscous, Newtonian fluid in which the motion is generated by a portion of the container boundary.

An interesting reference, [116], contains a thorough discussion on the fluid mechanics of the driven cavity. It also offers a section on the importance of the problem and its different applications, e.g., in mixing cavities used to synthesize fine polymeric composites.

As mentioned in [116], the overwhelming importance of these flows is to the basic study of fluid mechanics. In no other class of flows are the boundary conditions so unambiguous. As a consequence, driven cavity flows offer an ideal framework, in which, meaningful and detailed comparisons can be made between results obtained from experiment, theory, and computation. In fact, as hundreds of papers attest, the driven cavity problem is one of the standards used to test new computational schemes. The most comprehensive comparisons between the experimental results obtained in a turbulent flow and the corresponding direct numerical simulations (DNS) have been made for a driven cubical cavity. Finally, driven

cavity flows exhibit almost all phenomena that can possibly occur in incompressible flows: eddies, secondary flows, complex three-dimensional patterns, chaotic particle motions, instabilities, transition, and turbulence.

The special case studied here, however, concerns a two-dimensional square cavity, assumed to be full with no free surfaces, and gravity is assumed to be unimportant. The motion in the cavity is generated by the constant-speed motion of the lid. The geometry of this case is depicted in Fig. 8.1.

As mentioned above, the problem of interest is an incompressible case with no gravity. The acceleration of gravity, in the program, can be easily set equal to zero. The presence of compressibility in the program, however, complicates the matter. Because of compressibility, the problem is no longer defined by the Reynolds number (Re) only. The Mach number also needs to be kept small in order to generate results comparable to the incompressible benchmarks. Another numerical issue to consider is that the Courant-Friedrichs-Lewy (CFL) number of the lid must be kept as large as stability allows, for accuracy purposes.

Before defining the specific problem, it is worthwhile to note that, if only the steady state, incompressible, driven cavity problem was to be solved, the CE/SE method would not be an efficient choice. Usage of the velocity-stream function approach [90], for example, would provide results much more efficiently. Once the transient features of natural convection and phase change are considered, however, the advantages of the CE/SE method become more pronounced.

The problem studied concerns a unit square cavity, filled with air (treated as an ideal gas), for $\text{Re} = \frac{\rho u_\infty L}{\mu} = 400$, where u_∞ is the velocity of the lid, and L denotes the dimension of the square cavity. Further, $\text{Pr} = \frac{C_p \mu}{k} = 0.71$, and Mach number of the lid is equal to 0.05. A quiescent flow is used as the initial condition.

A number of unstructured grids were used to model this problem. Grid independence can be assumed to be achieved, to an acceptable degree, using a 200×200 spatial grid. The streamlines depicted in Fig. 8.2, clearly demonstrate three characteristic vortices of this flow. In Table 8.1, the position of the location of the core of each characteristic vortex is presented, for each grid. The last column contains Ghia's results from [46]. As can be seen, the bulk flow features are resolved, even on a relatively coarse grid. The details of the weakest vortex, i.e., the bottom left vortex, however, are not resolved for grids coarser than 200×200 .

Figure 8.3 compares the horizontal component of the velocity, on the vertical centerline, for different grids, with results from [46]. Similarly, Fig. 8.4 compares the vertical component of the velocity, on the horizontal centerline, for different grids, with results from [46].

Two conclusions can be drawn from these figures: 1) The CE/SE method, on the 200×200 grid, accurately captures the flow details, and 2) The convergence is non-oscillatory, for this Re number. The non-oscillatory convergence means the refinement of the grid results in more accurate solutions that are obtained monotonically. This feature suggests

Vortex	Core (x,y)	75×75 Mesh	117×117 Mesh	150×150 Mesh	200×200 Mesh	[116]
Primary	$x(m)$	0.57	0.56	0.56	0.56	0.56
	$y(m)$	0.63	0.61	0.61	0.61	0.61
Bottom right	$x(m)$	0.90	0.89	0.89	0.89	0.89
	$y(m)$	0.10	0.12	0.12	0.12	0.12
Bottom left	$x(m)$	0.06	0.05	0.05	0.05	0.05
	$y(m)$	0.03	0.04	0.04	0.05	0.05

Table 8.1: Location of the core of the vortices, resulting from usage of different grid spacing

that Richardson's extrapolation can be employed, to provide a more accurate solution, by using the results from two coarse grids. An interesting reference on the possibility of the oscillatory convergence and its treatment is [117].

Figure 8.5 displays the residual history for the 150×150 grid. The residuals are defined based on the absolute value of the difference between the solutions of two consecutive time-steps. This figure, therefore, confirms that a steady state solution is in fact reached.

Figures 8.6 and 8.7 provide visual demonstrations of the second-order accuracy of the method. The error demonstrated in Fig. 8.6 is computed based on the absolute value of the difference between the CE/SE method's results with those of [46], for the horizontal component of the velocity at the center of the cavity. The error demonstrated in Fig. 8.7 is computed based on the x coordinate of the location of the core of the bottom right vortex.

The accuracy of the scheme is assessed based on the above cases. The program also contains body force and phase change features that need to be verified using further relevant benchmark problems in the future.

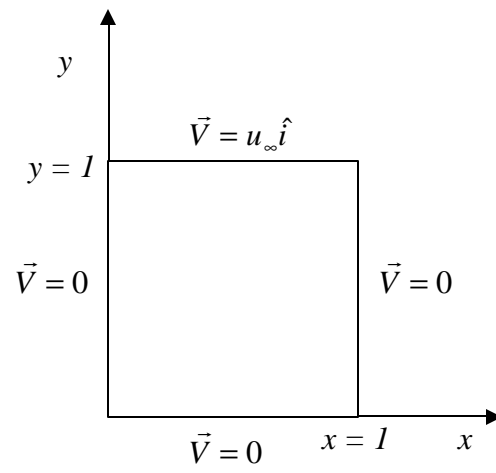
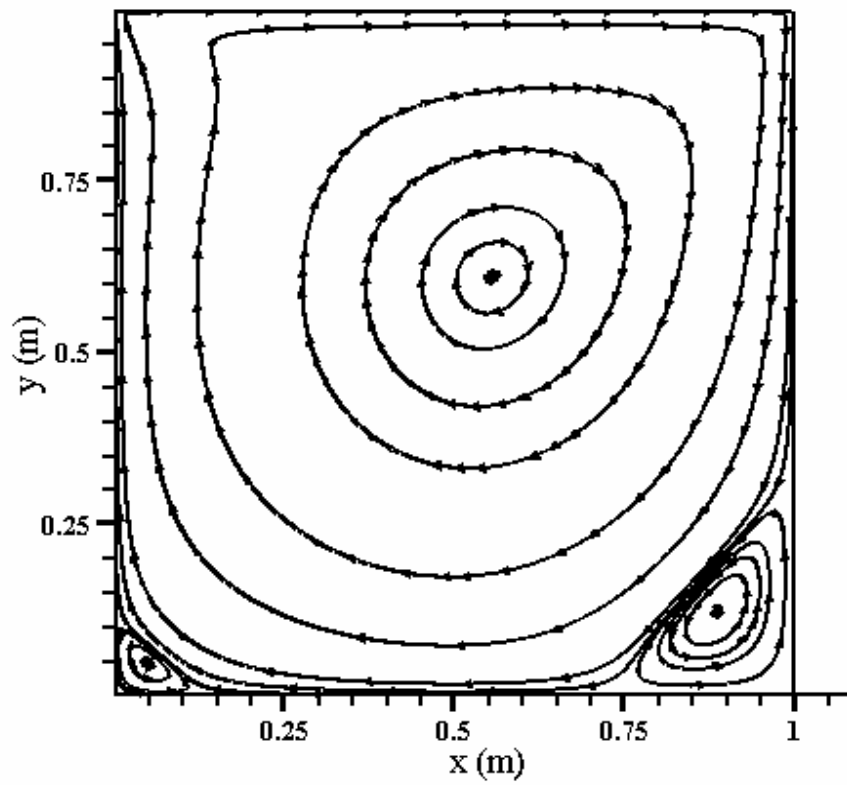


Figure 8.1: Geometry of the driven cavity

Figure 8.2: Streamlines for the 200×200 grid

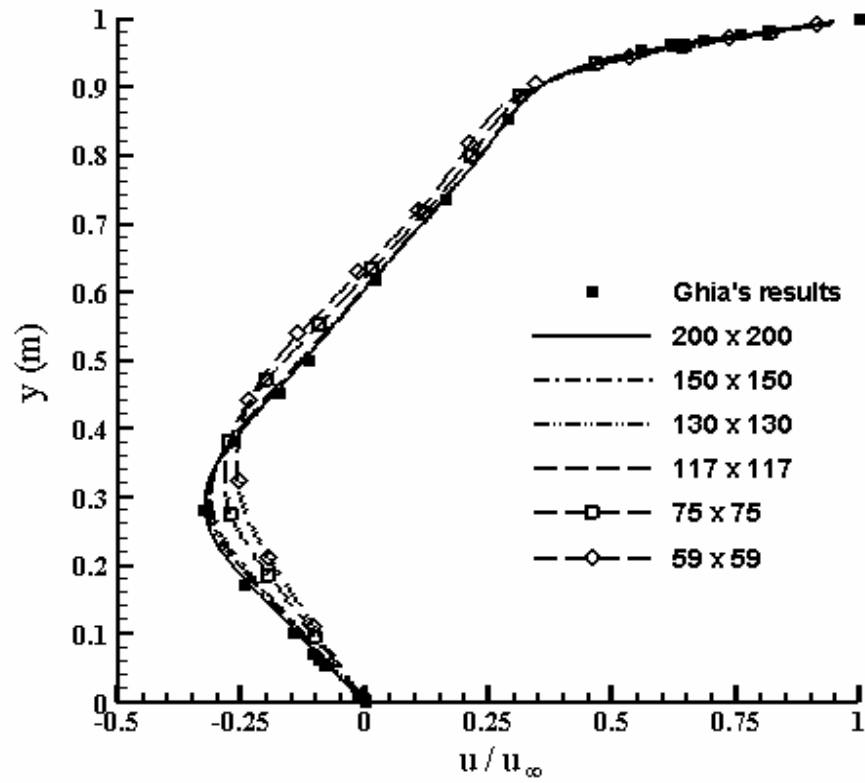


Figure 8.3: Comparison of the horizontal component of the velocity, on the vertical centerline, for different grids, with results from [46]

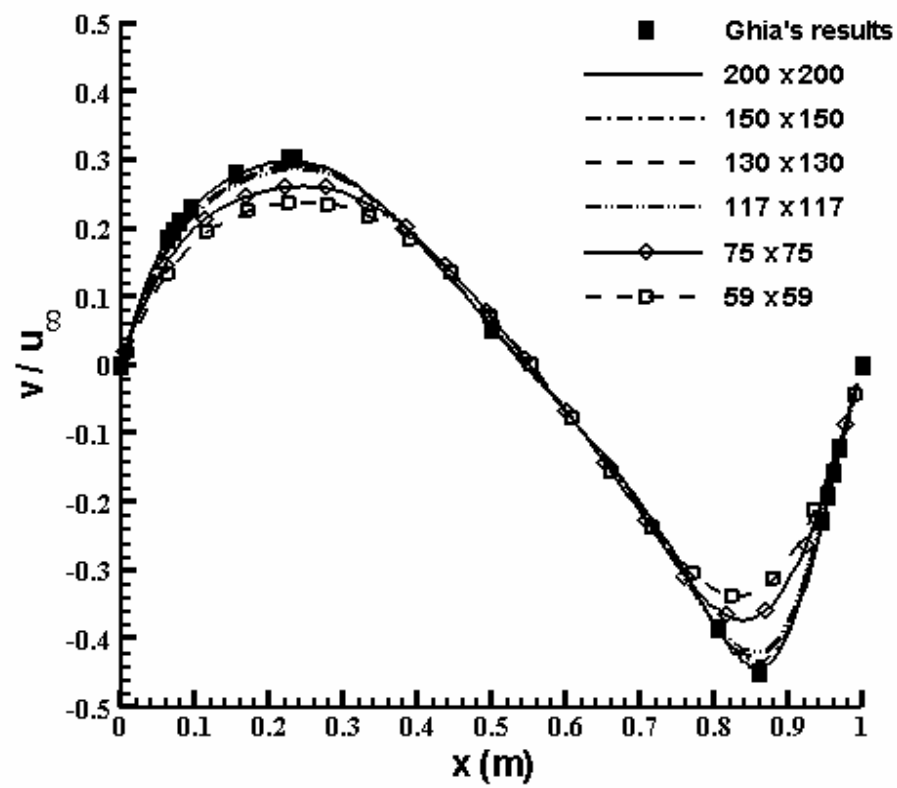


Figure 8.4: Comparison of the vertical component of the velocity, on the horizontal centerline, for different grids, with results from [46]

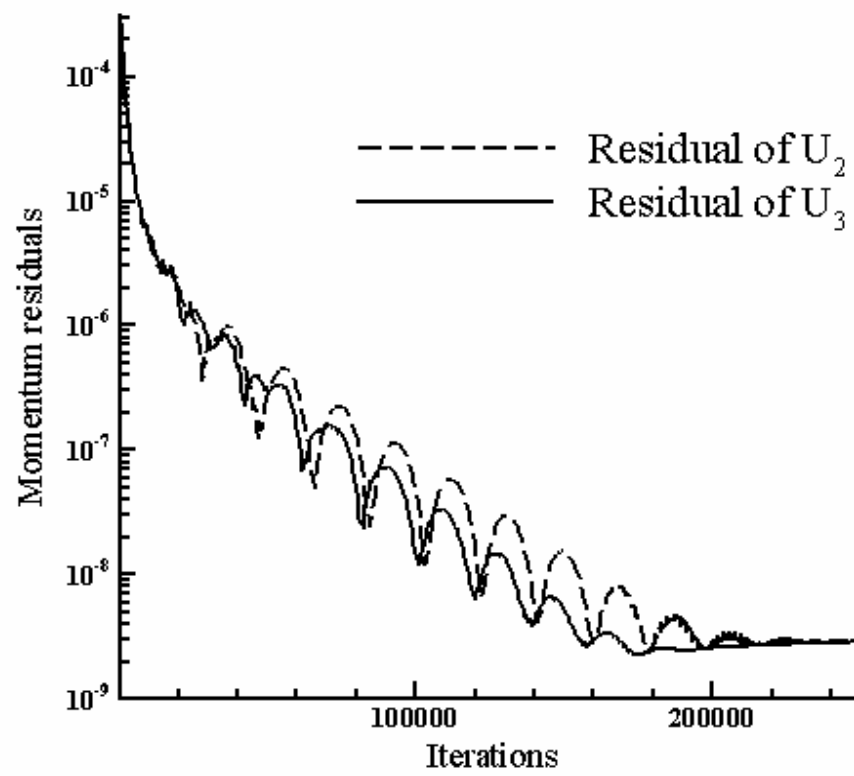


Figure 8.5: Convergence history for the 150×150 grid

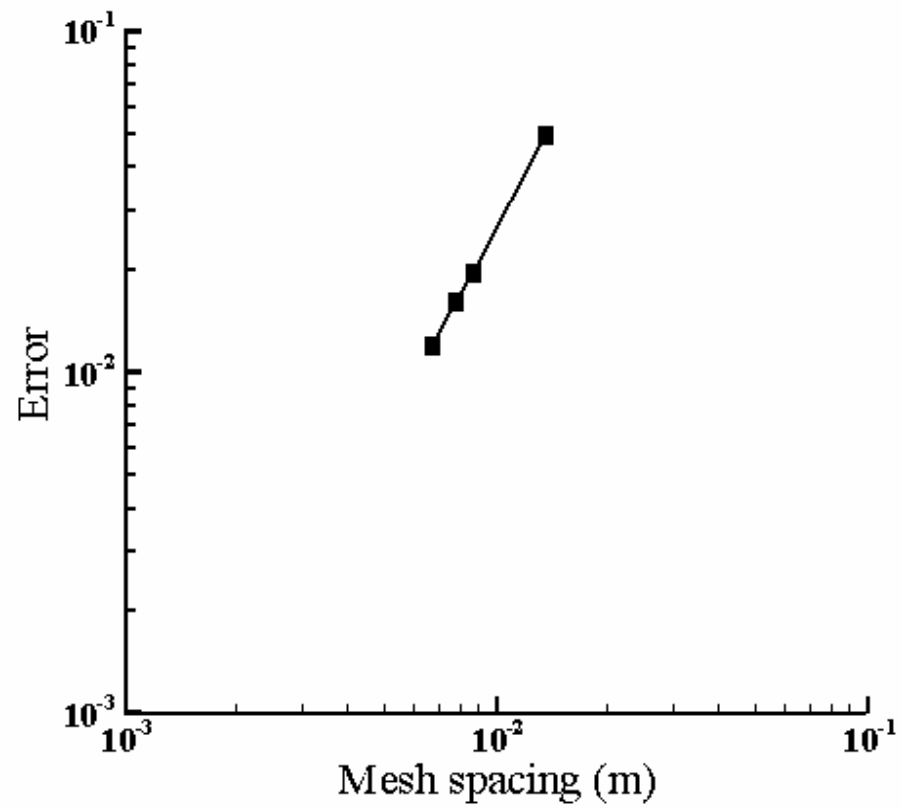


Figure 8.6: Demonstration of the two-dimensional CE/SE Navier-Stokes scheme's second-order accuracy, based on velocity of the center of the cavity

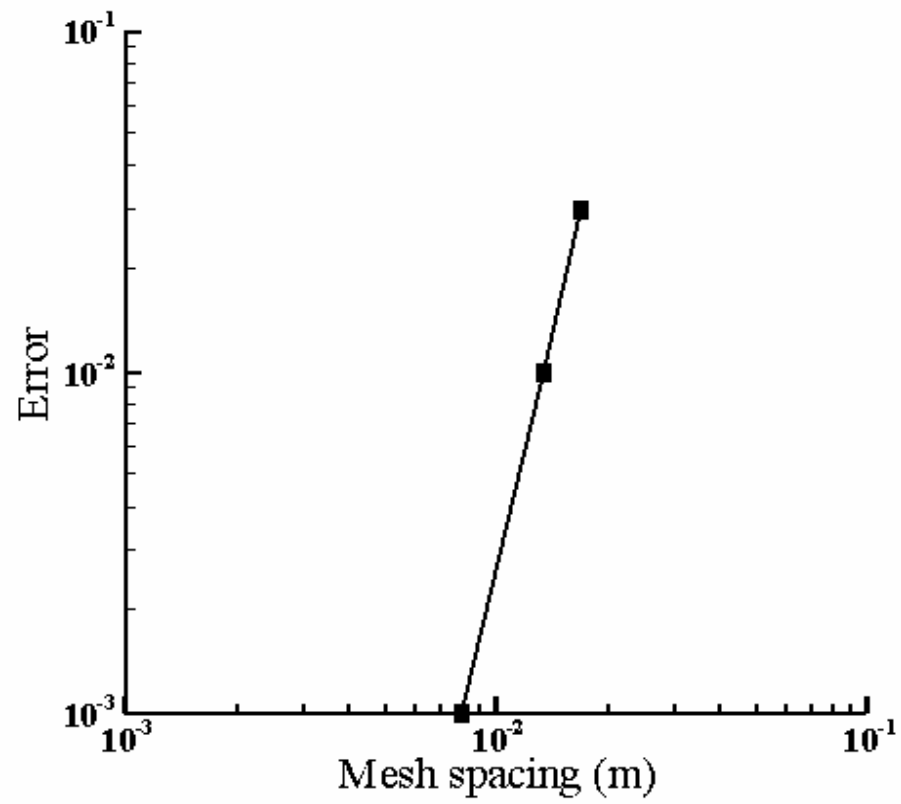


Figure 8.7: Demonstration of the two-dimensional CE/SE Navier-Stokes scheme's second-order accuracy, based on x coordinate of the core of the bottom right vortex

CONCLUSIONS

The numerical simulation of the Enthalpy formulation, for the Stefan problems, is known to be limited by two difficulties: 1) non-physical waviness in the temperature distribution, as well as unwanted oscillations close to the phase interface, for isothermal phase change, and 2) convergence and stability problems, as well as inaccuracies due to overwhelming dissipation of the numerical schemes, at the limit of small Stefan numbers.

The method of space-time conservation element and solution element is known for its low dissipation and dispersion errors, as well as its distinguishingly high capability of accurately capturing discontinuities. Therefore, this numerical method, which has been mainly applied to fluid flow problems, represents an alternative for numerical modeling of moving boundary problems (Stefan problems) such as solid/liquid phase change.

In this dissertation, space-time CE/SE schemes were developed, for the solid/liquid phase change problems, in one-, two-, and three- spatial dimensions. A separate formulation was also presented for the sub-category of axisymmetric problems.

The equivalence of the CE/SE formulation with the conventional formulation was proven mathematically. Each scheme was then validated, numerically, using benchmark problems

without and with phase change. Both analytical and experimental results were used in the validation process. The results revealed that using the space-time CE/SE method, the first problem associated with the numerical modeling of the enthalpy method is eliminated. No non-physical waviness or unwanted oscillation was detected in the results. The second problem, however, still existed. Although accurate results were obtained for small Stefan numbers using the CE/SE method, a case-dependent adjustment in dissipation was needed. This presented the potential for a modification in the original schemes.

An analytical stability study was then conducted on the one-dimensional scheme, using the von Neumann stability analysis. This analysis also revealed the dissipative/dispersive behavior of the numerical scheme and its variation with the Stefan number. The results of this analysis lead to a necessary stability condition, as well as the development of a CE/SE scheme that was, to a considerable degree, insensitive to the value of the Stefan number.

In summary, accurate numerical simulation of the enthalpy method, for the solid/liquid phase change problems, is possible using the space-time CE/SE method. Further, the method can be modified to automatically adjust to the value of the Stefan number. The approach, therefore, presents an alternative potentially capable of treating general phase change problems.

FUTURE WORK

The research presented in this dissertation lays the ground for extensions in several aspects.

The following presents a list of potential directions to further proceed.

- a) Relaxation of the underlying assumptions:
 - i. Relaxation of the no-convection in the melt assumption,
 - ii. Relaxation of the no-density change assumption,
 - iii. Moving towards a more general solver by adding the radiation heat transfer,
 - iv. Moving towards a more general solver by adding the gas phase.
- b) Further experiments with the generated solvers. For example, by adding simple modules, the codes can support variable properties:
 - i. Study of the cases where the properties vary with temperature,
 - ii. Study of the cases where properties are anisotropic inside each phase (variation with spatial coordinates).
- c) Improving the accuracy and efficiency of the numerical approach:
 - i. Usage of the special CE/SE schemes suitable for highly non-uniform grids, in order to reduce the sensitivity of the solvers to grid irregularities.

- ii. Usage of the Richardson's extrapolation (in reference to the driven cavity problem in Chapter 8), for capturing the solution details using coarser grids.
- d) Usage of the space-time CE/SE phase change solvers in the special applications, some of which were mentioned in Chapter 1.

REFERENCES

- [1] Bello-Maldonado, A. A., “Earth Crust Mechanics”, *International Journal of Rock Mechanics and Mining Sciences*, **35** (4/5), pp. 412-415, 1998.
- [2] Zhao, C., Hobbs, B. E., Ord, A., Lin, G., and Mühlhaus, H. B., “An Equivalent Algorithm for Simulating Thermal Effects of Magma Intrusion Problems in Porous Rocks”, *Computer Methods in Applied Mechanics and Engineering*, **192**, pp. 3397-3408, 2003.
- [3] Minster, O., Kufner, E., Vago, J., and Jarvis, D., “Esa Microgravity Research Activities in the Field of Physical Sciences and Applications”, *Earth, Moon and Planets*, **87**, pp. 127-147, 2001.
- [4] Lyne, J. E., Tauber, M. E., and Fought, R. M., “A Computer Model of the Atmospheric Entry of the Tunguska Object”, *Planetary and Space Science*, **46** (2/3), pp. 245-252, 1998.
- [5] Sherif, S. A., Pasumarthi, N., and Bartlett, C. S., “A Semi-empirical Model for Heat Transfer and Ice Accretion on Aircraft Wings in Supercooled Clouds”, *Cold Regions Science and Technology*, **26**, pp. 165-179, 1997.

- [6] Kind, R. J., Potapczuk, M. G., Feo, A., Golia, C., and Shah, A. D., “Experimental and Computational Simulation of In-flight Icing Phenomena”, *Progress in Aerospace Sciences*, **34**, pp. 257-345, 1998.
- [7] Gafur, M. A., Nasrul Haque, M., Narayan Prabhu, and K., “Effect of Chill Thickness and Superheat on Casting/Chill Interfacial Heat Transfer during Solidification of Commercially Pure Aluminum”, *Journal of Materials Processing Technology*, **133**, pp. 257-265, 2003.
- [8] Wu, M., Augthun, M., Wagner, I., Sahm, P. R., and Spiekermann, H., “Numerical Simulation of the Casting Process of Titanium Tooth Crowns and Bridges”, *Journal of Materials Science: Materials in Medicine*, **12**, pp. 485-490, 2001.
- [9] Shepel, S. V., and Paolucci, S., “Numerical Simulation of Filling and Solidification of Permanent Mold Castings”, *Applied Thermal Engineering*, **22**, pp. 229-248, 2002.
- [10] Rabin, Y., and Shitzer, A., “A New Cryosurgical Device for Controlled Freezing I. Setup and Validation Tests”, *Cryobiology*, **33**, pp. 82–92, 1996.
- [11] Schweikert, R. J., and Keanini, R. G., “A Finite Element and Order of Magnitude Analysis of Cryosurgery in the Lung”, *International Communications in Heat and Mass Transfer*, **26** (1), pp. 1-12, 1999.

- [12] Baissalov, R., Sandison, G. A., Donnelly, B. J., Saliken, J. C., McKinnon, J. G., Muldrew, K., and Rewcastle, J. C., “A Semi-empirical Treatment Planning Model for Optimization of Multiprobe Cryosurgery”, *Physics in Medicine and Biology*, **45**, pp. 1085-1098, 2000.
- [13] Liu, J., Zieger, M. A. J., Lakey, J. RT, Woods, E. J., and Critser, J. K., “The Determination of Membrane Permeability Coefficients of Canine Pancreatic Islet Cells and Their Application to Islet Cryopreservation”, *Cryobiology*, **35**, pp. 1-13, 1997.
- [14] Delisle, “Numerical Simulation of Permafrost Growth and Decay”, *Journal of Quaternary Science*, **13** (4), pp. 325–333, 1998.
- [15] Chadwick, J., “Exploration in permafrost”, *Mining Magazine*, **172** (2), pp.103-105, 1995.
- [16] Rajasekhar, K., Harendranath, C. S., Raman, R., and Kulkarni, S. D., “Microstructural Evolution during Solidification of Austenitic Stainless Steel Weld Metals: A Color Metallographic and Electron Microprobe Analysis Study”, *Materials Characterization*, **38**, pp. 53-65, 1997.
- [17] Liu, W., “Computational Analysis and Prediction of Weld-solidification Cracking”, *Computational Materials Science*, **4**, pp. 211-219, 1995.

- [18] van der Ham, F., Witkamp, G. J., de Graauw, J., and van Rosmalen, G. M., “Eutectic Freeze Crystallization: Application to Process Streams and Waste Water Purification, Chemical Engineering and Processing, **37**, pp. 207–213, 1998.
- [19] Gay, G., Lorain, O., Azouni, A., and Aurelle, Y., “Wastewater Treatment by Radial Freezing with Stirring Effects”, Water Research, **37**, pp. 2520-2524, 2003.
- [20] van den Branden, G., Hesius, M., and d’Haeseleer, W., “Comparison of Heat Storage Systems Employing Sensible and Latent Heat”, International Journal of Energy Research, **23**, pp. 605-624, 1999.
- [21] Cabeza, L. F., Mehling, H., Hiebler, S., and Ziegler, F., “Heat Transfer Enhancement in Water when used as PCM in Thermal Energy Storage”, Applied Thermal Engineering, **22**, pp. 1141–1151, 2002.
- [22] HASNAIN, S. M., “Review on Sustainable Thermal Energy Storage Technologies, Part I: Heat Storage Materials and Techniques”, Energy Conversion and Management, **39** (11), pp. 1127-1138, 1998.
- [23] Sulfredge, C. D., Chow, L.C., and Tagavi, K. A., “Void Formation in Radial Solidification of Cylinders”, Journal of Solar Energy Engineering, **114**, pp. 32-39, 1992.
- [24] Elliott, C. M., and Ockendon, J. R., “Weak and Variational Methods for Moving Boundary Problems”, Pitman Advanced Publishing Program, Boston, MA, 1982.

- [25] Šarler, B., “Stefan’s Work on Solid-Liquid Phase Change”, *Engineering Analysis with Boundary Elements*, **16**, pp. 83-92, 1995.
- [26] Rubinstein, L. I., “The Stefan Problem”, *Translations of Mathematical Monographs*, **27**, American Mathematical Society, 1971.
- [27] Alexiades, V., and Solomon, A. D., “Mathematical Modeling of Melting and Freezing Processes”, Hemisphere Publishing Company, Washington, DC, 1993.
- [28] Cannon, J. R., Henry, D., and Kotlow, “Continuous Differentiability of the Free Boundary for Weak Solutions of the Stefan Problem”, *Bulletin of Amer. Math. Soc.*, **80** (1), pp. 45-48, 1974.
- [29] Bankoff, S. G., “Heat Conduction or Diffusion with Change of Phase”, In “Advances in Chemical Engineering”, Drew, T. B., Hoopes, J. W. Jr., and Vermeulen, T., (editors), **5**, pp. 75-150, 1964.
- [30] Muehlbauer, J. C., and Sunderland, J. E., “Heat Conduction with Freezing or Melting”, *Applied Mechanics Reviews*, **18**, pp. 951-959, 1965.
- [31] Fox, L., In “A Survey of Numerical Methods for Partial Differential Equations”, Gladwell, I., and Wait, R., (editors), chapter 20, Clarendon Press, Oxford, 1979.
- [32] Ockendon, J. R., and Hodgkins, W. R., (editors), “Moving Boundary Problems in Heat Flow and Diffusion”, Clarendon Press, Oxford, 1975.

- [33] Crank, J., “Free and Moving Boundary Problems”, Clarendon Press, Oxford, 1984.
- [34] Wilson, D. G., Solomon, A. D., and Boggs, P. T. (editors), “Moving Boundary Problems” Academic Press, New York, 1978.
- [35] Albrecht, J., Collatz, L., and Hoffman, K. –H. (editors), “Numerical Treatment of Free Boundary Value Problems”, Workshop on Numerical Treatment of Free Boundary Value Problems, Oberwolfach, November 16-22, 1980.
- [36] Fasano, A., and Primicerio, M., (editors), “Free Boundary Problems – Theory and applications”, Volumes I & II, (“Research Notes in Mathematics”, 78 and 79), Pitman, London, 1983.
- [37] Cheng, K. C., and Seki, N., “Freezing and Melting Heat Transfer in Engineering”, Hemisphere Publishing Corporation, New York, 1991.
- [38] Douglas, J. and Gallie, T., “On the Numerical Integration of a Parabolic Differential Equation Subject to a Moving Boundary Condition”, Duke Math. J., **22**, pp. 557-571, 1955.
- [39] Meyer, G. H., “The Numerical Solution of Multidimensional Stefan Problems - A Survey”, In “Moving Boundary Problems”, Wilson, D. G., Solomon, A. D., and Boggs, P. T., (editors), pp. 73-89, Academic Press, New York, 1978.
- [40] Boley, B. A., “A General Starting Solution for Melting and Solidifying Slabs”, Int. J. Engng. Sci., **6** (89), 1968.

- [41] Oleinik, O. A., “A Method of Solution of the General Stefan Problem”, Soviet Mathematics – Doklady, **1**, pp. 1350-1354, 1960.
- [42] Dusenberre, G. M., “Numerical Methods for Transient Heat Flow”, Transactions of ASME, **67**, pp. 703-712, 1945.
- [43] Rose, M., “A Method for Calculating Solutions of Parabolic Equations with a Free Boundary”, Mathematics of Computation, **14**, pp. 249-256, 1960.
- [44] Solomon, A. D., “Some Remarks on the Stefan Problem”, Mathematics of Computation, **20**, pp. 347-360, 1966.
- [45] Celentano, D. and Pérez, E., “A Phase-Change Temperature-Based Formulation Including General Latent Heat Effects”, Int. J. Numerical Methods for Heat and Fluid Flow, **6** (8), pp. 71-79, 1996.
- [46] Minkowycz, W. J., Sparrow, E. M., Schneider, G. E., and Pletcher, R. H., 1988, “*Handbook of Numerical Heat Transfer*”, John Wiley & Sons, Inc., New York.
- [47] Chang, S. C. and To, W. M., “A New Numerical Framework for Solving Conservation Laws -- The Method of Space-Time Conservation Element and Solution Element”, NASA TM 104495, 1991.
- [48] Chang, S. C., Wang, X. Y., and Chow, C. Y., “The Space-Time Conservation Element and Solution Element Method: A New High Resolution and Genuinely Multidimensional

Paradigm for Solving Conservation Laws”, *Journal of Computational Physics*, **156**, pp. 89-136, 1999.

[49] Chang, S. C., Wang, X. Y., and To, W. M., “Application of the Space-Time Conservation Element and Solution Element Method to One-Dimensional Convection-Diffusion Problems”, *Journal of Computational Physics*, **165**, pp. 189-215, 2000.

[50] Chang, S.C., “New Developments in the Method of Space-Time Conservation Element and Solution Element -- Applications to the Euler and Navier-Stokes Equations”, NASA TM 106226, 1993.

[51] Wang, X.Y., Chow, C.Y., and Chang, S.C., “Application of the Space-Time Conservation Element and Solution Element Method to Shock-Tube Problem”, NASA TM 106806, 1994.

[52] Chang, S.C., Wang, X.Y., and Chow, C.Y., “New Developments in the Method of Space-Time Conservation Element and Solution Element -- Applications to Two-Dimensional Time-Marching Problems”, NASA TM 106758, 1994.

[53] Wang, X.Y., Chow, C.Y., and Chang, S.C., “Application of the Space-Time Conservation Element and Solution Element Method to Two-Dimensional Advection-Diffusion Problems”, NASA TM 106946, 1995.

[54] Chang, S.C., Wang, X.Y., Chow, C.Y., and Himansu, A., “The Method of Space-Time Conservation Element and Solution Element -- Development of a New Implicit Solver”,

Proceedings of the Ninth International Conference on Numerical Methods in Laminar and Turbulent Flow, July 10-14, Atlanta, GA, C. Taylor and P. Durbetaki, eds., Volume IX, Part I, Pineridge Press, pp. 82-93. Also published as NASA TM 106897, 1995.

[55] Wang, X.Y., Chang, S.C., and Chow, C.Y., "Application of the Method of Space-Time Conservation Element and Solution Element to Axisymmetric Euler Time-Marching Problems," A Collection of Technical Papers, Volume III, pp. 1351--1356, 6th International Symposium on Computational Fluid Dynamics, September 4-8, Lake Tahoe, Nevada, 1995.

[56] Loh, C.Y., Chang, S.C., Scott, J. R., and Yu, S. T., "Application of the Method of Space-Time Conservation Element and Solution Element to Aeroacoustics Problems", A Collection of Technical Papers, Volume II, pp. 713-718, 6th International Symposium on Computational Fluid Dynamics, September 4-8, Lake Tahoe, NV, 1995.

[57] Wang, X.Y., Chow, C.Y., and Chang, S.C., "Numerical Simulation of Flows Caused by Shock-Body Interaction", AIAA Paper 96-2004, 1996.

[58] Wang, X.Y., Chow, C.Y., and Chang, S.C., "Numerical Simulation of Shock Reflection over a Dust Layer Model Using the Space-Time Conservation Element and Solution Element Method", AIAA Paper 98-0443, 1998.

[59] Park, S. J., Yu, S. T., Lai, M.C., Chang, S.C., and Jorgenson, P.C.E., "Direct Calculations of Stable and Unstable ZND Detonations by the Space-Time Conservation Element and Solution Element Method", AIAA paper 98-3212, 1998.

- [60] Wang, X. Y., Chang, S. C., Kao, K. H., and Jorgenson, P. C. E., “A Non-Splitting Unstructured-Triangular-Mesh Euler Solver Based on the Method of Space-Time Conservation Element and Solution Element”, Proceedings of the 16th International Conference on Numerical Method in Fluid Dynamics, Arcachon, France, July 6-July 10, 1998.
- [61] Molls, T., and Molls, F., “Space-Time Conservation Method Applied to Saint Venant Equations”, Journal of Hydraulic Engineering, **125** (5), pp. 501-508, 1998.
- [62] Park S. J., Yu, S. T., Lai, M.C., Chang, S. C., Jorgenson, P. C. E., “Numerical Calculation of Unstable Detonations by the Method of Space-Time Conservation Element and Solution Element”, AIAA Paper 99-0491, 1999.
- [63] Loh, C.Y., Hultgren, L.S., Chang, S.C., Jorgenson, P.C.E., “Vortex Dynamics Simulation in Aeroacoustics by the Space-Time Conservation Element and Solution Element Method”, AIAA Paper 99-0359, 1999.
- [64] Wang, X.Y., Chang, S.C., “A 3-D Structured/Unstructured Euler Solver based on the Space-Time Conservation Element and Solution Element Method”, 14th AIAA CFD Conference June 28, Norfolk, VA, 1999.
- [65] Zhang, Z. C., Yu, S. T., and Chang, S. C., “A Space-Time Conservation Element and Solution Element Method for Solving the Two- and Three-Dimensional Unsteady Euler Equations using Quadrilateral and Hexahedral Meshes”, Journal of Computational Physics, **175**, pp. 168-199, 2002.

- [66] Guo, Y., Hsu, A. T., Wu, J. Yang, Z., and Oyedrian, A., “Extension of CE/SE Method to 2D Viscous Flows”, AIAA Paper 2000-3385, 2000.
- [67] Chen, K. H., and Liu, N. S., “Navier-Stokes Solution of the FLUX Code: A Module for the NCC Solver using the Concept of Space-Time Conservation Element and Solution Element”, AIAA 2000-0455, 2000.
- [68] Liu, N. S., and Chen, K. H., “FLUX: An Alternative Flow Solver for the National Combustion Code”, AIAA Paper 99-1079, 1999.
- [69] Liu, N. S. and Chen, K. H., “An Alternative Flow Solver for the NCC –The FLUX Code and Its Algorithm”, AIAA Paper 2001-0973.
- [70] Wang, X. Y., Chang, S. C., Jorgenson, P. C. E., “Prediction of Sound Waves Propagating Through a Nozzle Without/With a Shock Wave using the Space-Time CE/SE Method”, AIAA Paper 2000-0222, 2000.
- [71] Loh, C. Y., Hultgren, L. S., Chang, S. C., Jorgenson, P. C. E., “Aeroacoustic Computation for Nearly Fully Expanded Supersonic Jets Using the CE/SE Method”, AIAA Paper 2000-2010, 2000.
- [72] Loh, C. Y., Hultgren, L. S., Chang, S. C., Jorgenson, P. C. E., “Noise Computation of a Shock-Containing Supersonic Axisymmetric Jet by the CE/SE Method”, AIAA Paper

2000-0475, presented at the 38th AIAA Aerospace Sciences Meeting, January 10-13, Reno, NV, 2000.

[73] Himansu, A., Jorgenson, P. C. E., Wang, X. Y., Chang, S. C., “Parallel CE/SE Computations via Domain Decomposition”, Proceedings of the First International Conference on Computational Fluid Dynamics, July 9-14, Kyoto, Japan, 2000.

[74] Chang, S. C., Wu, Y., Wang, X. Y., Yang, V., “Local Mesh Refinement in the Space-Time Conservation Element and Solution Element Method”, Proceedings of the First International Conference on Computational Fluid Dynamics, held July 9-14, Kyoto, Japan, 2000.

[75] Loh, C. Y., Hultgren, L. S., and Chang, S. C., “Wave Computation in Incompressible Flow using the Space-Time Conservation Element and Solution Element Method”, AIAA Journal, **39** (5), pp. 794-801, 2001.

[76] Loh, C. Y., and Zaman, K. B. M. Q., “Numerical Investigation of ‘Transonic Resonance’ with a Convergent-Divergent Nozzle”, AIAA Journal, **40** (12), pp. 2393-2401, 2002.

[77] Wang, X. Y., Chen, C. L., Liu, Y., “The Space-Time CE/SE Method for Solving Maxwell's Equations in Time-Domain”, 2002 IEEE International Symposium on Antennas and Propagation and USNC/URSI National Radio Science Meeting, June 16-21, San Antonio, TX, 2002.

- [78] Yang, D., Yu, S. T., and Zhao, J., “Convergence and Error Bound Analysis for the Space-Time CESE Method”, *Numerical Methods for Partial Differential Equations*, **17**, pp. 64-78, 2001.
- [79] Chang, S. C., “The Method of Space-Time Conservation Element and Solution Element – A New Approach for Solving the Navier-Stokes and Euler Equations”, *Journal of Computational Physics*, **119**, pp. 295-324, 1995.
- [80] Chang, S. C., 2002, “Courant Number Insensitive CE/SE Schemes”, *AIAA Paper* 2002-3890, 2002.
- [81] Chang, S. C., and Wang, X. Y., 2003, “Multi-dimensional Courant Number Insensitive CE/SE Euler Solvers for Applications Involving Highly Non-uniform Meshes”, *AIAA Paper* 2003-5285, 2002.
- [82] Callen, H. B., “Thermodynamics”, John Wiley & Sons, New York, 1960.
- [83] Turnbull, D., “The Undercooling of Liquids”, *Scientific American*, **212**, pp. 38-46, 1965.
- [84] Myshkis, A. D., Babskii, V. G., Kopachevskii, N. D., Slobozhanin, L. A., and Tyuptsov, A. D., “Low Gravity Fluid Mechanics”, Springer-Verlag, Berlin 1987.
- [85] Bhattacharya, M., Basak, T., and Ayappa, K. G., “A Fixed Grid Finite Element Based Enthalpy Formulation for Generalized Phase Change Problems: Role of Superficial Mushy Region”, *International Journal of Heat and Mass Transfer*, **45**, 4881-4898, 2002.

- [86] Voller, V. R., and Swaminathan, C. R., “General Source-Based Method for Solidification Phase Change”, *Numerical Heat Transfer, Part B*, **19**, pp. 175-189, 1991.
- [87] Wang, X. Y. and Chang, S. C., 1999, “A 2D Non-Splitting Unstructured Triangular Mesh Euler Solver Based on the Space Time Conservation Element and Solution Element Method”, *Computational Fluid Dynamics Journal*, **8** (2), pp. 309-325.
- [88] Shamsundar, N., and Sparrow, E. M., “Analysis of Multidimensional Conduction Phase Change via the Enthalpy Model”, *Journal of Heat Transfer*, **97**, pp. 333-340, 1975.
- [89] Thomas Jr., G. B., and Finney, R. L., “Calculus and Analytic Geometry”, 7th Ed., Addison-Wesley Publishing Company, Reading, Massachusetts, 1991.
- [90] Tannehill, J. C., Anderson, D. A., and Pletcher, R. H., “*Computational Fluid Mechanics and Heat Transfer*”, second edition, Taylor & Francis, Washington, DC, 1997.
- [91] Ayasoufi, A., “A Solution-Adaptive Method for Solving Euler Equations in Axisymmetric Problems using Unstructured Triangular Grid”, Master Thesis, Sharif University of Technology, Tehran, Iran, 1997.
- [92] Lunardini, V. J., “*Heat Transfer in Cold Climates*”, Van Nostrand Reinhold Company, New York, 1981.
- [93] Rathjen, K. A. and Jiji, L. M., “Heat Conduction with Melting or Freezing in a Corner”, *Journal of Heat Transfer*, **93**, pp. 101-109, 1971.

- [94] Ouyang, T. and Tamma, K. K., "On Adaptive Time Stepping Approaches for Thermal Solidification Processes", *Int. J. Numerical Methods for Heat and Fluid Flow*, **6**, (2), pp. 37-50, 1996.
- [95] Rahmani, R. K., "Unstructured Three-Dimensional Delaunay Grid Generation and Solving Three-Dimensional Euler Equations", Master Thesis, Sharif University of Technology, Tehran, Iran, 1997.
- [96] Eyres, N. R., Hartree, D. R., Ingham, F. R. S., J., Jackson, R., Sarjant, R. J., and Wagstaff, S. M., "The Calculation of Variable Heat Flow in Solids", *Philosophical Transactions of the Royal Society of London, Series A, Mathematical and Physical Sciences*, **240**, pp.1-57, 1946.
- [97] Richards, P. M., "Interface Kinetics Kinetics of Freezing and Melting with a Density Change", *Physical Review B*, **38**(4), pp. 2727-2739, 1988.
- [98] Jany, P., and Bejan, A., "Scales of Melting in the Presence of Natural Convection in a Rectangular Cavity Filled with Porous Medium", *Transactions of the ASME*, **110**, pp. 526-529, 1988.
- [99] Szimmat, J., "Numerical Simulation of Solidification Processes in Enclosures", *Heat and Mass Transfer*, **38**, pp. 279-293, 2002.
- [100] aus der Wiesche, S., and Hofer, E. P., "On the Stefan Problem in a Finite and Moveable System", *Heat and Mass Transfer*, **36**, pp. 305-311, 2000.

- [101] Hwang, K., “Effects of Density and Natural Convection on the Solidification Process of a Pure Metal”, *Journal of Materials Processing Technology*, **71**, pp. 466-476, 1997.
- [102] Charach, Ch. and Zarmi, Y., “Planar Solidification in a Finite Slab: Effects of Density Change”, *Journal of Applied Physics*, **70** (11), pp. 6687-6693, 1991.
- [103] Asako, Y., and Faghri, M., “Effect of Density Change on Melting of Unfixed Rectangular Phase-Change Material under Low-Gravity Environment”, *Numerical Heat Transfer, Part A*, **36**, pp. 825-838, 1999.
- [104] Wolff, F., and Viskanta, R., “Solidification of a pure metal at a vertical wall in the presence of liquid superheat”, *International Journal of Heat and Mass Transfer*, **31** (8), pp. 1735-1744, 1988.
- [105] Beckermann, C., and Viskanta, R., “Effect of Solid Subcooling on Natural Convection Melting of a Pure Metal”, *Transactions of the ASME*, **111**, pp. 416-424, 1989.
- [106] Zhang, X., and Nguyen, T. H., “Solidification of a Superheated Fluid in a Porous Medium: Effects of Convection”, *International Journal of Numerical Methods for Heat & Fluid Flow*, **9** (1), pp. 72-91, 1999.
- [107] Hao, Y. L., and Tao, Y. -X., “Heat Transfer Characteristics of Melting Ice Spheres under Forced and Mixed Convection”, *Journal of Heat Transfer*, **124**, pp. 891-903, 2002.

- [108] Koster, J. N., Derebail, R., and Grötzbach, A., “Visualization of Convective Solidification in a Vertical Layer of Eutectic Ga-In Melt”, *Applied Physics A*, **64**, pp. 45-54, 1997.
- [109] Starovoitov, V. N., “On the Stefan Problem with Different Phase Densities”, *ZAMM.Z.Angew.Math.Mech.*, **80** (2), pp. 103-111, 2000.
- [110] Vierendeels, J., Merci, B., and Dick, E., “Numerical Study of Natural Convection Heat Transfer with Large Temperature Differences”, *International Journal of Numerical Methods for Heat & Fluid Flow*, **11** (4), pp. 329-341, 2001.
- [111] Vierendeels, J., Merci, B., and Dick, E., “Benchmark Solutions for the Natural Convection Heat Transfer Problem in a Square Cavity with Large Horizontal Temperature Difference”, *International Journal of Numerical Methods for Heat & Fluid Flow*, **13** (8), pp. 1057-1078, 2003.
- [112] Zhang, Z. C., Wang, X. Y., Chang, S. C., “The Space-Time CE/SE Method for the Navier-Stokes Equations in Three Spatial Dimensions”, *AIAA Paper 2000-2331*, 2000.
- [113] Zhang, M., and Yu, S. T. J., “Solving the Navier-Stokes Equations by the CESE Method”, *AIAA Paper 2004-0075*.
- [114] Haller, K. K., Ventikos, Y., and Poulikakos, D., “Wave Structure in the Contact Line Region during High Speed Droplet Impact on a Surface: Solution of the Riemann Problem

for the Stiffened Gas Equation of State”, Journal of Applied Physics, **93** (5), pp. 3090-3097, 2003.

[115] Poinso, T. J., and Lele, S. K., “Boundary Conditions for Direct Simulation of Compressible Viscous Flows”, Journal of Computational Physics, **101**, pp. 104-129, 1992.

[116] Shankar, P. N., and Deshpande, M. D., “Fluid Mechanics in the Driven Cavity”, Annual Reviews Fluid Mechanics, **32**, pp. 93–136, 2000.

[117] Celik, I. B., Hu, J. L. G., and Shaffer C., “Limitations of Richardson Extrapolation and Possible Remedies for Estimation of Discretization Error”, Proceedings of HT-FED04, 2004 ASME Heat Transfer/Fluids Engineering Summer Conference, July 11-15, 2004, Charlotte, North Carolina, USA, 2004.

APPENDIX A

This appendix contains the derivation of the insulated boundary conditions for temperature, on an arbitrarily oriented boundary in a three-dimensional geometry. Figure A.1 depicts the geometric parameters involved.

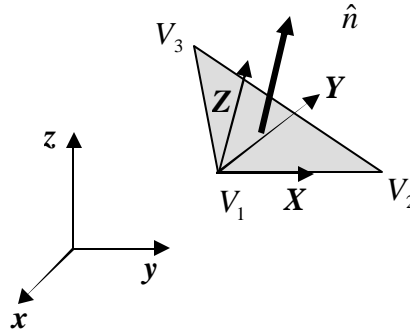


Figure A.1: Geometric parameters involved in the transformation of the coordinates

The original coordinate system of the problem is xyz . Triangle $V_1V_2V_3$ represents an arbitrary boundary face. This triangle is shared between a tetrahedral boundary cell called cell ‘b’, and its corresponding ghost cell referred to as cell ‘g’. The unit outward vector, normal to this boundary face, is represented by

$$\hat{n} = n_x \hat{e}_x + n_y \hat{e}_y + n_z \hat{e}_z \quad (\text{A.1})$$

where \hat{e}_x , \hat{e}_y , and \hat{e}_z are the basic unit vectors of xyz system.

As mentioned in previous chapters, it is usually easier to define the boundary conditions in a boundary fitted coordinate system, such as XYZ . As can be seen from Fig. A.1, this new coordinate system can be generated by rotating the original system until the transformed z -axis, i.e., the Z -axis, becomes parallel to \hat{n} . Further, as a matter of convenience, the rotation is selected such that the transformed x -axis, i.e., the X -axis, becomes parallel to V_1V_2 . The origin of the new system can be selected arbitrarily. Again, for convenience in programming, a translation is also employed and the origin of the transformed system is selected at vertex V_1 of the boundary triangle.

Before starting the derivation of the transformation matrix, referred to as \bar{T} , it is of value to outline the procedure of defining second-order derivatives of the temperature. Let matrix \bar{T} represent the transformation of the coordinates from xyz system to XYZ system, as illustrated in Fig. A.2. The inverse transformation will be referred to as \bar{T}^{-1} . The procedure can then be summarized as follows.

1. The value of the temperature in cell 'g' is set equal to that of cell 'b'.
2. From a physical point of view, the insulated boundary condition of temperature in the XYZ system can be defined as follows
 - a. The first-order spatial derivatives:

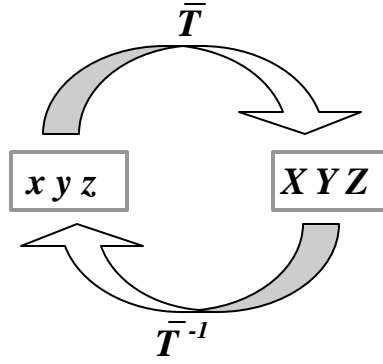


Figure A.2: Transformation of the coordinate system

$$\begin{bmatrix} T_X \\ T_Y \\ T_Z \end{bmatrix}_g = \begin{bmatrix} T_X \\ T_Y \\ -T_Z \end{bmatrix}_b \quad (\text{A.2})$$

b. The second-order spatial derivatives:

$$\begin{bmatrix} T_{XX} \\ T_{YX} \\ T_{ZX} \\ T_{XY} \\ T_{YY} \\ T_{ZY} \\ T_{XZ} \\ T_{YX} \\ T_{ZZ} \end{bmatrix}_g = \begin{bmatrix} T_{XX} \\ T_{YX} \\ -T_{ZX} \\ T_{XY} \\ T_{YY} \\ -T_{ZY} \\ -T_{XZ} \\ -T_{YX} \\ T_{ZZ} \end{bmatrix}_b \quad (\text{A.3})$$

c. The second-order mixed derivatives containing time, i.e. T_{xt} , T_{yt} , T_{zt} :

since the transformation is accomplished in space only, the time coordinate remains intact. Therefore, the formula derived for the first-order derivatives can be used for these mixed derivatives by replacing each first order derivative by its corresponding second-order derivative mixed with time differentiation.

3. The inverse transformation can then be used to transform the values of the derivatives at cell ‘g’ back to the original system xyz .

To derive the transformation matrices for the first- and second-order derivatives, the metrics of the transformation are needed. For this purpose return to Fig. A.1. Let’s refer to the basic unit vectors of XYZ system as \hat{e}_x , \hat{e}_y , and \hat{e}_z . Obviously,

$$\hat{e}_z = \hat{n} = n_x \hat{e}_x + n_y \hat{e}_y + n_z \hat{e}_z \quad (\text{A.4})$$

Further, since the X-axis is aligned with $V_1 V_2$, unit vector \hat{e}_x can be calculated as

$$\hat{e}_x \equiv d_x \hat{e}_x + d_y \hat{e}_y + d_z \hat{e}_z \quad (\text{A.5})$$

where

$$d_x = \frac{x(V_2) - x(V_1)}{d}, d_y = \frac{y(V_2) - y(V_1)}{d}, d_z = \frac{z(V_3) - z(V_1)}{d} \quad (\text{A.6})$$

and

$$d = \sqrt{(x(V_2) - x(V_1))^2 + (y(V_2) - y(V_1))^2 + (z(V_2) - z(V_1))^2} \quad (\text{A.7})$$

Finally, the unit vector \hat{e}_Y can be found using the cross product of the other two unit vectors, i.e.

$$\hat{e}_Y = \hat{e}_Z \times \hat{e}_X = \begin{vmatrix} \hat{e}_x & \hat{e}_y & \hat{e}_z \\ n_x & n_y & n_z \\ d_x & d_y & d_z \end{vmatrix} \quad (\text{A.8})$$

Therefore,

$$\hat{e}_Y \equiv m_x \hat{e}_x + m_y \hat{e}_y + m_z \hat{e}_z \quad (\text{A.9})$$

where

$$m_x = n_y d_z - n_z d_y, \quad m_y = n_z d_x - n_x d_z, \quad \text{and} \quad m_z = n_x d_y - n_y d_x \quad (\text{A.10})$$

Consider an arbitrary point (X, Y, Z) in the XYZ system. Using Eqs.(A.4), (A.5), and (A.9), and also taking into account the translation of the coordinate systems, the position vector of this node can be written as follows

$$\begin{aligned}
X \hat{e}_x + Y \hat{e}_y + Z \hat{e}_z &= X (d_x \hat{e}_x + d_y \hat{e}_y + d_z \hat{e}_z) \\
&\quad + Y (m_x \hat{e}_x + m_y \hat{e}_y + m_z \hat{e}_z) \\
&\quad + Z (n_x \hat{e}_x + n_y \hat{e}_y + n_z \hat{e}_z) \\
&= (X d_x + Y m_x + Z n_x) \hat{e}_x \\
&\quad + (X d_y + Y m_y + Z n_y) \hat{e}_y \\
&\quad + (X d_z + Y m_z + Z n_z) \hat{e}_z \\
&= [x - x(V_1)] \hat{e}_x + [y - y(V_1)] \hat{e}_y + [z - z(V_1)] \hat{e}_z
\end{aligned} \tag{A.11}$$

or in matrix form

$$\begin{bmatrix} x - x(V_1) \\ y - y(V_1) \\ z - z(V_1) \end{bmatrix} = \bar{T} \begin{bmatrix} X \\ Y \\ Z \end{bmatrix} \tag{A.12}$$

where

$$\bar{T} = \begin{bmatrix} d_x & m_x & n_x \\ d_y & m_y & n_y \\ d_z & m_z & n_z \end{bmatrix} \tag{A.13}$$

is the coordinate transformation matrix that can be used, for example, in the geometric calculations related to the ghost cell as mirror image of the boundary cell with respect to the boundary. However, further calculations are needed for transformation of the derivatives. Before proceeding to that subject, it is worthwhile to note that the inverse transformation, \bar{T}^{-1} , is also the transpose of the matrix \bar{T} and can be easily found to be

$$\bar{T}^{-1} = \begin{bmatrix} d_x & d_y & d_z \\ m_x & m_y & m_z \\ n_x & n_y & n_z \end{bmatrix} = \bar{T}^T \quad (\text{A.14})$$

In order to transform the first-order derivatives of the temperature, the chain rule can be used as follows

$$\left\{ \begin{array}{l} \frac{\partial T}{\partial X} = \frac{\partial T}{\partial x} \frac{\partial x}{\partial X} + \frac{\partial T}{\partial y} \frac{\partial y}{\partial X} + \frac{\partial T}{\partial z} \frac{\partial z}{\partial X} \\ \frac{\partial T}{\partial Y} = \frac{\partial T}{\partial x} \frac{\partial x}{\partial Y} + \frac{\partial T}{\partial y} \frac{\partial y}{\partial Y} + \frac{\partial T}{\partial z} \frac{\partial z}{\partial Y} \\ \frac{\partial T}{\partial Z} = \frac{\partial T}{\partial x} \frac{\partial x}{\partial Z} + \frac{\partial T}{\partial y} \frac{\partial y}{\partial Z} + \frac{\partial T}{\partial z} \frac{\partial z}{\partial Z} \end{array} \right. \quad (\text{A.15})$$

Differentiation of Eq.(A.12) produces again the Jacobian matrix of the transformation

$$\begin{bmatrix} \frac{\partial x}{\partial X} & \frac{\partial x}{\partial Y} & \frac{\partial x}{\partial Z} \\ \frac{\partial y}{\partial X} & \frac{\partial y}{\partial Y} & \frac{\partial y}{\partial Z} \\ \frac{\partial z}{\partial X} & \frac{\partial z}{\partial Y} & \frac{\partial z}{\partial Z} \end{bmatrix} = \begin{bmatrix} d_x & m_x & n_x \\ d_y & m_y & n_y \\ d_z & m_z & n_z \end{bmatrix} = \bar{T} \quad (\text{A.16})$$

which can be used to write Eq.(A.15) in the following matrix form

$$\begin{bmatrix} \frac{\partial T}{\partial X} \\ \frac{\partial T}{\partial Y} \\ \frac{\partial T}{\partial Z} \end{bmatrix} = \bar{T}^T \begin{bmatrix} \frac{\partial T}{\partial x} \\ \frac{\partial T}{\partial y} \\ \frac{\partial T}{\partial z} \end{bmatrix} \quad (\text{A.17})$$

and

$$\begin{bmatrix} \frac{\partial T}{\partial x} \\ \frac{\partial T}{\partial y} \\ \frac{\partial T}{\partial z} \end{bmatrix} = \bar{T} \begin{bmatrix} \frac{\partial T}{\partial X} \\ \frac{\partial T}{\partial Y} \\ \frac{\partial T}{\partial Z} \end{bmatrix} \quad (\text{A.18})$$

The chain rule can again be used to provide the transformation matrix for the second-order derivatives. This transformation matrix will be a 9 by 9 matrix, with each row transforming one of the 9 spatial second-order derivatives. As an example, one row of this matrix is derived below. Consider the derivative T_{XX} , using the first row of the transformation matrix \bar{T}^T , we can write

$$T_{XX} = \frac{\partial}{\partial X} \left(\frac{\partial T}{\partial X} \right) = \begin{bmatrix} d_x & d_y & d_z \end{bmatrix} \begin{bmatrix} \frac{\partial}{\partial x} \left(\frac{\partial T}{\partial X} \right) \\ \frac{\partial}{\partial y} \left(\frac{\partial T}{\partial X} \right) \\ \frac{\partial}{\partial z} \left(\frac{\partial T}{\partial X} \right) \end{bmatrix}$$

The same row of the same transformation matrix can be used again to produce

$$\begin{aligned}
T_{XX} &= \begin{bmatrix} d_x & d_y & d_z \end{bmatrix} \left[\begin{array}{l} \frac{\partial}{\partial x} \left\{ \begin{bmatrix} d_x & d_y & d_z \end{bmatrix} \begin{bmatrix} \partial T / \partial x \\ \partial T / \partial y \\ \partial T / \partial z \end{bmatrix} \end{array} \right. \\ \frac{\partial}{\partial y} \left\{ \begin{bmatrix} d_x & d_y & d_z \end{bmatrix} \begin{bmatrix} \partial T / \partial x \\ \partial T / \partial y \\ \partial T / \partial z \end{bmatrix} \end{array} \right. \\ \frac{\partial}{\partial z} \left\{ \begin{bmatrix} d_x & d_y & d_z \end{bmatrix} \begin{bmatrix} \partial T / \partial x \\ \partial T / \partial y \\ \partial T / \partial z \end{bmatrix} \end{array} \right. \end{array} \right] \\
&= \begin{bmatrix} d_x & d_y & d_z \end{bmatrix} \left[\begin{array}{l} \begin{bmatrix} d_x & d_y & d_z \end{bmatrix} \begin{bmatrix} T_{xx} \\ T_{yx} \\ T_{zx} \end{bmatrix} \\ \begin{bmatrix} d_x & d_y & d_z \end{bmatrix} \begin{bmatrix} T_{xy} \\ T_{yy} \\ T_{zy} \end{bmatrix} \\ \begin{bmatrix} d_x & d_y & d_z \end{bmatrix} \begin{bmatrix} T_{xz} \\ T_{yz} \\ T_{zz} \end{bmatrix} \end{array} \right]
\end{aligned}$$

or

$$T_{XX} = \begin{bmatrix} d_x & d_x \\ d_x & d_y \\ d_x & d_z \\ d_y & d_x \\ d_y & d_y \\ d_y & d_z \\ d_z & d_x \\ d_z & d_y \\ d_z & d_z \end{bmatrix}^T \begin{bmatrix} T_{xx} \\ T_{yx} \\ T_{zx} \\ T_{xy} \\ T_{yy} \\ T_{zy} \\ T_{xz} \\ T_{yz} \\ T_{zz} \end{bmatrix} \quad (\text{A.19})$$

The remaining rows can be derived similarly and the final transformation becomes

$$\begin{bmatrix} T_{XX} \\ T_{YX} \\ T_{ZX} \\ T_{XY} \\ T_{YY} \\ T_{ZY} \\ T_{XZ} \\ T_{YZ} \\ T_{ZZ} \end{bmatrix} = M \begin{bmatrix} T_{xx} \\ T_{yx} \\ T_{zx} \\ T_{xy} \\ T_{yy} \\ T_{zy} \\ T_{xz} \\ T_{yz} \\ T_{zz} \end{bmatrix} \quad (\text{A.20})$$

where $M = m_{ij}$, and for $i = 1, \dots, 9$, $j = 1, \dots, 9$ its components are

$$m_{11} = d_x d_x, \quad m_{12} = d_x d_y, \quad m_{13} = d_x d_z, \quad m_{14} = d_y d_x, \quad m_{15} = d_y d_y, \quad m_{16} = d_y d_z,$$

$$m_{17} = d_z d_x, \quad m_{18} = d_z d_y, \quad m_{19} = d_z d_z,$$

$$m_{21} = d_x m_x, \quad m_{22} = d_x m_y, \quad m_{23} = d_x m_z, \quad m_{24} = d_y m_x, \quad m_{25} = d_y m_y, \quad m_{26} = d_y m_z,$$

$$m_{27} = d_z m_x, \quad m_{28} = d_z m_y, \quad m_{29} = d_z m_z,$$

$$m_{31} = d_x n_x, \quad m_{32} = d_x n_y, \quad m_{33} = d_x n_z, \quad m_{34} = d_y n_x, \quad m_{35} = d_y n_y, \quad m_{36} = d_y n_z,$$

$$m_{37} = d_z n_x, \quad m_{38} = d_z n_y, \quad m_{39} = d_z n_z,$$

$$m_{41} = m_x d_x, \quad m_{42} = m_x d_y, \quad m_{43} = m_x d_z, \quad m_{44} = m_y d_x, \quad m_{45} = m_y d_y, \quad m_{46} = m_y d_z,$$

$$m_{47} = m_z d_x, \quad m_{48} = m_z d_y, \quad m_{49} = m_z d_z,$$

$$m_{51} = m_x m_x, \quad m_{52} = m_x m_y, \quad m_{53} = m_x m_z, \quad m_{54} = m_y m_x, \quad m_{55} = m_y m_y,$$

$$m_{56} = m_y m_z, \quad m_{57} = m_z m_x, \quad m_{58} = m_z m_y, \quad m_{59} = m_z m_z,$$

$$m_{61} = m_x n_x, \quad m_{62} = m_x n_y, \quad m_{63} = m_x n_z, \quad m_{64} = m_y n_x, \quad m_{65} = m_y n_y, \quad m_{66} = m_y n_z,$$

$$m_{67} = m_z n_x, \quad m_{68} = m_z n_y, \quad m_{69} = m_z n_z,$$

$$m_{71} = n_x d_x, \quad m_{72} = n_x d_y, \quad m_{73} = n_x d_z, \quad m_{74} = n_y d_x, \quad m_{75} = n_y d_y, \quad m_{76} = n_y d_z,$$

$$m_{77} = n_z d_x, \quad m_{78} = n_z d_y, \quad m_{79} = n_z d_z,$$

$$m_{81} = n_x m_x, \quad m_{82} = n_x m_y, \quad m_{83} = n_x m_z, \quad m_{84} = n_y m_x, \quad m_{85} = n_y m_y, \quad m_{86} = n_y m_z,$$

$$m_{87} = n_z m_x, \quad m_{88} = n_z m_y, \quad m_{89} = n_z m_z,$$

$$m_{91} = n_x n_x, \quad m_{92} = n_x n_y, \quad m_{93} = n_x n_z, \quad m_{94} = n_y n_x, \quad m_{95} = n_y n_y, \quad m_{96} = n_y n_z,$$

$$m_{97} = n_z n_x, \quad m_{98} = n_z n_y, \quad m_{99} = n_z n_z.$$

Conveniently, the inverse of this transformation matrix is also equal to its transpose, therefore

$$\begin{bmatrix} T_{xx} \\ T_{yx} \\ T_{zx} \\ T_{xy} \\ T_{yy} \\ T_{zy} \\ T_{xz} \\ T_{yz} \\ T_{zz} \end{bmatrix} = M^T \begin{bmatrix} T_{XX} \\ T_{YX} \\ T_{ZX} \\ T_{XY} \\ T_{YY} \\ T_{ZY} \\ T_{XZ} \\ T_{YZ} \\ T_{ZZ} \end{bmatrix} \quad (\text{A.21})$$

The procedure outlined in the beginning of this appendix, is then completed by using Eqs.(A.17) and (A.20) in step 2, and using Eqs.(A.18) and (A.21) in step 4 of the procedure.

APPENDIX B: AN UNSTRUCTURED THREE DIMENSIONAL REGULAR GRID GENERATOR

This appendix contains details related to one of the three-dimensional grid generators used in this research. The grid generator of interest is unstructured, but is particularly programmed to generate regular grids in which the minimum angle is kept as large as possible. As is well known, the minimum angle in the grid is inversely related to mesh-originated errors. To keep the grid regular, cubic building blocks are used. Each cube is divided into tetrahedral cells. The block of tetrahedral cells are then assembled together to produce the region to be meshed.

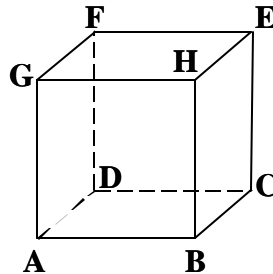
There exists a number of ways to divide a cube into tetrahedral cells. Each method produces its own specific number of tetrahedral cells inside the cube. This number can be 5, 6, 12, etc. An study on the resultant tetrahedral cells from each dividing method shows that small angles result from any division method that contains divisions requiring drawing of the cube's larger diagonals, i.e., diagonals FB, DH, AE, and GC in the following figure. If these diagonals are to be avoided, the cube can be divided into 5 tetrahedral cells. All triangular faces will have angles of at least 45 degrees. One specific

tetrahedron will consist of equilateral triangles for its faces. The overall mesh will have very good quality.

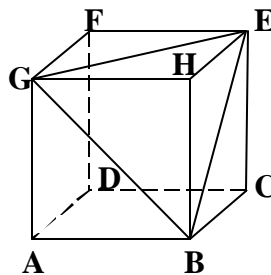
The drawback of this method is the fact that it can not be fitted easily to the curved boundaries. Therefore, this grid generator is used in this research, for geometries without curvature. Other grid generation methods, such as the advancing front method are used for curved geometries.

The following contains an illustrated explanation of the division method applied on a cube.

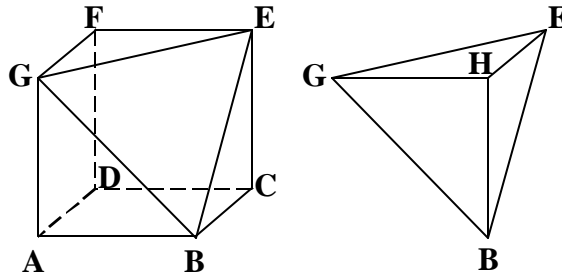
Consider the following cube (ABCDEFGH)



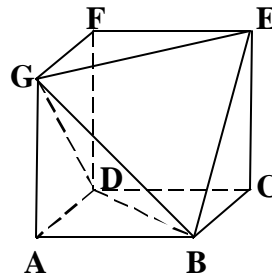
Draw diagonals GE, GB, and BE



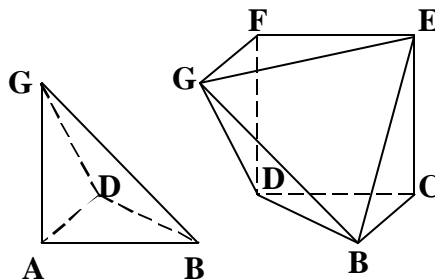
The first tetrahedron (GHEB) is then built. For demonstration purpose, this tetrahedron is cut from the original cube and shown separately below.



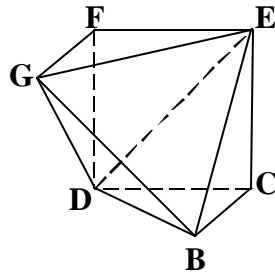
On the remaining polyhedron, draw diagonals DB and DG



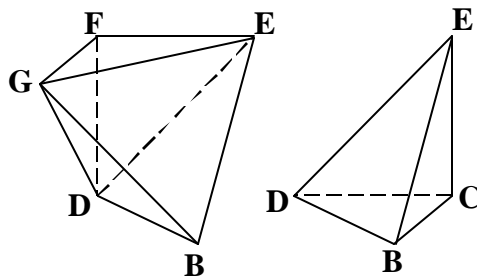
The second tetrahedron (GABD) is then built. For demonstration purpose, this tetrahedron is cut from the original cube and shown separately below.



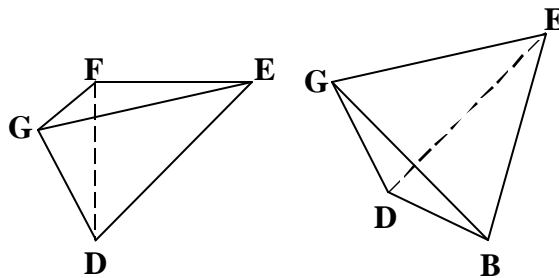
On the remaining polyhedron, draw diagonal DE



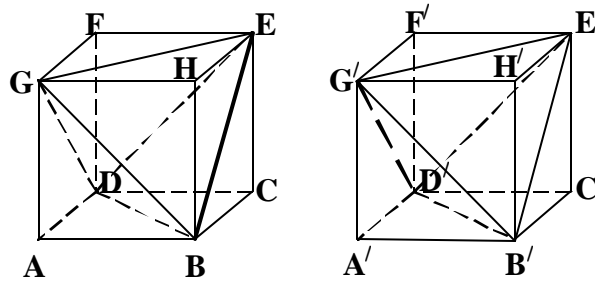
The third tetrahedron (EBCD) is then built. For demonstration purpose, this tetrahedron is cut from the original cube and shown separately below.



The remaining polyhedron is readily divided into the fourth and the fifth tetrahedral cells, i.e., FEGD and GDBE. For demonstration purpose, these cells are shown separately below



Examination of the sub-elements of the cubic block shows that the next block can not be generated only by translation of the first block. This difficulty originated from the fact that the larger diagonals needed to be avoided. The following figure demonstrates this problem.



As can be seen, if the second block ($A'B'C'D'E'F'G'H'$) is assembled on the first block, triangular faces will not match since edges EB and $G'D'$ cross each other. A rotation would be needed; repeated rotations would complicate the computer program. One way to overcome this difficulty can be explained as follows. Imagine that the mirror image of the block $ABCDEFGH$ (containing 5 cells) with respect to face $BCEH$ is attached to the first block at face $BCEH$. The new block containing 10 tetrahedral cells can then easily generate additional blocks only by translation in the horizontal direction. A similar technique can be used in the other two directions of the coordinate systems. Finally, the building blocks that can be easily assembled on each other, without any rotation, consist of 8 cubes attached together. The final building block contains 40 tetrahedral cells.

A computer program is then written to generate a prescribed domain, filled with the above 40-cell blocks.

APPENDIX C

In this appendix, the derivatives of the flux functions, related to the CE/SE Navier-Stokes formulation, are derived. The first step is to express the flux functions \vec{F} and \vec{G} in terms of the components of vector \vec{U} . For clarity, we repeat the definitions of vectors \vec{F} , \vec{G} , and \vec{U} from Chapter 8:

$$\vec{U} = \begin{bmatrix} \mathbf{r} \\ \mathbf{r}u \\ \mathbf{r}v \\ \mathbf{r}E \end{bmatrix} \quad (\text{C.1})$$

$$\vec{F} = \begin{bmatrix} \mathbf{r}u \\ \mathbf{r}u^2 + p - \mathbf{t}_{xx} \\ \mathbf{r}uv - \mathbf{t}_{xy} \\ (\mathbf{r}E + p)u - u\mathbf{t}_{xx} - v\mathbf{t}_{xy} - kT_x \end{bmatrix} \quad (\text{C.2})$$

$$\vec{G} = \begin{bmatrix} \mathbf{r}v \\ \mathbf{r}uv - \mathbf{t}_{xy} \\ \mathbf{r}v^2 + p - \mathbf{t}_{yy} \\ (\mathbf{r}E + p)v - u\mathbf{t}_{xy} - v\mathbf{t}_{yy} - kT_y \end{bmatrix} \quad (\text{C.3})$$

In the above definitions, the pressure is substituted for, using the stiffened gas equation of state, i.e. Eq. (8.5). Further, Eq. (8.3) is used for substituting the shear stresses. The flux functions can then be expressed in terms of the components of \vec{U} as follows

$$F_1 = U_2 \quad (\text{C.4})$$

$$F_2 = \frac{(U_2)^2}{U_1} + (\tilde{\mathbf{g}} - 1) \left\{ U_4 - \frac{1}{2} U_1 \left[\left(\frac{U_2}{U_1} \right)^2 + \left(\frac{U_3}{U_1} \right)^2 \right] \right\} \\ - \tilde{\mathbf{g}} B - \frac{2}{3} \mathbf{m} \left[2 \frac{(U_x)_2}{U_1} - 2 \frac{U_2 (U_x)_1}{(U_1)^2} - \frac{(U_y)_3}{U_1} + \frac{U_3 (U_y)_1}{(U_1)^2} \right] \quad (\text{C.5})$$

$$F_3 = \frac{U_2 U_3}{U_1} \\ - \mathbf{m} \left[\frac{(U_y)_2}{U_1} - \frac{U_2 (U_y)_1}{(U_1)^2} + \frac{(U_x)_3}{U_1} - \frac{U_3 (U_x)_1}{(U_1)^2} \right] \quad (\text{C.6})$$

$$F_4 = \frac{U_2}{U_1} \left\{ U_4 + (\tilde{\mathbf{g}} - 1) \left[U_4 - \frac{U_1}{2} \left(\left(\frac{U_2}{U_1} \right)^2 + \left(\frac{U_3}{U_1} \right)^2 \right) \right] - \tilde{\mathbf{g}} B \right\} \\ - \frac{2}{3} \mathbf{m} \frac{U_2}{U_1} \left[2 \frac{(U_x)_2}{U_1} - 2 \frac{U_2 (U_x)_1}{(U_1)^2} - \frac{(U_y)_3}{U_1} + \frac{U_3 (U_y)_1}{(U_1)^2} \right] \\ - \mathbf{m} \frac{U_3}{U_1} \left[\frac{(U_y)_2}{U_1} - \frac{U_2 (U_y)_1}{(U_1)^2} + \frac{(U_x)_3}{U_1} - \frac{U_3 (U_x)_1}{(U_1)^2} \right] - k T_x \quad (\text{C.7})$$

$$G_1 = U_3 \quad (\text{C.8})$$

$$G_2 = F_3 = \frac{U_2 U_3}{U_1} - \mathbf{m} \left[\frac{(U_y)_2}{U_1} - \frac{U_2 (U_y)_1}{(U_1)^2} + \frac{(U_x)_3}{U_1} - \frac{U_3 (U_x)_1}{(U_1)^2} \right] \quad (\text{C.9})$$

$$G_3 = \frac{(U_3)^2}{U_1} + (\tilde{\mathbf{g}} - 1) \left\{ U_4 - \frac{1}{2} U_1 \left[\left(\frac{U_2}{U_1} \right)^2 + \left(\frac{U_3}{U_1} \right)^2 \right] \right\} - \tilde{\mathbf{g}} B - \frac{2}{3} \mathbf{m} \left[2 \frac{(U_y)_3}{U_1} - 2 \frac{U_3 (U_y)_1}{(U_1)^2} - \frac{(U_x)_2}{U_1} + \frac{U_2 (U_x)_1}{(U_1)^2} \right] \quad (\text{C.10})$$

$$G_4 = \frac{U_3}{U_1} \left\{ U_4 + (\tilde{\mathbf{g}} - 1) \left[U_4 - \frac{U_1}{2} \left(\left(\frac{U_2}{U_1} \right)^2 + \left(\frac{U_3}{U_1} \right)^2 \right) \right] - \tilde{\mathbf{g}} B \right\} - \frac{2}{3} \mathbf{m} \frac{U_3}{U_1} \left[2 \frac{(U_y)_3}{U_1} - 2 \frac{U_3 (U_y)_1}{(U_1)^2} - \frac{(U_x)_2}{U_1} + \frac{U_2 (U_x)_1}{(U_1)^2} \right] - \mathbf{m} \frac{U_2}{U_1} \left[\frac{(U_y)_2}{U_1} - \frac{U_2 (U_y)_1}{(U_1)^2} + \frac{(U_x)_3}{U_1} - \frac{U_3 (U_x)_1}{(U_1)^2} \right] - k T_y \quad (\text{C.11})$$

Now that the flux functions are expressed in terms of the independent variables, the Jacobian components, needed in Eq. (8.10), can be derived by as follows. Differentiation of Eq. (C.4) leads to

$$\frac{\partial F_1}{\partial U_1} = \frac{\partial F_1}{\partial U_3} = \frac{\partial F_1}{\partial U_4} = 0 \quad (\text{C.12})$$

and

$$\frac{\partial F_1}{\partial U_2} = 1 \quad (\text{C.13})$$

Differentiation of Eq. (C.5) yields the following

$$\begin{aligned} \frac{\partial F_2}{\partial U_1} = & -\left(\frac{U_2}{U_1}\right)^2 + \frac{(\tilde{\mathbf{g}} - 1)}{2} \left[\left(\frac{U_2}{U_1}\right)^2 + \left(\frac{U_3}{U_1}\right)^2 \right] \\ & - \frac{2}{3} \mathbf{m} \left[-2 \frac{(U_x)_2}{(U_1)^2} + 4 \frac{U_2 (U_x)_1}{(U_1)^3} + \frac{(U_y)_3}{(U_1)^2} - 2 \frac{U_3 (U_y)_1}{(U_1)^3} \right] \end{aligned} \quad (\text{C.14})$$

$$\frac{\partial F_2}{\partial U_2} = (3 - \tilde{\mathbf{g}}) \frac{U_2}{U_1} + \frac{4}{3} \mathbf{m} \frac{(U_x)_1}{(U_1)^2} \quad (\text{C.15})$$

$$\frac{\partial F_2}{\partial U_3} = (1 - \tilde{\mathbf{g}}) \frac{U_3}{U_1} - \frac{2}{3} \mathbf{m} \frac{(U_y)_1}{(U_1)^2} \quad (\text{C.16})$$

$$\frac{\partial F_2}{\partial U_4} = \tilde{\mathbf{g}} - 1 \quad (\text{C.17})$$

Differentiation of Eq. (C.6) provides

$$\begin{aligned} \frac{\partial F_3}{\partial U_1} = & -\frac{U_2 U_3}{(U_1)^2} \\ & - \mathbf{m} \left[\frac{(U_y)_2}{(U_1)^2} + 2 \frac{U_2 (U_y)_1}{(U_1)^3} - \frac{(U_x)_3}{(U_1)^2} + 2 \frac{U_3 (U_x)_1}{(U_1)^3} \right] \end{aligned} \quad (\text{C.18})$$

$$\frac{\partial F_3}{\partial U_2} = \frac{U_3}{U_1} + \mathbf{m} \frac{(U_y)_1}{(U_1)^2} \quad (\text{C.19})$$

$$\frac{\partial F_3}{\partial U_3} = \frac{U_2}{U_1} + \mathbf{m} \frac{(U_x)_1}{(U_1)^2} \quad (\text{C.20})$$

and

$$\frac{\partial F_3}{\partial U_4} = 0 \quad (\text{C.21})$$

Differentiation of Eq. (C.7) results in the following

$$\begin{aligned} \frac{\partial F_4}{\partial U_1} = & \frac{\tilde{\mathbf{g}} - 1}{2} \frac{U_2}{U_1} \left[\left(\frac{U_2}{U_1} \right)^2 + \left(\frac{U_3}{U_1} \right)^2 \right] - \\ & \frac{U_2}{(U_1)^2} \left\{ U_4 + (\tilde{\mathbf{g}} - 1) \left[U_4 - \frac{U_1}{2} \left(\left(\frac{U_2}{U_1} \right)^2 + \left(\frac{U_3}{U_1} \right)^2 \right) \right] - \tilde{\mathbf{g}} B \right\} \\ & - \frac{2}{3} \mathbf{m} \frac{U_2}{U_1} \left[-2 \frac{(U_x)_2}{(U_1)^2} + 4 \frac{U_2 (U_x)_1}{(U_1)^3} + \frac{(U_y)_3}{(U_1)^2} - 2 \frac{U_3 (U_y)_1}{(U_1)^3} \right] \\ & + \frac{2}{3} \mathbf{m} \frac{U_2}{(U_1)^2} \left[2 \frac{(U_x)_2}{U_1} - 2 \frac{U_2 (U_x)_1}{(U_1)^2} + \frac{(U_y)_3}{U_1} + 2 \frac{U_3 (U_y)_1}{(U_1)^2} \right] \\ & - \mathbf{m} \frac{U_3}{U_1} \left[-\frac{(U_y)_2}{(U_1)^2} + 2 \frac{U_2 (U_y)_1}{(U_1)^3} - \frac{(U_x)_3}{(U_1)^2} + 2 \frac{U_3 (U_x)_1}{(U_1)^3} \right] \\ & + \mathbf{m} \frac{U_3}{(U_1)^2} \left[\frac{(U_y)_2}{U_1} - \frac{U_2 (U_y)_1}{(U_1)^2} + \frac{(U_x)_3}{U_1} - \frac{U_3 (U_x)_1}{(U_1)^2} \right] \end{aligned} \quad (\text{C.22})$$

$$\begin{aligned}
\frac{\partial F_4}{\partial U_2} = & (1 - \tilde{\mathbf{g}}) \left(\frac{U_2}{U_1} \right)^2 + \\
& \frac{1}{U_1} \left\{ U_4 + (\tilde{\mathbf{g}} - 1) \left[U_4 - \frac{U_1}{2} \left(\left(\frac{U_2}{U_1} \right)^2 + \left(\frac{U_3}{U_1} \right)^2 \right) \right] - \tilde{\mathbf{g}} B \right\} \\
& - \frac{2}{3} \frac{\mathbf{m}}{U_1} \left[2 \frac{(U_x)_2}{U_1} - 2 \frac{U_2 (U_x)_1}{(U_1)^2} - \frac{(U_y)_3}{U_1} + \frac{U_3 (U_y)_1}{(U_1)^2} \right] \\
& + \frac{4}{3} \mathbf{m} \frac{U_2 (U_x)_1}{(U_1)^3} + \mathbf{m} \frac{U_3 (U_y)_1}{(U_1)^3}
\end{aligned} \tag{C.23}$$

$$\begin{aligned}
\frac{\partial F_4}{\partial U_3} = & (1 - \tilde{\mathbf{g}}) \frac{U_2 U_3}{(U_1)^2} - \frac{2}{3} \mathbf{m} \frac{U_2 (U_y)_1}{(U_1)^3} \\
& - \frac{\mathbf{m}}{U_1} \left[\frac{(U_y)_2}{U_1} - \frac{U_2 (U_y)_1}{(U_1)^2} + \frac{(U_x)_3}{U_1} - \frac{U_3 (U_x)_1}{(U_1)^2} \right] \\
& + \mathbf{m} \frac{U_3 (U_x)_1}{(U_1)^3}
\end{aligned} \tag{C.24}$$

$$\frac{\partial F_4}{\partial U_4} = \tilde{\mathbf{g}} \frac{U_2}{U_1} \tag{C.25}$$

Similarly, differentiation of Eq. (C.8) leads to

$$\frac{\partial G_1}{\partial U_1} = \frac{\partial G_1}{\partial U_2} = \frac{\partial G_1}{\partial U_4} = 0 \tag{C.26}$$

and

$$\frac{\partial G_1}{\partial U_3} = 1 \tag{C.27}$$

Since $G_2 = F_3$, derivatives of G_2 with respect to components of \vec{U} , can be readily computed from Eqs. (C.18)-(C.21). Further proceeding, Eq. (C.10) can be differentiated to provide

$$\begin{aligned} \frac{\partial G_3}{\partial U_1} = & -\left(\frac{U_3}{U_1}\right)^2 + \frac{(\tilde{\mathbf{g}} - 1)}{2} \left[\left(\frac{U_2}{U_1}\right)^2 + \left(\frac{U_3}{U_1}\right)^2 \right] \\ & - \frac{2}{3} \mathbf{m} \left[-2 \frac{(U_y)_3}{(U_1)^2} + 4 \frac{U_3 (U_y)_1}{(U_1)^3} + \frac{(U_x)_2}{(U_1)^2} - 2 \frac{U_2 (U_x)_1}{(U_1)^3} \right] \end{aligned} \quad (\text{C.28})$$

$$\frac{\partial G_3}{\partial U_2} = (1 - \tilde{\mathbf{g}}) \frac{U_2}{U_1} - \frac{2}{3} \mathbf{m} \frac{(U_x)_1}{(U_1)^2} \quad (\text{C.29})$$

$$\frac{\partial G_3}{\partial U_3} = (3 - \tilde{\mathbf{g}}) \frac{U_3}{U_1} + \frac{4}{3} \mathbf{m} \frac{(U_y)_1}{(U_1)^2} \quad (\text{C.30})$$

$$\frac{\partial G_3}{\partial U_4} = \tilde{\mathbf{g}} - 1 \quad (\text{C.31})$$

Finally, differentiation of Eq. (C.11) results in

$$\begin{aligned}
\frac{\partial G_4}{\partial U_1} = & \frac{\tilde{\mathbf{g}}-1}{2} \frac{U_3}{U_1} \left(\left(\frac{U_2}{U_1} \right)^2 + \left(\frac{U_3}{U_1} \right)^2 \right) - \\
& \frac{U_3}{(U_1)^2} \left\{ U_4 + (\tilde{\mathbf{g}}-1) \left[U_4 - \frac{U_1}{2} \left(\left(\frac{U_2}{U_1} \right)^2 + \left(\frac{U_3}{U_1} \right)^2 \right) \right] - \tilde{\mathbf{g}} B \right\} \\
& - \frac{2}{3} \mathbf{m} \frac{U_3}{U_1} \left[-2 \frac{(U_y)_3}{(U_1)^2} + 4 \frac{U_3 (U_y)_1}{(U_1)^3} + \frac{(U_x)_2}{(U_1)^2} - 2 \frac{U_2 (U_x)_1}{(U_1)^3} \right] \\
& + \frac{2}{3} \mathbf{m} \frac{U_3}{(U_1)^2} \left[2 \frac{(U_y)_3}{U_1} - 2 \frac{U_3 (U_y)_1}{(U_1)^2} - \frac{(U_x)_2}{U_1} + \frac{U_2 (U_x)_1}{(U_1)^2} \right] \\
& - \mathbf{m} \frac{U_2}{U_1} \left[-\frac{(U_y)_2}{(U_1)^2} + 2 \frac{U_2 (U_y)_1}{(U_1)^3} - \frac{(U_x)_3}{(U_1)^2} + 2 \frac{U_3 (U_x)_1}{(U_1)^3} \right] \\
& + \mathbf{m} \frac{U_2}{(U_1)^2} \left[\frac{(U_y)_2}{U_1} - \frac{U_2 (U_y)_1}{(U_1)^2} + \frac{(U_x)_3}{U_1} - \frac{U_3 (U_x)_1}{(U_1)^2} \right]
\end{aligned} \tag{C.32}$$

$$\begin{aligned}
\frac{\partial G_4}{\partial U_2} = & (1-\tilde{\mathbf{g}}) \frac{U_2 U_3}{(U_1)^2} - \frac{2}{3} \mathbf{m} \frac{U_3 (U_x)_1}{(U_1)^3} \\
& - \frac{\mathbf{m}}{U_1} \left[\frac{(U_y)_2}{U_1} - \frac{U_2 (U_y)_1}{(U_1)^2} + \frac{(U_x)_3}{U_1} - \frac{U_3 (U_x)_1}{(U_1)^2} \right] \\
& + \mathbf{m} \frac{U_2 (U_y)_1}{(U_1)^3}
\end{aligned} \tag{C.33}$$

$$\begin{aligned}
\frac{\partial G_4}{\partial U_3} = & (1-\tilde{\mathbf{g}}) \left(\frac{U_3}{U_1} \right)^2 + \\
& \frac{1}{U_1} \left\{ U_4 + (\tilde{\mathbf{g}}-1) \left[U_4 - \frac{U_1}{2} \left(\left(\frac{U_2}{U_1} \right)^2 + \left(\frac{U_3}{U_1} \right)^2 \right) \right] - \tilde{\mathbf{g}} B \right\} \\
& - \frac{2}{3} \mathbf{m} \frac{U_3}{U_1} \left[2 \frac{(U_y)_3}{U_1} - 2 \frac{U_3 (U_y)_1}{(U_1)^2} - \frac{(U_x)_2}{U_1} + \frac{U_2 (U_x)_1}{(U_1)^2} \right] \\
& + \frac{4}{3} \mathbf{m} \frac{U_3 (U_y)_1}{(U_1)^3} + \mathbf{m} \frac{U_2 (U_x)_1}{(U_1)^3}
\end{aligned} \tag{C.34}$$

$$\frac{\partial G_4}{\partial U_4} = \tilde{\mathbf{g}} \frac{U_3}{U_1} \quad (\text{C.35})$$

The above Jacobian components can then be used in Eqs. (8.9) and (8.10) in order to compute the derivatives of the flux functions.